# Acoustic Characteristics of Northern and Southern Resident Killer Whale Echolocation Clicks

by

Jack Lawson
B.Eng., Royal Military College of Canada, 2011

A Thesis Submitted in Partial Fulfillment of the
Requirements for the Degree of

MASTER OF SCIENCE

in the School of Earth and Ocean Sciences

University of Victoria

# Acoustic Characteristics of Northern and Southern Resident Killer Whale Echolocation Clicks

by

Jack Lawson
B.Eng., Royal Military College of Canada, 2011

Supervisory Committee

---

Dr. S.E. Dosso, Supervisor
(School of Earth and Ocean Sciences)

---

Dr. A. Monahan, Departmental Member
(School of Earth and Ocean Sciences)

---

Dr. S. Vagle, Departmental Member
(School of Earth and Ocean Sciences )
(Fisheries and Oceans Canada)

# ABSTRACT

Resident killer whales (*Orcinus orca*) in the Salish Sea use echolocation clicks to hunt for Chinook salmon, their preferred prey. An increase in underwater anthropogenic noise in recent decades has been identified as a threat to their survival due to auditory masking effects on these signals. Studies quantifying the effects of anthropogenic noise on echolocation signals have yet to be carried out due to a data gap for echolocation acoustic characteristics. In particular, to date, only one study has reported click characteristics for northern resident killer whales, and no results have been reported for southern residents. This thesis reports on acoustic recordings of resident killer whale echolocation clicks gathered over two summers in several locations around Vancouver Island, and spectral and temporal characteristics extracted from them. Acoustic characteristics are reported separately for southern and northern resident killer whales based on 708 clicks from 19 click trains and 1277 clicks from 16 click trains, respectively. Results are further categorized into click type (slow, fast, and buzz clicks) based on inter-click interval, an indicator of foraging phase. Results show no differences in acoustic characteristics between the northern and southern killer whales, suggesting echolocation clicks do not vary between these subspecies. No significant differences are noted between slow- and fast-click characteristics, while buzz clicks appear to have some significant differences in characteristics from the others. Apparent source level values for northern and southern killer whales vary between 179-221 dB re 1 $\mu$Pa at 1 m and 192-220 dB re 1 $\mu$Pa at 1 m, respectively, based on the largest amplitude click from each click train (assumed to be directed towards the recording array). The values reported in this thesis will be used in subsequent noise modelling studies to quantify the effects of anthropogenic noise on resident killer whale ability to hunt for prey via echolocation signals.

# Contents

# List of Tables

# List of Figures

# ACKNOWLEDGEMENTS

I would like to thank:

**Stan Dosso,** for his time, effort, and encouragement, which was, perhaps, not always earned.

**the Ocean and Freshwater Science Contribution Program,** for funding this research.

**Jen Wladichuk, Svein Vagle, Caitlin O'Neill, and Peter Van Buren** for their determination and enthusiasm in overcoming every difficulty encountered along the way.

**the Department of Fisheries and Oceans,** for contracting the northern resident killer whale research.

**Lord Fitzgerald Cornwallis Alder McLawson III,** for allowing me to accompany him on daily walks.

**Dugald Thomson,** for haphazardly suggesting I call UVic, while staring glazy eyed into his boxed-lunch sandwich.

*In the beginning, the Universe was created. This had made a lot of people very angry and been widely regarded as a bad move.*

Douglas Adams

# DEDICATION

To Jenna, your ability to look beyond the unfairness surrounding our two employments is rivaled only by your inability to rise to the land of the waking. I love you so very much.

# Chapter 1

# Introduction

The Salish Sea composes one of the richest and most ecologically diverse habitats in North America. Spanning from the Pacific Ocean's entrance to the Juan de Fuca strait in the west, to the complex estuarine basins of Puget Sound in the south, and beyond the fast-flowing Strait of Georgia in the north, the once quiet aquatic home to many animal species is experiencing significant change due to anthropogenic activity. Encompassed within the region are the coastal cities of Seattle, Vancouver, and Victoria, among others. As the sole waterway connecting this megalopolis to the Pacific Ocean, the Salish Sea experiences denser shipping traffic than any other coastal area in Canada. While chemical pollutants and threats of oil spills tend to be at the forefront of public concern, a less recognized but more insidious threat to parts of the Salish Sea's environment exists: anthropogenic noise. Among species affected by anthropogenic noise are *Orcinus orca*, also known as killer whales, with resident killer whales (RKWs) the ecotype most affected.

Southern and northern resident killer whale (SRKW and NRKW, respectively) populations are thought to have significantly fewer individuals than they did a hundred years ago (U.S.A. Official Marine Mammal Commission). The government of Canada recognizes its role in ensuring the survival of its RKW populations, and has published an ever-evolving recovery strategy meant to encourage their growth [1]. A threat has been identified concerning RKW ability to forage for preferred prey (Chinook salmon) in the presence of an increasing level of anthropogenic noise, produced mainly by small boats and large shipping vessels [2]. Studies throughout the past decades have quantified and characterized anthropogenic noise in the Salish Sea, while others have looked closely at acoustic characteristics of RKW communications (whistles and calls), and the interaction between the two [3] [4]. Few studies, however, have quantified the potential interference of anthropogenic noise on the acoustic signals used by RKWs to navigate and forage: echolocation clicks. This thesis seeks to rectify an existing data gap by reporting on acoustic characteristics of RKW echolocation clicks. Future work will use these results to quantify the effects of anthropogenic noise on RKW foraging and navigational abilities.

## 1.1 RKW Populations and the Critical Habitat

In 1964, a male SRKW, *Moby Doll*, was captured off the coast of Saturna Island for public display at the Vancouver Aquarium — the first of many to follow. The next decade saw approximately 47 adult RKW captures for display while another dozen or so are believed to have died during the capture process [5]. In 1976, public concern over dwindling RKW populations pressured the Canadian and American governments into halting all live captures until a population assessment could be carried out. This began the annual census of RKW populations which has been carried out every year since, and reported by the Center for Whale Research (CWR). The discovery that RKW populations were much lower than previously thought led to the indefinite ban of their live capture. Unfortunately, the damage that had already been inflicted proved vast, particularly for the SRKW population whose growth has remained more or less stagnant for the last five decades.

The first SRKW census took place in 1974, following the cessation of live captures, and placed the population at 71 individuals within 3 pods (referred to as J, K, and L pods). Since then, the population has fluctuated, peaking in the mid-1990s at an estimated 97 individuals, but falling to 76 in 2020. The last decade has seen only 17 new births, of which six have disappeared, assumed dead [6]. Additionally, that same period has witnessed the disappearance and assumed death of an estimated 26 adults [6]. The NRKW population has experienced more encouraging growth rates in the past decades, and sits at approximately 309 individuals as of 2017 [1]. Figures 1.1 and 1.2 present SRKW and NRKW population estimates from 1976-2017 and 1974-2016, respectively. While the NRKW population is trending up, the SRKW population has, at best, appeared to stagnate.

In 2001, under the Species at Risk Act (SARA), the government of Canada designated SRKWs as endangered, and NRKWs as threatened [1]. Similarly, in 2005, the government of the United States listed SRKWs as endangered under its own act, the Endangered Species Act [6]. In 2008, the government of Canada published a docu-

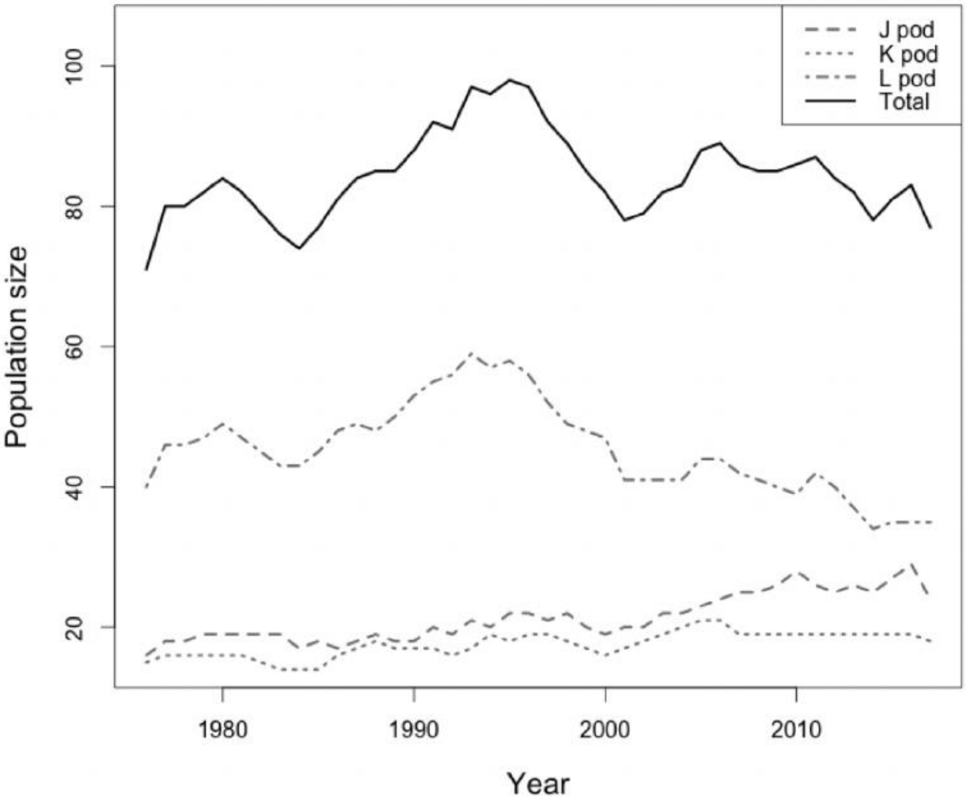

Figure 1.1: SRKW population estimates from 1976-2017 (J, K, L pods and total). Despite increases in the 1990s, the population has since decreased and appears to have stagnated. Figure reproduced from: Recovery Strategy for the Northern and Southern Resident Killer Whales (*Orcinus orca*) in Canada. [1].

ment titled *Recovery Strategy for the Northern and Southern Resident Killer Whales (Orcinus orca) in Canada*, which has since been updated twice: once in 2011, and again in 2018 [1]. The overarching goal of the strategy is "to ensure the long-term viability of Resident Killer Whale populations by achieving and maintaining demographic conditions that preserve their reproductive potential, genetic variation, and cultural continuity" [1]. In order to achieve this goal, the strategy has been further divided into four principal objectives:

1. to ensure that RKWs have an adequate and accessible food supply to allow recovery;
2. to ensure that chemical and biological pollutants do not prevent the recovery of RKW populations;

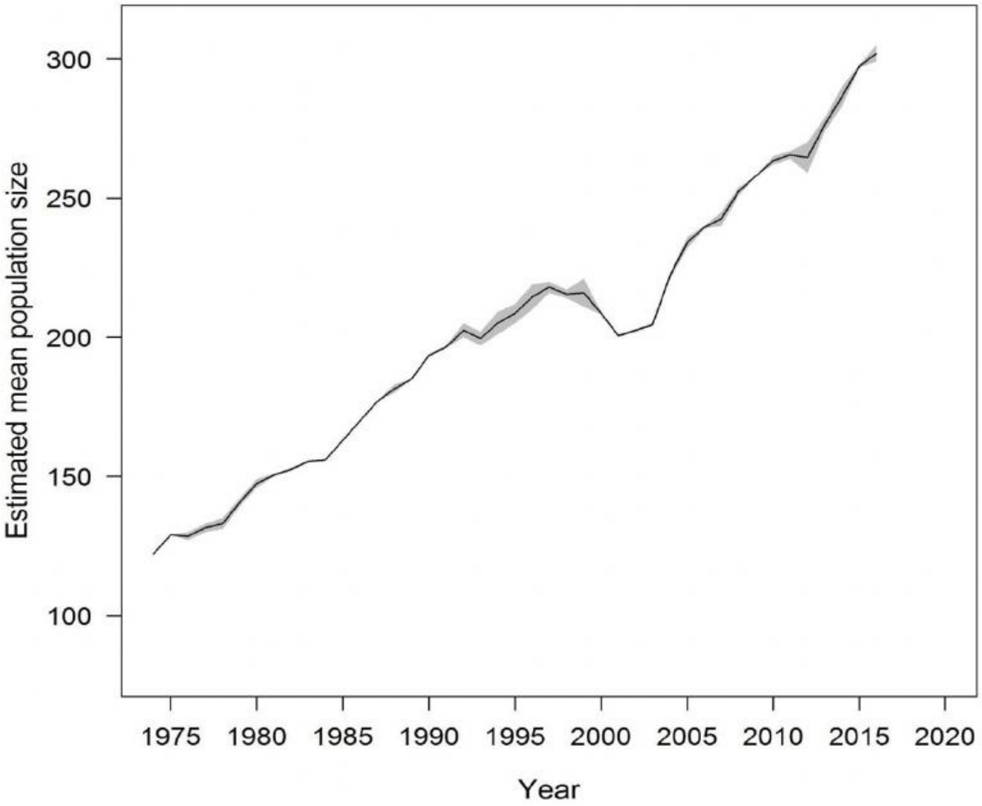

Figure 1.2: NRKW population estimates from 1974-2016. Shaded portions represent uncertainty due to difficulties identifying all individuals. Figure reproduced from: Recovery Strategy for the Northern and Southern Resident Killer Whales (*Orcinus orca*) in Canada [1].

3. to ensure that disturbance from human activities does not prevent the recovery of RKWs;
4. to protect critical habitat for RKWs and identify additional areas for critical habitat designation and protection.

A critical habitat is defined as “an area necessary for the survival or recovery of a listed wildlife species” [1]. The strategy has decreed, supported by SARA, that certain areas be designated critical habitats for RKWs, and be afforded particular attention in respect to the potential for its destruction or degradation due to anthropogenic activity. The NRKW critical habitat ranges from Northern Vancouver Island to Alaska, including Queen Charlotte Sound, and the waters surrounding Haida

Gwaii. The SRKW critical habitat overlaps the NRKW habitat on the south side of Vancouver Island, and continues southeast to Puget Sound and northeast to the Strait of Georgia between mainland BC and the north side of Vancouver Island. Figure 1.3 shows RKW critical habitats recognized by the Government of Canada.

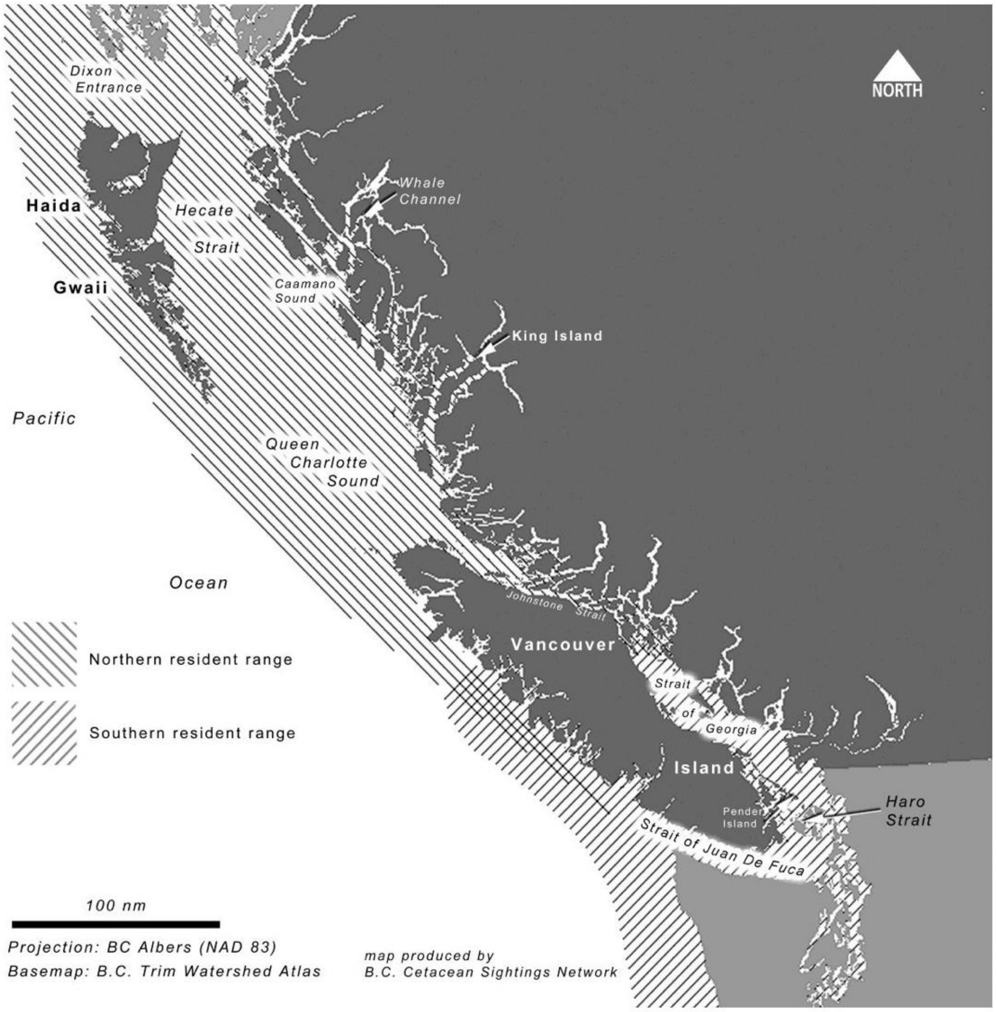

Figure 1.3: RKW critical habitats surrounding Vancouver Island and coastal mainland BC. Figure reproduced from: Recovery Strategy for the Northern and Southern Resident Killer Whales (*Orcinus orca*) in Canada [1].

It is within these areas that scientific efforts are being focused. From prey availability studies to potential contaminant measurements to continuous sound monitoring, studying and protecting RKW critical habitats is paramount in ensuring population survivability. This study seeks to contribute to the RKW recovery strategy by focusing on principal objective number three; that is, preventing human activity from disturbing RKW recovery, in particular, RKW foraging ability in the presence of underwater anthropogenic noise. The contribution is manifested through the quantification of RKW echolocation acoustic characteristics, which future work in this project will make use of in combination with noise modelling to consider affects on echolocation in various noise scenarios.

## 1.2 RKW Echolocation Clicks and the Data Gap

RKWs use sound as their primary tool for a number of functions, including communication, navigation, and foraging. While communicative signals take the form of “calls” and “whistles”, and function as a method of relaying information to others, foraging and navigation are carried out through a process known as echolocation. Echolocation refers to an animal’s ability to transmit an acoustic signal and receive an echo of the signal following its reflection off of an object. The return echo provides information to the echolocating animal about the reflecting object, such as bearing, range, size, and velocity. It is particularly important to RKWs as it is the primary method by which they hunt for prey, as opposed to mammal-eating whales, such as transient (Bigg’s) killer whales, who hunt visually. RKW echolocation is achieved through the use of phonic lips — a mechanism similar in structure to the human nasal cavity, but in operation to the human vocal chord. First, modulated by a fatty sac, compressed air is forced through lips located near the RKW’s cranium, resulting in a highly directional and impulsive “click”. Returning clicks, after reflecting off an object, are filtered through an oil filled channel in the RKW’s lower jaw, and conducted to the middle ear [7]. The whale can discern distance and bearing information of objects based on the time delay and direction of returning acoustic energy. Due to the impulsiveness of the signal, and its very short duration, RKWs tend to produce many clicks every second, the collection of which is known as a click train.

Echolocation clicks have a shorter effective range than calls or whistles. Unlike communicative signals, clicks suffer from two-way propagation loss as opposed to only one-way loss. Furthermore, only a relatively small fraction of the original signal’s energy is reflected and returned to the signal’s originator. In order to effectively echolocate, a RKW must be able to distinguish a returning signal from the noise in its immediate environment. One study has shown that RKWs increase their call amplitude proportionately to increasing ambient noise in the surrounding environment [4]. It follows then, that the more noise in the environment, the greater the reduction in effective echolocation range, in respect to both navigation and foraging. RKWs are accustomed to filtering out biotic and abiotic noise from their signals, a characteristic developed over millennia of evolution. Anthropogenic noise, however, is a relatively new phenomena (approximately a century old), the sudden onset of which marine mammals have been unable to quickly adapt to [8]. The combination of already prevalent small boat traffic and an increase in large boat traffic (shipping vessels) is leading to noise levels never before experienced by RKWs in their critical habitat.

While echolocation is of fundamental importance to RKWs, there is a dearth of information (data gap) on echolocation click characteristics, including source level, temporal and spectral characteristics, and directionality (beam pattern), all of which are instrumental in understanding how echolocation abilities are influenced by anthropogenic noise. To date, only one study [9], carried out in 2004, has presented results on some of the characteristics listed for NRKWs, and no such results have been reported for SRKWs. It is common for toothed whales to alter click type; that is, the characteristics of clicks, including frequency and source level, to provide more information on objects, such as size, shape, and velocity [10]. However, no study so far has yet attempted to quantify the differences in characteristics between click types for RKWs. Echolocating marine mammals use different types of click trains depending on the function they are carrying out. For example, while searching for prey, RKWs produce less frequent but more powerful clicks, and upon discovery of prey actively change click characteristics during pursuit [11]. The characteristic used to classify click type is the inter-click interval (ICI), which is a measurement of the time between the maximum amplitude of each click within a click train. Generally, echolocation clicks can be separated into three categories: slow-click trains (ICI $>$ 100 ms), fast-click trains (10 ms $<$ ICI $\leq$ 100 ms), and buzz-click trains (ICI $\leq$ 10 ms) [11]. Studies have hypothesized the different marine mammal behaviour that correspond with each click train type, and most are in agreement of their specific functions. RKWs utilize slow-click trains to search wide areas, over long distances allowing extra time for echoes to return. Fast-click trains are used to further refine the location of potential prey that have been located with slow-click trains. Finally, buzz-click trains tend to be used in the final phase of pursuit, most likely to provide immediate information on prey velocity, prior to capture attempts [11].

A research team from the University of Victoria, in collaboration with Fisheries and Oceans Canada, and funded through the Ocean and Freshwater Science Contribution Program, developed a plan to record echolocation clicks in RKW critical habitats, from which acoustic characteristics could be extracted to help rectify the existing data gap. This thesis reports on my contribution to these efforts.

## 1.3 Overview of Work in This Thesis

This thesis has been written as part of a four-year research project investigating anthropogenic impacts on RKWs and their prey. I had the opportunity to join a research team from the School of Earth and Ocean Sciences at year three of the project (2020), focusing on quantifying the abilities of RKW echolocation for prey in the presence of anthropogenic noise. In 2019, the research team designed and built a rectangular (2 m × 2 m) array of 20 hydrophones and deployed it from a small boat in SRKW and NRKW critical habitats around Vancouver Island. On several occasions, RKWs were encountered and echolocation click data were recorded. I joined the team shortly after this first field season and was employed to prepare for the second field season in summer 2020. I took part in preparing for and carrying out the second field season in the summer of 2020. This involved redesigning and rebuilding the array, and carrying out field recordings of SRKWs around southern Vancouver Island. Subsequently, I carried out the analysis of both the 2019 and 2020 data sets to derive echolocation click characteristics of interest to address the data gap mentioned above.

The work presented in this thesis has been organized into the following chapters. Chapter 2 outlines the theory used to determine RKW click source levels from the data; two approaches to source localization are discussed and compared, along with a description of propagation loss theory. Chapter 3 describes the hydrophone array configuration used in field seasons one and two, and presents a modelling comparison between configurations. This chapter also discusses fieldwork procedures and data acquisition, and calibration of the hydrophones. Chapter 4 presents the acoustic characteristics of RKW echolocation clicks extracted from the recorded data, which represent the main results of this work. Finally, Chapter 5 summarizes the thesis.

It is worth noting that an initial goal of the project was to estimate echolocation click directionality via beam pattern measurements. However, discerning beamwidth requires the whales to closely approach and click directly at the array. Unfortunately, such data were not collected, and hence beam characteristics could not be calculated.

At the time of this study, beam pattern estimates have yet to be quantified for RKWs.

# Chapter 2

# Theory

One goal of this study seeks to report an acoustic characteristic of RKW echolocation clicks that some other marine mammal acoustic studies omit: apparent source level (ASL). Generally, sound levels can be categorized into three types: received level (RL) — the acoustic intensity at the recording instrument's location; source level (SL) — the acoustic intensity back-calculated to 1 m from the source along the acoustic signal's direction of maximum source intensity; and ASL, defined by [12] as "the acoustic intensity back-calculated to 1 m in any direction from the sound source". While RL is unambiguous, there is an important distinction between SL and ASL. SL refers to the acoustic intensity along the acoustic axis (on-axis), while ASL is irrespective of directionality of the sound source. This is important because for the majority of publications on odontocetes, signal directionality can not be confirmed as on-axis. While data selection criteria can be established to increase the probability that a recording is made approximately on-axis (more detail given in Section 4.1), ASL is a more appropriate term to use when the on-axis directionality of a signal is questionable. The two sound level characteristics reported in this study are RL and ASL. The difference between these sound levels is encompassed in propagation loss (PL) which accounts for energy spreading and absorption as a signal propagates. PL is defined as the ratio of the acoustic intensity at 1 m from a source to the acoustic intensity at a distance $R$ (referred to as slant range or simply range here) from the source [12]. Since PL is a function of $R$, its determination requires the distance from the source to the receiver to be known. Determining the range between source (whale) and receiver requires acoustic localization of the source, as described in this chapter.

This chapter describes the theory used in this study to determine the effect of PL on RKW echolocation clicks, which is subsequently used to derive ASLs from RLs.

The first section considers PL, while the following sections describe two independent source localization methods used in this study to allow for the calculation of PL.

## 2.1 Transmission Loss

As an acoustic wave propagates from a source to a receiver, it experiences energy loss due to two effects: geometric spreading and absorption [13]. Geometric spreading occurs as the energy of a signal distributes over a greater surface area as it propagates. The type of modelling used to account for geometric spreading losses in water depends on the depth of the water column in relation to a signal's propagation distance; for water columns with a much greater depth than the distance over which the signal propagates (e.g., RKWs in this study), spherical spreading is an appropriate approximation. PL due to spherical spreading is calculated by determining the ratio of the surface area of a sphere with radius equal to the source-to-receiver distance (in metres), to the surface area of a sphere with radius 1 m (1 m from the source). Expressing this relationship in decibels, leads to the following equation for PL due to spherical spreading

$$\mathrm{PL}_{spherical} = 20\log R. \tag{2.1}$$

The other form of PL that must be considered is the energy loss due to absorption. While many different models exist to account for absorption in sea water, it is widely accepted that the frequency-dependent model proposed by Francois and Garrison based on empirical results is most accurate [13]. The model accounts for chemical losses due to the presence of boric acid and magnesium sulfate, and viscous losses in water (all have varying loss contributions based on temperature, salinity, pH, and frequency). The chemical losses are due to molecular relaxation; that is, the dissociation of ionic compounds (salts) in seawater due to the local pressure variations [13]. Absorption is dominated by chemical losses at frequencies up to about 100 kHz, and by viscous losses above 100 kHz. For this study, which assumes seawater characteristics and a representative echolocation signal frequency of 30 kHz, the average loss due to absorption is 0.01 dB/m, and can be expressed as

$$\mathrm{PL}_{absorption} = 0.01R. \tag{2.2}$$

Combining the equations for energy losses due to spherical spreading and absorption leads to an equation for total PL:

$$\mathrm{PL} = 20\log R + 0.01R. \tag{2.3}$$

## 2.2 Source Localization

Several different methods exist to localize the source of a recorded signal using what are called time of arrival differences (TOADs) — the lag-time between between signal arrivals at various sensors of an array. Localization consists of seeking the source position in three dimensions (3D) for which predicted TOAD data best match the measured data. This study uses 20 receivers (2019) and 23 receivers (2020) to conduct source localization.

The determination of TOADs across a series of receivers can be carried out via signal cross correlation, assuming the receivers are synchronized. Cross correlation is a measure of the similarity of two signals as a function of the delay or lag-time between the signals. Setting one receiver as a reference, and cross correlating its recorded signal with the signal recorded on each of the other receivers leads to a series of TOADs each referenced to the same receiver. Knowledge of each receiver's position relative to the reference receiver, and the sound speed of the medium, allows the location of the source to be estimated by minimizing the difference between the measured TOADs and those predicted for possible source locations. This study assumed a constant sound speed of 1485 m/s, a representative value for near-surface waters at time and location of the study. The localization results are relatively insensitive to this value, since for receivers separated by small distances compared to the propagation path length (as in our study), it only applies over the distance between receivers, not over the distance from source to receivers, minimizing the impact of varying sound speeds in the water on the localization calculations. Two approaches to source localization and uncertainty estimation are considered in this thesis including iterated linearized inversion and a 3D grid search. The following sections detail the mathematical procedures of these two approaches.

### 2.2.1 Linearized Inversion

Inversion is a mathematical method of estimating the parameters of a model of a physical system, given a set of observations of some process that interacts with the system. It is the determination of a model that fits a given set of data. Solving an inversion problem requires that a solution to the forward problem (predicting data for a given model) is known.

Localization is initially formulated here in a Bayesian sense to allow the computation of probability distributions to define uncertainties. For vectors $\mathbf{m}$ and $\mathbf{d}$ representing model parameters and observed data, respectively, with each assumed to be random variables, Bayes theorem can be expressed

$$P(\mathbf{m}|\mathbf{d}) = \frac{P(\mathbf{m})P(\mathbf{d}|\mathbf{m})}{P(\mathbf{d})}. \tag{2.4}$$

In this equation, $P(\mathbf{m})$ is the prior distribution, representing what is known about the model independent of the data. $P(\mathbf{d}|\mathbf{m})$ represents the conditional probability of the data given the model; however, for (fixed) observed data, this term is considered as a function of the model, defining the likelihood function $L(\mathbf{m})$. $P(\mathbf{m}|\mathbf{d})$ is the posterior probability distribution (PPD), the goal of the inversion, representing the state of information about the model including both data and prior information. $P(\mathbf{d})$ can be considered a normalization factor in the present formulation. In this thesis, only uniform priors are considered representing a constant value which may also be considered part of the normalization. Hence, Eq. (2.4) can be written

$$P(\mathbf{m}|\mathbf{d}) \propto L(\mathbf{m}), \tag{2.5}$$

indicating the PPD can be computed in terms of an appropriately-normalized likelihood function. Hence, in the remainder of this chapter, theory is presented in terms of likelihoods, with the understanding that normalization provides the PPD.

Analytic solutions for the optimal set of model parameters and their uncertainties are available for linear inverse problems. While localization is a non-linear problem, it is often solved via iterated linearized inversion; however, the solution, particularly uncertainty estimates, may suffer from linearization errors [14]. The general form of a linear inverse problem can be written as

$$\mathbf{d} = \mathbf{A}\mathbf{m}, \tag{2.6}$$

where $\mathbf{A}$ represents the Jacobian matrix which encompasses the physics of the forward problem. The equation can be solved by seeking the model corresponding to the maximum-likelihood (ML) estimate. Assuming identical, independently-distributed

Gaussian-distributed errors of unknown standard deviation $\sigma$, the likelihood function can be written

$$L(\mathbf{m}, \sigma) = \frac{1}{(2\pi)^{N/2}\sigma^N} \exp\left[-\frac{1}{2\sigma^2}|\mathbf{d} - \mathbf{d}(\mathbf{m})|^2\right], \tag{2.7}$$

where $\mathbf{d}(\mathbf{m})$ represents data predicted for model parameters $\mathbf{m}$. The ML estimate can be determined by maximizing the likelihood by setting

$$\frac{\partial L(\mathbf{m})}{\partial \mathbf{m}} = 0. \tag{2.8}$$

For an over-determined problem, the ML solution can solution can be written

$$\hat{\mathbf{m}} = \left[\mathbf{A}^T\mathbf{A}\right]^{-1}\mathbf{A}^T\mathbf{d}. \tag{2.9}$$

The associated uncertainty distribution for this solution represents a multi-variate Gaussian distribution about $\hat{\mathbf{m}}$ with a covariance matrix

$$\mathbf{C} = \sigma^2\left[\mathbf{A}^T\mathbf{A}\right]^{-1}. \tag{2.10}$$

The standard deviations for model parameters are square roots of the diagonal elements of $\mathbf{C}$. In problems with unknown data standard deviations, a ML estimate of $\sigma$ can be made by setting $\partial L/\partial\sigma = 0$ leading to

$$\hat{\sigma} = \left[\frac{1}{N}|\mathbf{d} - \mathbf{d}(\hat{\mathbf{m}})|^2\right]^{1/2}, \tag{2.11}$$

where $\mathbf{d} - \mathbf{d}(\hat{\mathbf{m}})$ are residuals — the difference between measured data and data predicted for the ML estimate.

To apply linear inverse theory (approximately) to a nonlinear problem like localization requires linearization. This is achieved by expanding a generalized Taylor series about a starting model, $\mathbf{m_0}$, and neglecting second-order terms. A linear problem can be formulated in terms of modified data, $\mathbf{d}'$, written as

$$\mathbf{d}' = \mathbf{d} - \mathbf{d}(\mathbf{m_0}) + \mathbf{A}\mathbf{m_0} = \mathbf{A}\mathbf{m}, \tag{2.12}$$

where the Jacobian matrix is defined as

$$A_{ij} = \frac{\partial d_i(\mathbf{m}_0)}{\partial m_j}. \tag{2.13}$$

The solution to this problem, following Eq. (2.9), results in a new model, $\mathbf{m_1}$. As linearization is not exact, due to the elimination of higher-order terms, multiple iterations are required for solution convergence. This is carried out by updating $\mathbf{m_0}$ in Eq. (2.12) with $\mathbf{m_1}$ before carrying out each subsequent iteration. It is important to note that linearized inversion is an approximation, and that due to linearization errors the iterative solution may not converge or the parameter uncertainty estimates may be a poor approximation to the actual uncertainties.

The linearization theory presented above can be applied to localization problems by representing $\mathbf{d}$ with TOADs, and $\mathbf{m}$ with a 3D position coordinate $(x, y, z)$ representing source position. The forward problem for short-range propagation from source to the $i$th receiver (hydrophone) located at $(X_i, Y_i, Z_i)$ can be expressed

$$t_i = t_0 + \frac{1}{v}\sqrt{(X_i - x)^2 + (Y_i - y)^2 + (Z_i - z)^2}, \tag{2.14}$$

for $i = 1, ..., H$, where $H$ is the number of receivers, $t_0$ is the source instant, and $v$ is the water sound speed. As the data correspond to arrival-time differences, not arrival times, they can be expressed as $d_i = t_{i+1} - t_1$, for $i = 1, ..., H - 1$ with $t_1$ being the arrival time for hydrophone 1, which is assumed to be the reference. This has the effect of removing the unknown source instant from the problem.

For this study, localization via linearized inversion worked most of the time, but in some cases diverged rather than converged, and did not provide a solution. Further, analysis showed that in some cases the uncertainty distributions were significantly affected by linearization errors. Hence, a fully-nonlinear localization method based on a 3D grid search was also developed.

### 2.2.2 3D Grid Search

To formulate a nonlinear localization approach, a 3D grid of points in $(x, y, z)$, with each point representing a potential source position, is defined over the volume in space bounded by the estimated maximum distance the whale could have been in each dimension. A uniform prior probability is defined over the grid, and a zero prior outside of the grid. To compute the unknown data standard deviation, predicted TOAD data and the summed-squared misfit $|\mathbf{d} - \mathbf{d}(\mathbf{m})|^2$ to the observed data are computed for every grid point $\mathbf{m}$. The grid point that minimizes this summed-squared misfit represents the ML position estimate $\hat{\mathbf{m}}$ and can be applied in Eq. (2.8) for the standard deviation estimate $\hat{\sigma}$. Applying $\hat{\sigma}$ to Eq. (2.7), and neglecting normalization terms leads to a non-normalized likelihood estimate

$$L(\mathbf{m}, \hat{\sigma}) \propto \exp\left[-\frac{1}{2\hat{\sigma}^2}|\mathbf{d} - \mathbf{d}(\mathbf{m})|^2\right]. \tag{2.15}$$

Normalization is achieved by summing the non-normalized likelihood function over all grid points and dividing each point by this sum. The result is a normalized PPD in 3D, with the estimate of source position being the grid point with the ML value. It should be noted that this solution is limited only by the discretization of the size of the grid. In this study a grid spacing of 10 cm was used in all dimensions, which appeared sufficient for accurate estimates. Since this approach directly yields probability values for each point on a (regular) 3D search grid, computing one-dimensional (1D) or two-dimensional (2D) marginal probability densities requires only integrating (summing) over the required dimensions.

### 2.2.3 Localization Method Comparison

This section compares the localization results from both methods described above on two synthetic data sets — the first involving a source-array geometry that provides good localization information and the second corresponding to a poorer geometry. The true source positions and the added synthetic noise are identical between localization methods. Hydrophone array geometry in this study will be further discussed in Chapter 3; however, briefly: 23 hydrophones are arranged within a roughly 2 m × 2 m rectangular plane in $(x, z)$, with relatively small position difference in $y$. This arrangement corresponds to the 2020 array configuration.

The first localization example considers a source that is perpendicular to the $(x, z)$ plane of receivers (representing a RKW directly in front of a hydrophone array), at a position of $(x, y, z) = (0, 30, 0)$ m. Gaussian random errors, with a standard deviation of 5 $\mu$s, are added to the TOADs and the source position and its uncertainties are estimated via linearization and via 3D grid search. Localization via linearization leads to a source position estimate of $(x, y, z) = (-0.03, 28.3, -0.05)$ m corresponding to a range of 28.3±3.4 m, with positional standard deviations of $(0.1, 3.4, 0.1)$ m. A 3D grid was set up and bounded by $-0.5$-0.5 m in $x$, 15-45 m in $y$, and $-0.5$-0.5 m in $z$. The grid spacing was 0.01 m in $x$, 0.1 m in $y$, and 0.01 m in $z$, for a total of $3,070,501$ grid points (a finer grid spacing was used in this example to smooth the uncertainty estimates). Localization via 3D grid search leads to a source position estimate of $(x, y, z) = (0, 29.3, 0)$ m corresponding to a range of 29.3±4.5 m, with positional standard deviations of $(0.2, 4.5, 0.2)$ m. Figures 2.1 and 2.2 show the 1D and 2D marginal probability distributions for the localization results, respectively. In this example, both localization methods produce similar source position estimates, although the uncertainty estimates are higher for the grid search. The structure of the probability distribution of the grid search resembles a Gaussian distribution suggesting that linearization for this source-receiver geometry is a reasonably good approximation. It is important to recognize that although the uncertainty estimates are smaller for linearized inversion, these represent an approximation, while the non-linear inversion produces exact results (within the limits of the grid).

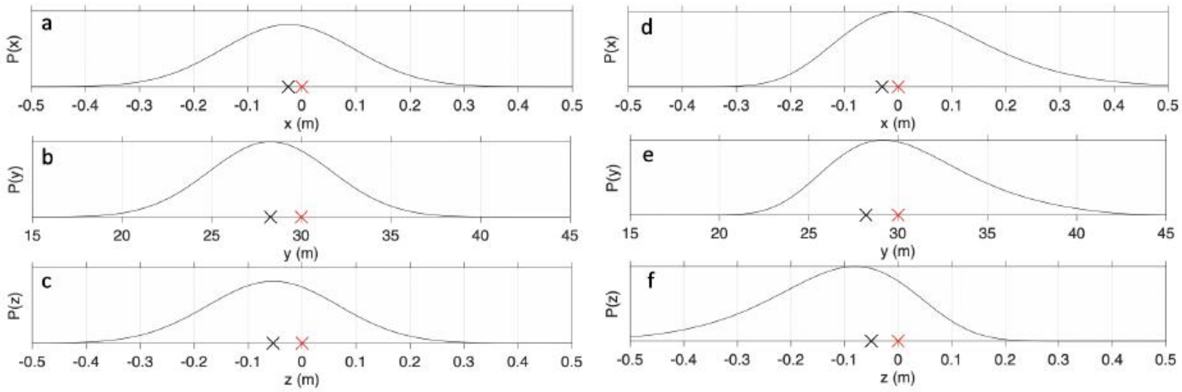

Figure 2.1: 1D marginal probability distributions for a source at 30 m, perpendicular to the $(x, z)$ plane of the receivers, localized via linearization (a)-(c) and 3D grid search (d)-(f), respectively. The red and black "x" represent the true and estimated source positions, respectively.

The second localization example considers a source at a relatively large distance in all three components with $(x, y, z) = (20, 40, 35)$ m, corresponding to a range of 56.8 m. Localization via linearization leads to a source position estimate of $(x, y, z) = (20.1, 39.8, 35.1)$ m corresponding to a range of 56.7±5.8 m, with positional standard deviations of $(3.4, 6.4, 5.5)$ m. A 3D grid was set up and bounded by 10-40 m in $x$, 20-80 m in $y$, and 20-70 m in $z$. The grid spacing was 0.1 m for all coordinates, resulting in a total of $90,932,502$ grid points. Localization via grid search leads to a source position estimate of $(x, y, z) = (20.2, 39.9, 35.2)$ m corresponding to a range of 56.9±10.1 m, with positional standard deviations of $(5.9, 11.2, 9.7)$ m. Figures 2.3 and 2.4 show the 1D and 2D marginal probability distributions for the localization results, respectively. Once again the source-location estimate is virtually identical between methods but the standard deviations from the grid search are

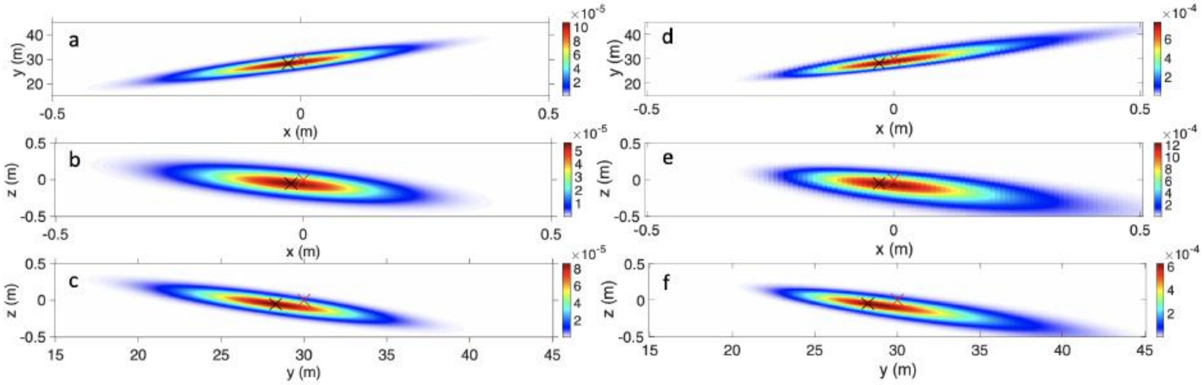

Figure 2.2: 2D marginal probability distributions for a source at 30 m, perpendicular to the $(x, z)$ plane of the receivers, localized via linearization (a)-(c) and 3D grid search (d)-(f), respectively. The red and black "x" represent the true and estimated source positions, respectively.

almost twice as large as for linearized approximations. Figure 2.3 shows that, for this example, the linearized approximation to uncertainty distributions is not a good representation of the actual distributions captured by grid sampling, which suffers no linearization errors. In particular, the linearized distributions (Gaussians) do not capture the asymmetry and long "tails" to large ranges evident in the non-linear (gridded) solution. This asymmetry indicates that the TOAD data have less information to discriminate source positions that are too far than too close. This is consistent with the fact that source-distance information is primarily due to wavefront curvature which changes more slowly at larger distances. The 2D marginals in Figure 2.4 illustrate how the localization provides excellent directional estimates but much poorer range estimates.

Due to occasional divergence and inaccuracy of uncertainty estimates for linearized localization, the grid search was used for localizations needed for data analysis in this thesis. A grid search may not always be feasible for large search volumes as the required computational time increases geometrically with volume. For this study, however, prior knowledge of approximate whale positions allowed for a relatively small volume to be searched (leading to finer grid spacing), and computational time was not a concern. For example, a grid search based on $10^8$ grid points required only 1-2 minutes of computation time in MATLAB on a laptop computer, taking advantage of partial parallelization.

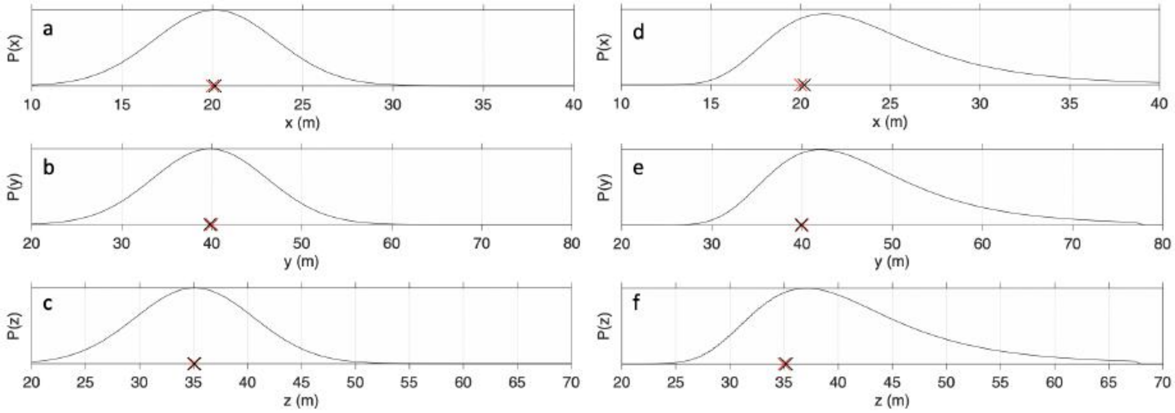

Figure 2.3: 1D marginal probability distributions for a source at 58.7 m, at a significant angle to the normal to the plane of receivers, localized via linearization (a)-(c) and 3D grid search (d)-(f), respectively. The red and black "x" represent the true and estimated source positions, respectively.

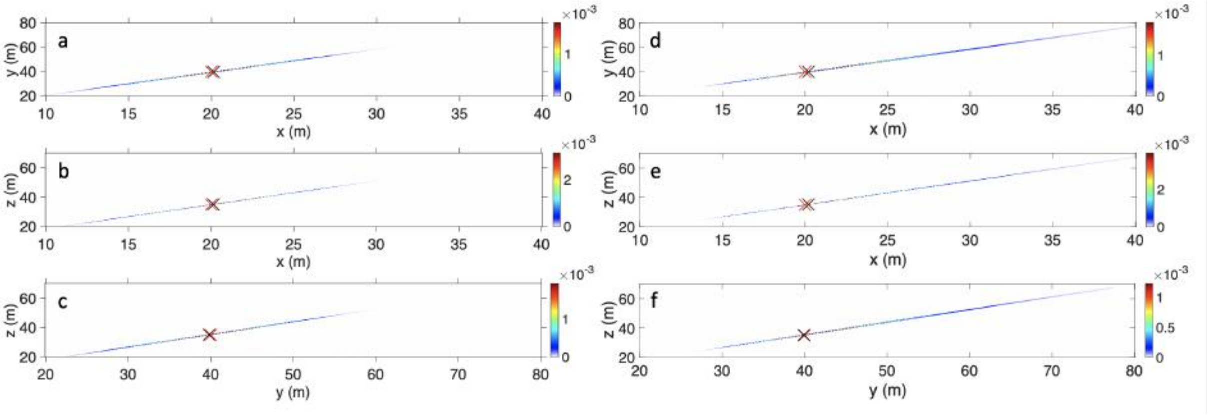

Figure 2.4: 2D marginal probability distributions for a source at 58.7 m, at a significant angle to the normal to the plane of receivers, localized via linearization (a)-(c) and 3D grid search (d)-(f), respectively. The red and black "x" represent the true and estimated source positions, respectively.

# Chapter 3

# Fieldwork and Instrumentation

This chapter describes the methods by which an acoustic array and data acquisition system was designed, constructed and transported to RKW critical habitats. It outlines the techniques used to search for RKWs and record echolocation click data. Finally, it details the hydrophone calibration procedure used to measure each hydrophone's sensitivity, necessary to extract acoustic characteristics from the data.

## 3.1 Fieldwork Set-Up and Data Acquisition

RKW echolocation click data were gathered over two field seasons: June to August 2019, and August to October 2020. A polyvinyl chloride (PVC) array frame was designed and constructed to hold 20+ hydrophones, and was secured to a 7 m long *Zodiac Hurricane* rigid hull inflatable boat (RHIB). Specifications for the two types of hydrophones used to acquire data are outlined in Section 3.1.1. The array design and construction for the 2019 field season, and its subsequent redesign for the 2020 field season, are discussed in Sections 3.1.2 and 3.1.3, followed by a simulation study carried out to compare localization between the two years. Finally, techniques used to search for RKWs and position the array are outlined in Section 3.1.5.

The majority of SRKW encounters took place in a 50 km radius around Swiftsure Bank, between Vancouver Island and Washington state, a salmon-rich area frequently foraged by RKWs. A few encounters occurred in Haro Strait adjacent to San Juan Island. In 2019, SRKWs were encountered in just 2 of 14 field days, while in 2020, they were encountered in 11 of 21 field days. Figures 3.1 and 3.2 show the routing and search areas for SRKW data collection in the 2019 and 2020 field seasons, respectively. The RHIB was based out of three departure points depending on available information about SRKW locations: Beecher Bay Marina, Port Renfrew Marina, or Sidney Marina. The NRKWs were encountered in 6 of 7 days, near Telegraph Cove on the northeast side of Vancouver Island (N 50°37′48″ W 126°46′48″). Figure 3.3 shows the routing and search areas for NRKW data collection in 2019. Through both field seasons approximately 6200 km were traveled over 42 days, searching for and recording RKWs.

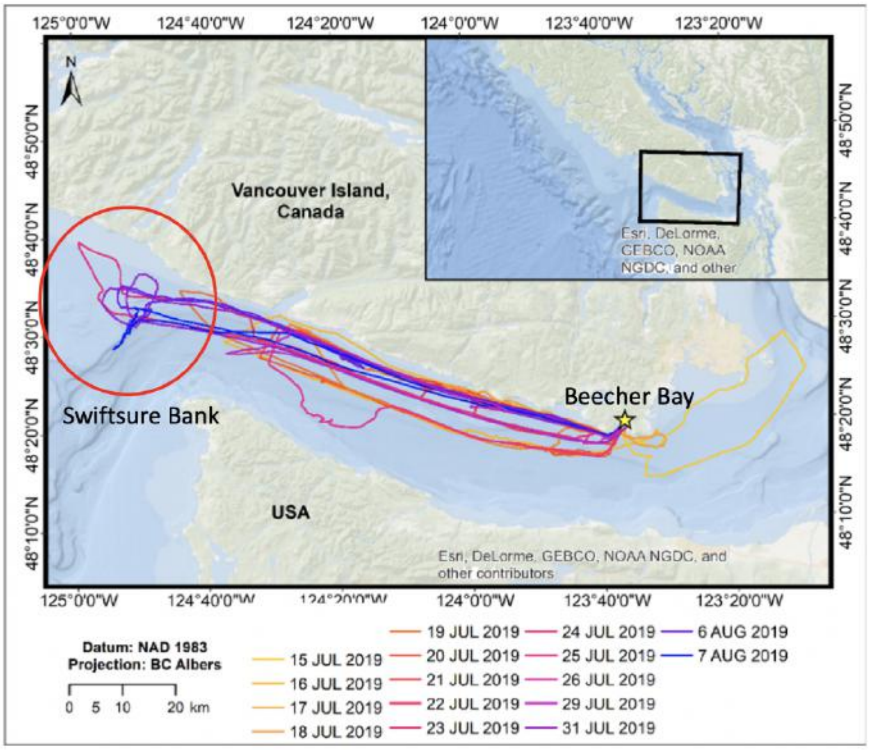

Figure 3.1: Search routing for 2019 SRKW data collection. Red circle shows the approximate position of Swiftsure Bank.

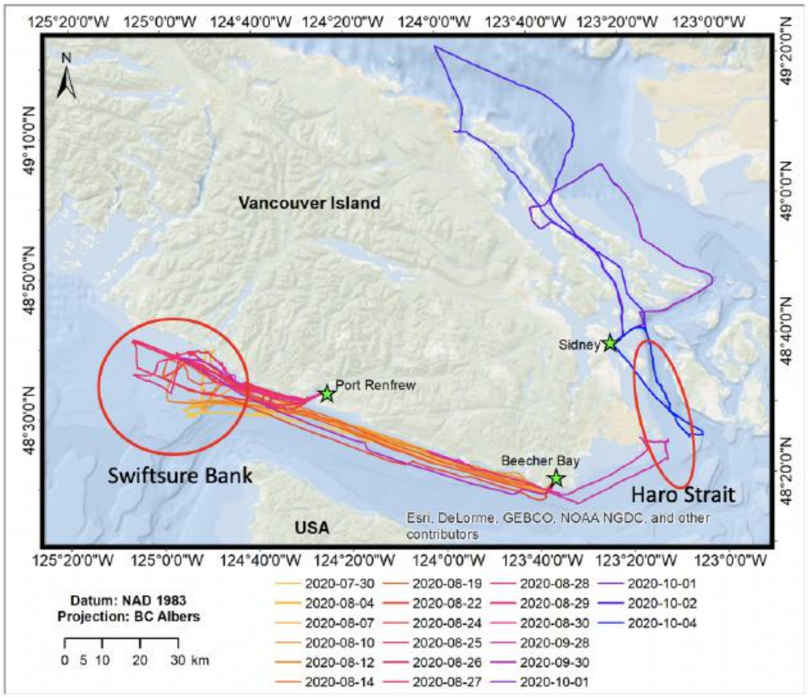

Figure 3.2: Search routing for 2020 SRKW data collection. Red circle shows the approximate position of Swiftsure Bank.

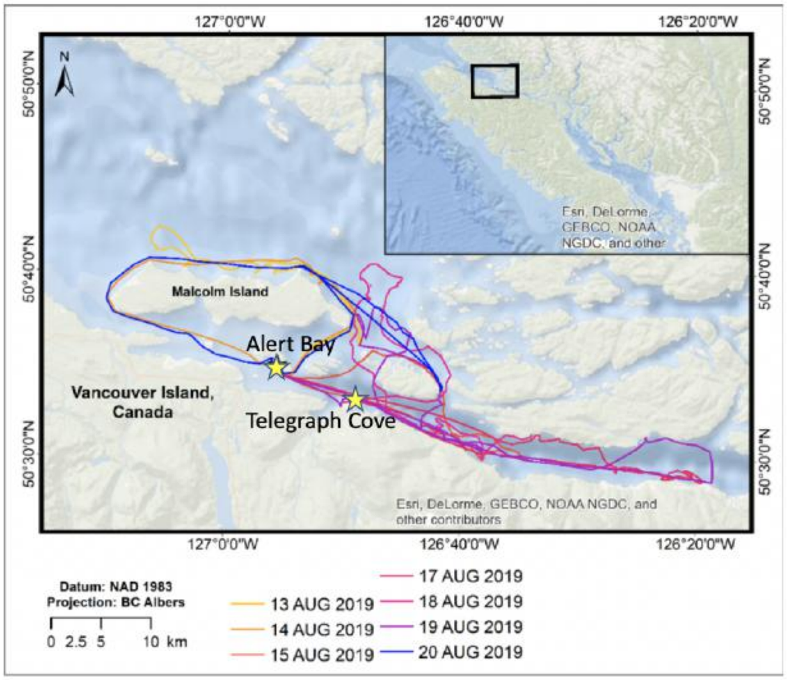

Figure 3.3: Search routing for 2019 NRKW data collection.

### 3.1.1 Acoustic Measurement System

A total of 20 hydrophones were available in 2019, and 23 hydrophones in 2020, for constructing the acoustic array to record echolocation clicks. Sixteen Reson TC-4013 hydrophones were provided by collaborator Jens Koblitz (manufacturer's sensitivity $-215$ dB re 1V/$\mu$Pa; flat (±5 dB) frequency response 1-150 kHz). Additionally, seven Geospectrum M36 hydrophones were purchased for this project (five with sensitivity $-165$ dB re 1V/$\mu$Pa, two with sensitivity $-170$ dB re 1V/$\mu$Pa; flat (±5 dB) frequency response 1-200 kHz). The Reson hydrophones were pre-amplified by 38 dB through a custom built 16 channel amplifier, while the M36 hydrophones were not externally amplified. Data from both hydrophone types were converted from analog to digital via a National Instrument A/D converter (PXI-6123) with 16 bit resolution at a sampling rate of 500 kHz. Custom-written software called MALTA (Microphone Array Localization Tool for Animals, CAE Software and Systems), installed on a laptop computer, provided a user interface on-board the RHIB which provided a real-time display of recorded signals via a moving-spectrum display. MALTA packaged the data into a 5 s files 5 MB in size for each hydrophone. For example, a two-minute recording produced a total of 2.76 GB of stored data (24 files, 23 hydrophones, 5 MB per file).

### 3.1.2 2019 Hydrophone Array Design

The hydrophone array was designed and built to satisfy a number of conditions required to effectively record RKW echolocation clicks. Source localization requires the positions of the hydrophones be known to high precision with respect to each other. Therefore, the array frame needed to be rigid so the relative sensor positions remained fixed. Given the initial goal of measuring the beamwidth of echolocation clicks, the array was designed as a 2D grid of hydrophones. The sensors were approximately evenly-spaced over a grid size of about 2 m × 2 m, which represented the largest array that could be conveniently transported and deployed using the RHIB. Figure 3.4 shows the array configuration in 2019. The array frame was made of PVC piping, fastened with plastic screws and nuts. The small, light-weight Reson hydrophones were deployed in a four-by-four evenly-spaced array grid, while the larger M36 hydrophones were attached to the outside array frame, increasing its aperture.

The array was secured to the RHIB by resting on a wooden frame bolted to the RHIB superstructure. The bottom of the array fit into a trough designed to limit

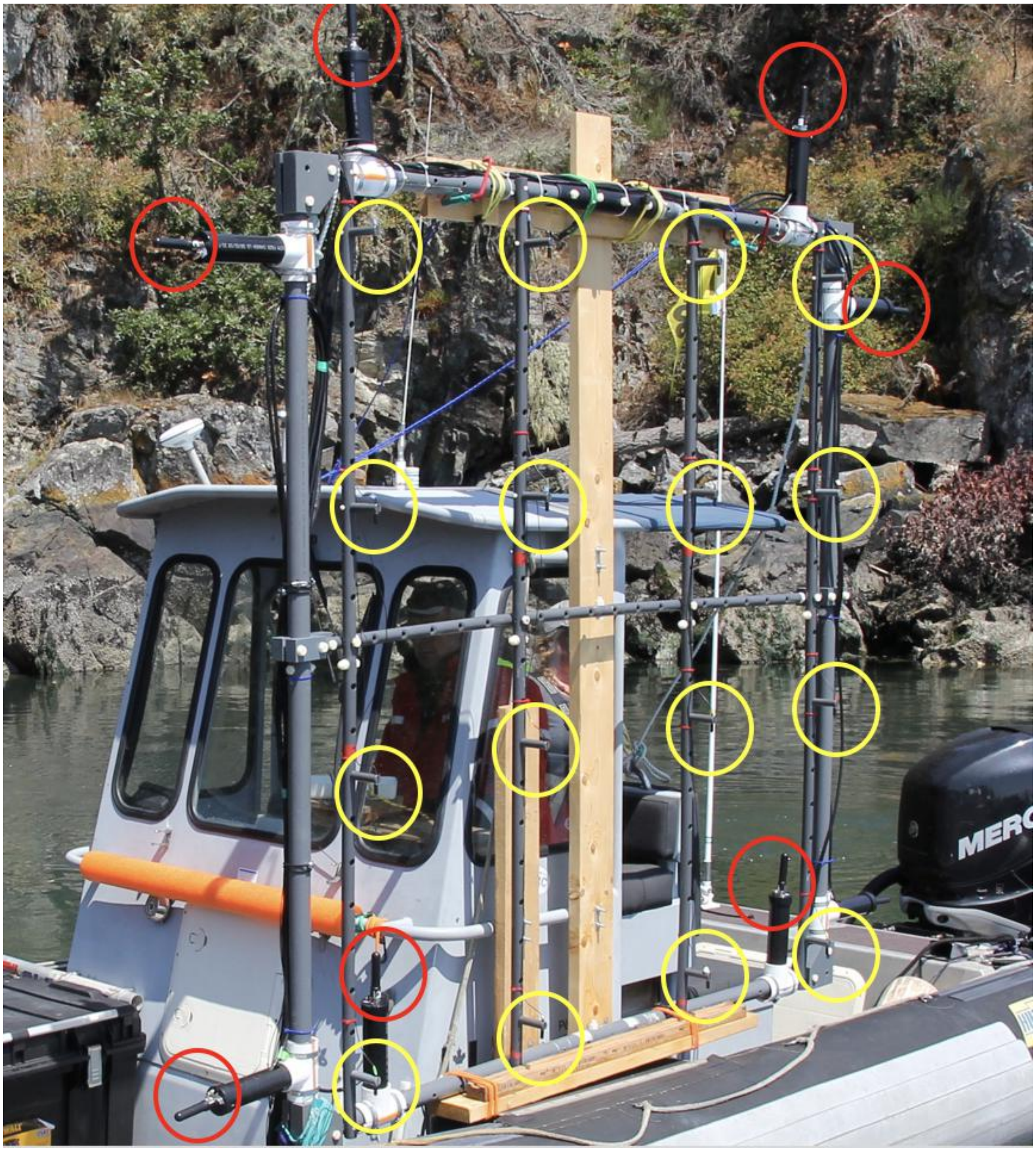

Figure 3.4: Hydrophone array configuration for 2019, mounted on the side of the RHIB. Yellow and red circles show Reson and Geospectrum hydrophones, respectively.

its movement abeam the hull, while two hooks held the top of the array limiting its fore and aft movement. While the RHIB was underway, several bungee cords were required to supplement its stability. Still, on two occasions fieldwork was ceased for the day due to damage to the frame requiring repairs to be carried out from the marina.

Reasonably good source position localization success was achieved with this array configuration; however, post-analysis showed that uncertainties could be improved. Before the 2020 field season, the array was redesigned and reconstructed in an attempt to improve source localization (reduce positional uncertainties), as discussed in the following section.

### 3.1.3 2020 Hydrophone Array Design

The main issue with localizing an acoustic source (e.g., echolocating whale) with a small planar array is that the hydrophone geometry provides good information on the direction to the source but poorer ability to estimate the range for long-range sources. In our work, the array-based coordinate system is defined with the positive $y$ axis perpendicular to the plane of the array away from the RHIB (the intended direction towards RKWs), the $x$ axis horizontal parallel to the array, and the $z$ axis positive downward. The 2019 version of the array had virtually no aperture between hydrophones in the $y$ direction (i.e., out of the plane of the array), since a flat array was easier to build, transport, and deploy. Increasing the array aperture in the $y$ axis was expected to improve localization accuracy. This was achieved by the addition of array "arms" that jutted out at approximately 30-45° angles from the sides of the array frame. This increased the distance between hydrophones in the $y$ direction up to 20 cm, and further increased aperture in the $x$ direction by up to 56 cm. The arms were constructed using PVC piping and hydrophones secured to the ends via hose clamps. Figure 3.5 shows the 2020 array configuration secured to the RHIB with added arms. Figure 3.6 shows the 2020 array with all hydrophones installed on it.

The addition of the PVC arms led to difficulties associated with array deployment and recovery by adding weight to the frame. Furthermore, the moment associated with each M36 hydrophone on the end the arms led to apparatus instability during RHIB transits. The solution to this was the design of an improved array frame securing and deployment device that included a pulley system, also shown in Figure 3.5. This system better secured the array to the RHIB and increased the ease and speed of array deployment and recovery.

The success of the redesign became immediately apparent during the second field season, through the reduction in time and effort required for deployment. Furthermore, no substantial damage was sustained to the array through the entirety of the fieldwork in 2020, due to improved array stability.

Figure 3.5: Hydrophone array configuration for 2020. Red circles show the new positioning of the M36 Geospectrum hydrophones. Yellow circle shows the newly installed pulley system. The Reson hydrophones had not been installed at the time of this photo.

Figures 3.7 and 3.8 show underwater views of the 2019 array following its deployment from the RHIB.

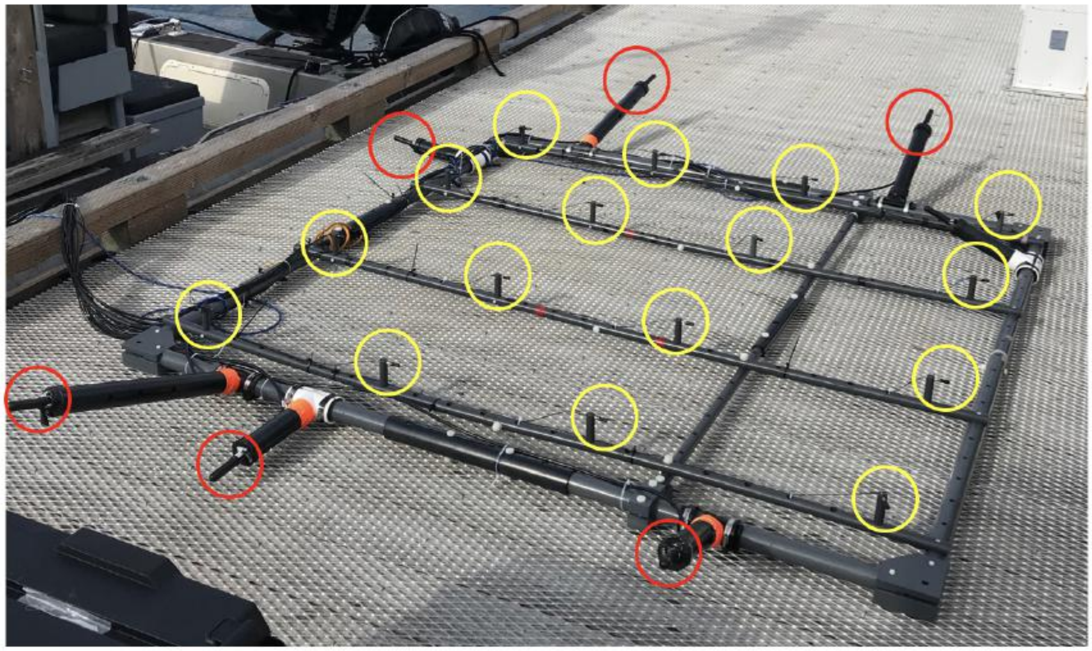

Figure 3.6: Hydrophone array configuration for 2020. Yellow and red circles show positioning of Reson and Geospectrum hydrophones, respectively.

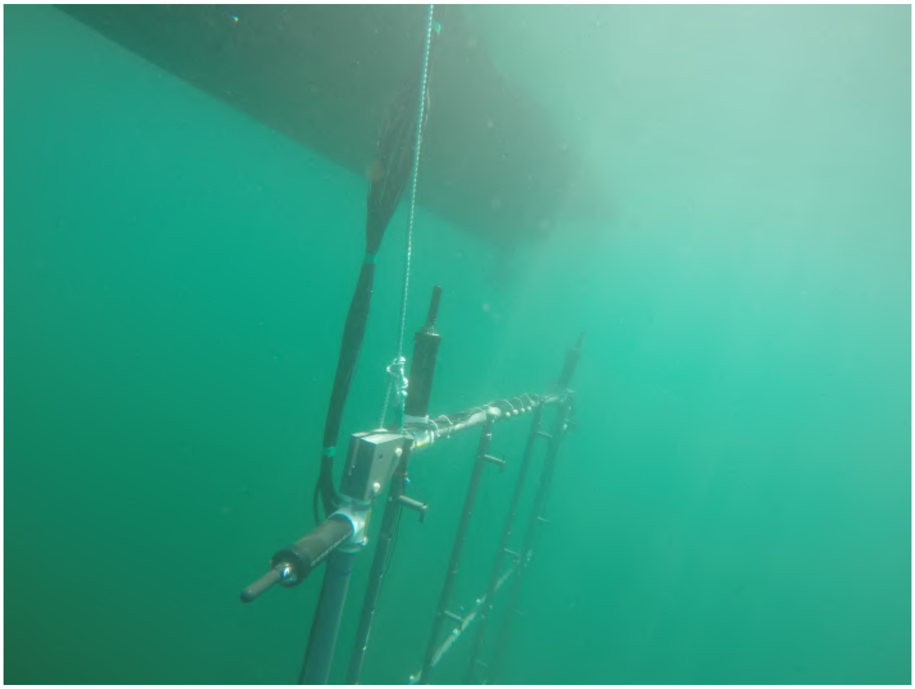

Figure 3.7: Underwater side view of the deployed array (2019) with the RHIB seen in the top left.

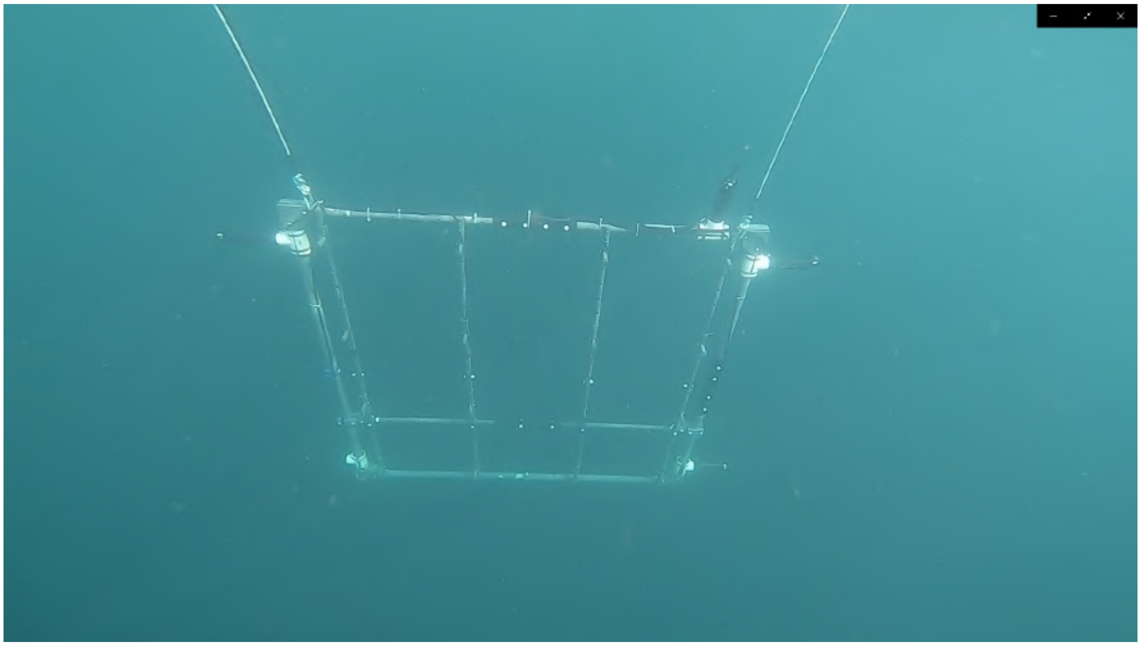

Figure 3.8: Underwater top down view of deployed array (2019).

### 3.1.4 Source Localization Uncertainty Modelling

This section presents the simulation study carried out to guide the array redesign between field seasons. A set of assumed whale positions was used to predict synthetic observed data (TOADs) at each hydrophone for each array configuration. Random Gaussian errors were added to these data, and a 3D grid search and misfit analysis was carried out to estimate source positions and associated uncertainties. For each position and configuration, the coefficient of variation (CoV), defined as the ratio of the standard deviation of the distance estimate to the true distance, was calculated to provide a quantitative assessment of the two arrays. Additionally, the accuracy of the estimated position was expressed as the absolute difference between the estimated and true distances divided by the true distance (converted to a percentage).

The following example illustrates the comparison of localization uncertainties for the two array configurations for a source located at $(x, y, z)$ = (10, 25, 5) m, at a source-to-array range of 27.4 m. Localization with the 2019 array data yields an estimated source position of $(x, y, z)$ = (10.8, 26.8, 5.3) m corresponding to a range of 29.4 m, with positional standard deviations of (6.3, 14.1, 2.4) m corresponding to a standard deviation in range of 13.1 m, for a CoV of 0.48, and a position error of 7.3%. For the 2020 array data the estimated source position is $(x, y, z)$ = (10.6, 26.4, 5.2) m corresponding to a range of 28.9 m, with positional standard deviations of (4.6, 10.5, 1.8) m corresponding to a standard deviation in range of 9.7 m, for a CoV of 0.35, and a position error of 5.5%. The percent decrease in CoV (difference divided by mean of the two values) and position error are 31.1% and 14.1%, respectively.

Figures 3.9 and 3.10 show the 1D and 2D marginal posterior probability distributions side-by-side for both array configurations, respectively. The improvement in localization accuracy from the 2019 to 2020 configurations can be seen through the reduction of the long tails to long ranges in both 1D and 2D distributions.

The same analysis was carried out for 1000 synthetic whale positions evenly spaced on a grid bounded by the maximum distances expected for useful whale positions during field work (±40 m in $x$, 20-80 m range in $y$, and 0-20 m in $z$). For each simulation, different random errors were applied, although held constant between configurations, and the CoV and percent position error were determined. Figures 3.11 and 3.12 show histograms of the results for the CoV and percent position error for the 1000 simulations carried out for each configuration.

The mean CoV for the 2019 configuration and 2020 configuration was determined

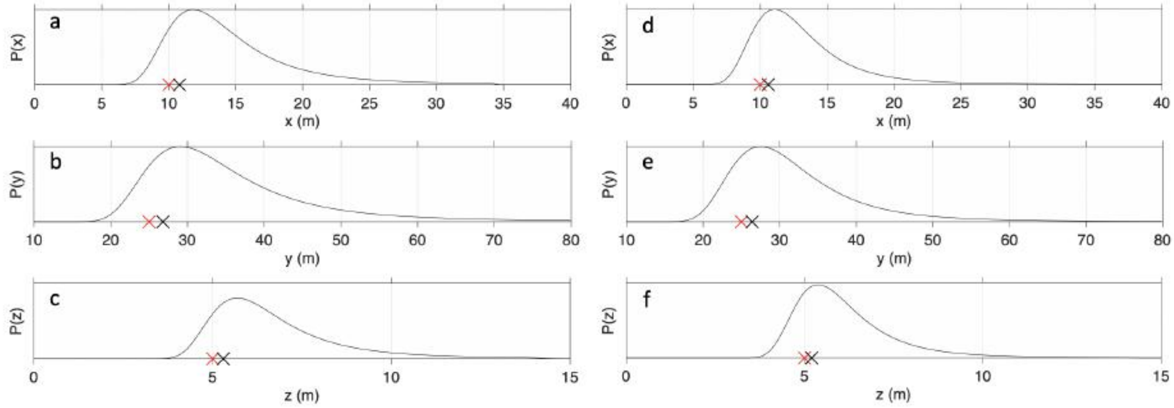

Figure 3.9: 1D marginal probability distributions for a source at 27.4 m, for the 2019 array configuration (a)-(c), and the 2020 array configuration (d)-(f), respectively. The red and black "x" represent the true and estimated source positions, respectively.

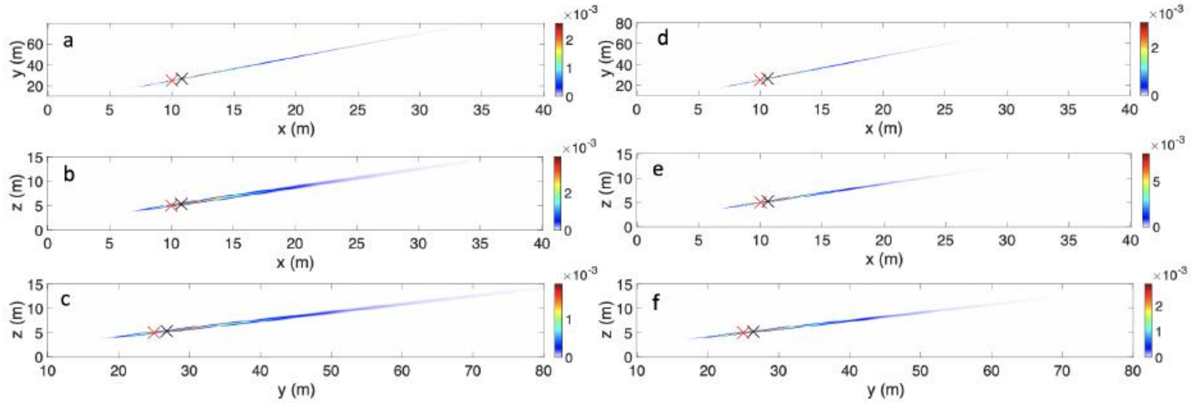

Figure 3.10: 2D marginal probability distributions for a source at 27.4 m, for the 2019 array configuration (a)-(c), and the 2020 array configuration (d)-(f), respectively. The red and black "x" represent the true and estimated source positions, respectively.

to be 0.30 and 0.22, respectively. The mean percent position error for the 2019 configuration and 2020 configuration was determined to be 23.7% and 20.9%, respectively. Expressed as an average of all synthetic test runs, the 2020 configuration improved upon the 2019 configuration uncertainty by 30.8% and the position accuracy by 6.3%.

While the uncertainty improvements were desirable, they ultimately did not influence the source level results significantly. The rate of change of PL due to spherical spreading decreases logarithmically as a function of range. Therefore, the uncertainty improvement at long ranges became insignificant compared to close ranges. Unfortunately, most of the click data collected in this study were from whales at ranges

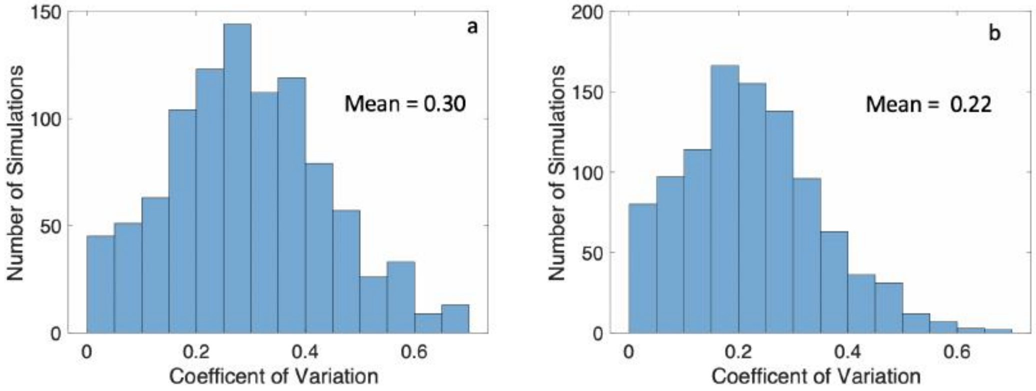

Figure 3.11: Histograms of CoVs calculated for 1000 localizations for the 2019 configuration (a) and 2020 configuration (b). The analysis shows an average uncertainty improvement of 15.4% from the 2019 to 2020 configuration.

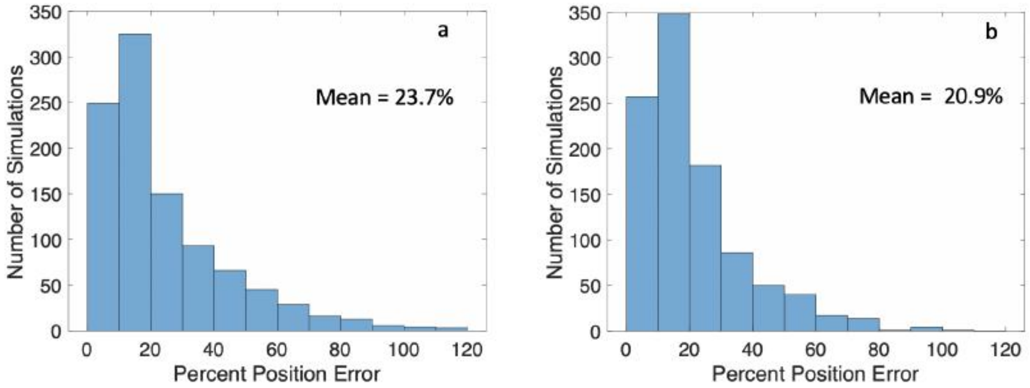

Figure 3.12: Histograms of the percent position error calculated for 1000 localizations for the 2019 configuration (a) and 2020 configuration (b). The analysis shows an average position accuracy improvement of 6.3% from the 2019 to 2020 configuration.

greater than 30 m. So, while the 2020 configuration proved superior to the 2019 configuration, the benefits were relatively minor.

### 3.1.5 RKW Search Procedure and Data Acquisition

The procedure for locating RKWs began by searching critical habitats based on reported sighting information, if available. Otherwise passive acoustic monitoring (PAM) would begin soon after exiting the harbour. Occasionally, RKWs would be

Figure 3.13: Listening for RKW calls and whistles.

Figure 3.14: Direction finding equipment.

encountered immediately upon reaching locations where sightings had been reported; however, often they were not and PAM was the best available search method. PAM was conducted by deploying a single hydrophone from the RHIB and monitoring it for RKW acoustic signals. If no whale calls or clicks were heard, the team would relocate approximately 15 km (double the estimated acoustic range of RKW calls) to a new position. If signals were heard, the omni-directional hydrophone would be converted to a direction tool using a wooden rod and metal bowl. Acoustically monitoring for RKW signals while rotating the apparatus underwater often led to a rough bearing to RKW positions. Figures 3.13 and 3.14 display the tools used to search for RKW acoustically. Locating groups of RKWs was only the first step towards successful data acquisition. Careful positioning of the RHIB prior to array deployment, based on behavioural predictions of RKW movements was required.

Other RKW studies illustrate the difficulties associated with array positioning for data acquisition. Odontocete behaviour has been characterized and reported in numerous studies, some of which include SRKWs [15] and NRKWs [16]. The SRKW study reported that of 289 one-minute time intervals in which whale behaviour was noted and the surrounding area acoustically monitored, echolocation clicks were found in only 66.4%. Furthermore, in only 27.3% of the intervals were the whales producing clicks while traveling in a constant direction. Otherwise they were spread out and frequently changing direction, probably searching for prey. This behaviour was apparent during attempts to position the RHIB — it was very difficult to accurately predict a whale's heading prior to array deployment. The development of a RHIB positioning procedure led to more success than simply deploying the array and hoping a whale would swim towards it.

This procedure consisted of positioning the RHIB approximately 500 m in front of the whales and maneuvering at very slow speeds (<10 km/h) to be in-line with the whales' estimated direction of travel. The engine was turned off and the array was lowered into the water to approximately 2 m depth. The vessel and array drifted with the current until the whales were more than 500 m away and did not appear to be returning. If a direction or pattern of RKW movements could not be discerned the array was deployed in the approximate vicinity of as many RKWs as could be observed visually. Even with these opportunistic approach procedures, data acquisition proved challenging.

The difficulty in recording RKW echolocation clicks can be assessed by comparing the number of array deployments during which high-quality data were recorded to the total number of deployment attempts. For both SRKW field seasons, high-quality data were recorded on 8 of 40 array deployments. Over the NRKW field season, high-quality data were recorded on 6 of 20 array deployments. In total, only approximately 23% of attempts led to useful data.

## 3.2 Hydrophone Calibration

The last step in the field work involved in-situ hydrophone calibrations, described in this section. Audio recording instruments have a tendency to experience changes in sensitivity characteristics over time, especially if exposed to harsh environmental conditions such as temperature changes or direct sun. The hydrophones used in this study were calibrated over two days with the assistance of DFO. Each of the 23 hydrophones were calibrated independently and a sensitivity response (calibration) curve was generated for each.

First, an acoustic source (transducer) was secured to the middle of a 3 m metal bar. A reference hydrophone (known sensitivity) was secured 1 m to one side of it, and the hydrophone to be calibrated was secured 1 m to the other side of it. This configuration is illustrated in Figure 3.15 for a Geospectrum hydrophone.

The apparatus was lowered to a depth of approximately 15 m, and a signal was produced by the transducer which was recorded for both hydrophones. The recorded signals were compared digitally using software called *HydroCal*. The software compared the two hydrophone responses at 40 frequencies between 2-100 kHz, and because the sensitivity response was known for the reference hydrophone, a response could be generated for the other. This process was carried out for each of the 23 hydrophones producing a calibration curve for each. Figures 3.16 and 3.17 present an example of the calibration curves measured for a Geospectrum and Reson hydrophone, respectively, together with the generic calibration curves provided by manufacturers, respectively.

An obvious difference between the measured calibration curves is the strong increase in sensitivity with frequency for the Reson hydrophone compared to the relatively flat response for the Geospectrum sensor. The difference appears to be due to the custom-build pre-amps included with the Reson hydrophones, although details are not available. The Reson calibrations were validated by comparison to the Geospectrum results for a common signal. Source level analysis showed that the Geospectrum sensors experienced saturation for some of the more powerful clicks. This led to signal clipping and erroneous source level determinations via these hydrophones. Therefore, the Reson hydrophones were used to extract source level values reported in this thesis. Source level results for less powerful clicks, for which the Geospectrum hydrophones did not saturate, were consistent between hydrophone types, validating the use of the Reson hydrophones.

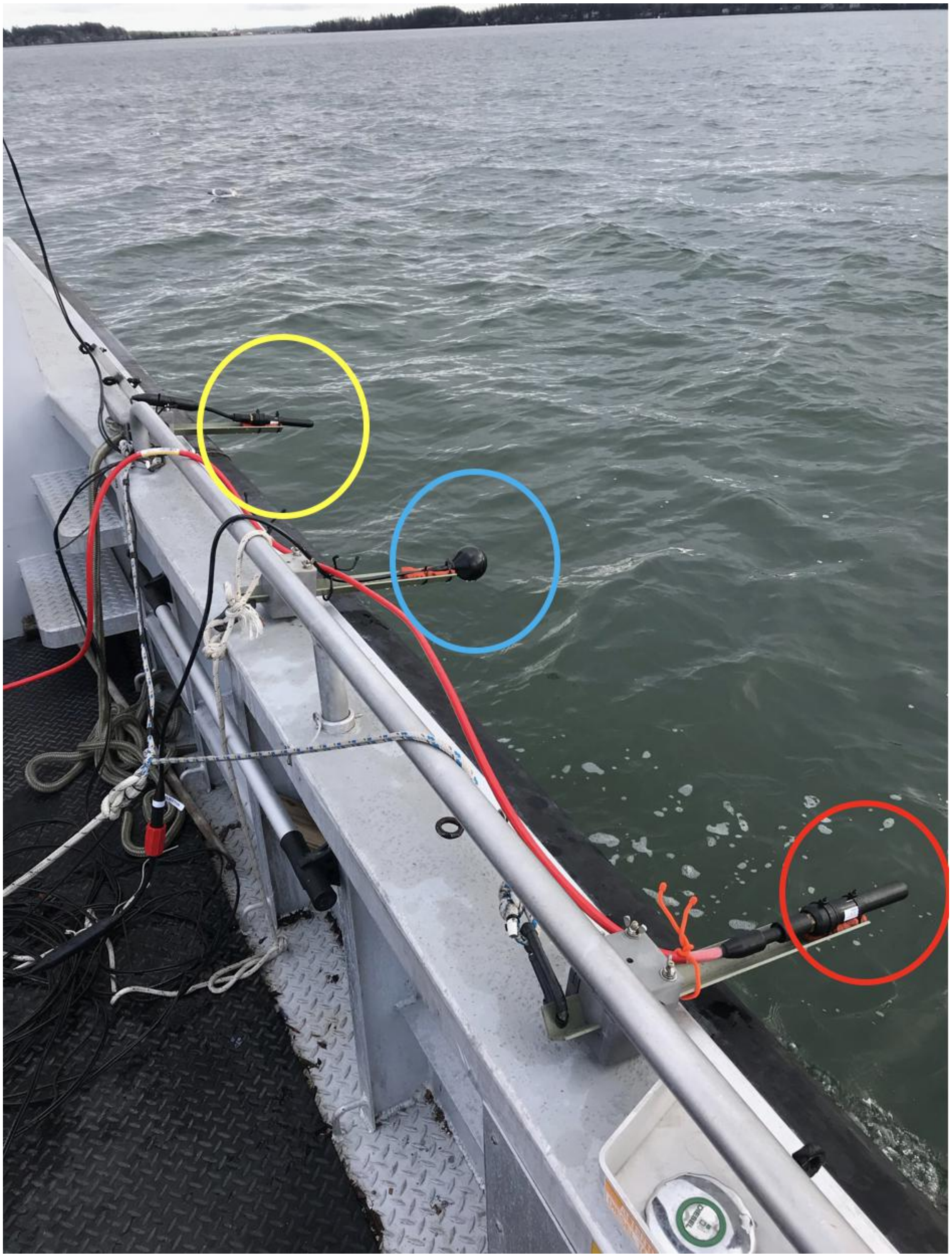

Figure 3.15: Hydrophone calibration configuration prior to deployment. Yellow, blue, and red circles show the reference hydrophone, transducer, and hydrophone under calibration, respectively.

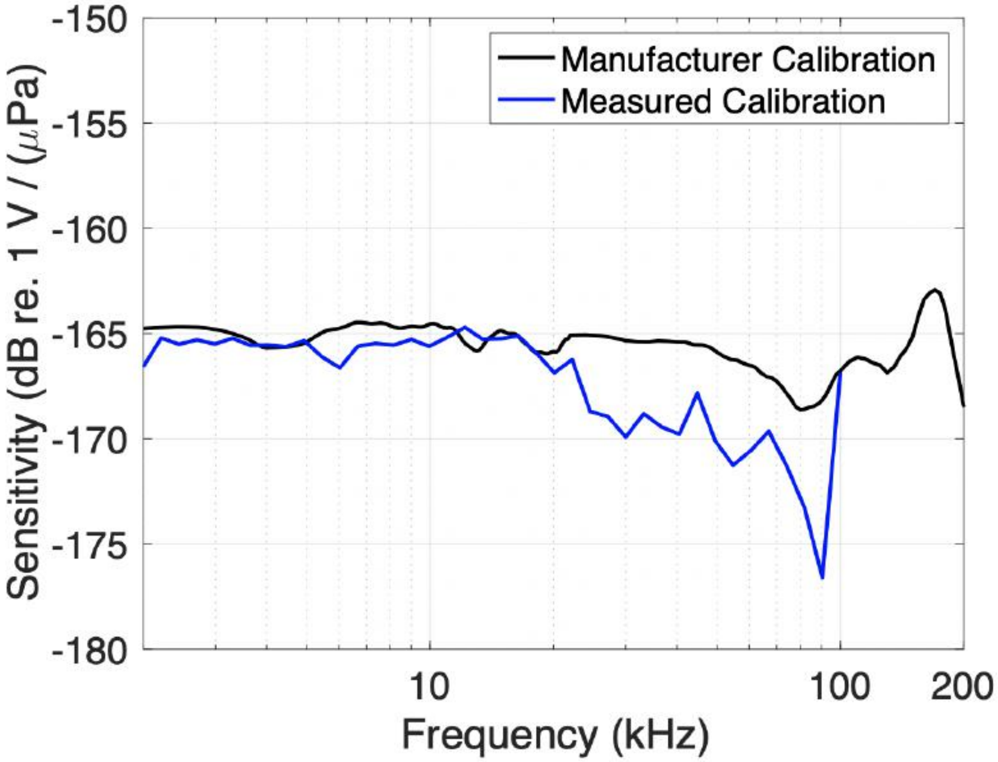

Figure 3.16: Calibration curves for one of the Geospectrum hydrophones used in this study. The blue curve was measured via the calibration procedure and the black curve was provided by the manufacturer.

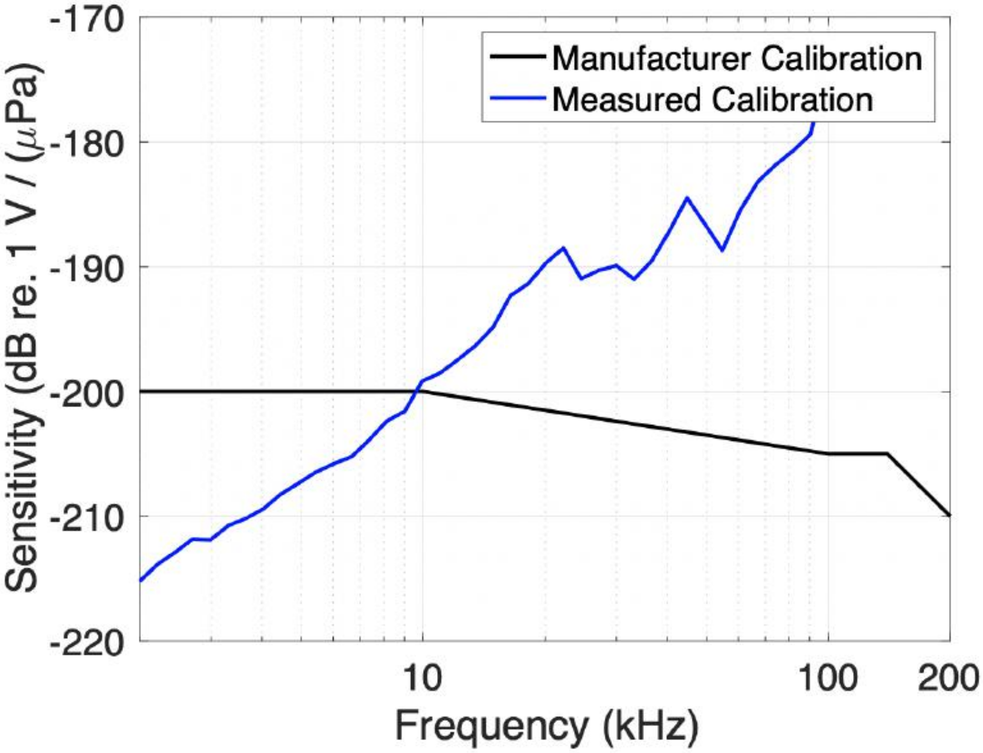

Figure 3.17: Calibration curves for one of the Reson hydrophones used in this study. The blue curve was measured via the calibration procedure and the black curve was provided by the manufacturer.

# Chapter 4

# Results

This chapter presents the results of the study: RKW echolocation click acoustic characteristics. The findings are partitioned by RKW type (NRKW or SRKW) and click type (slow, fast, or buzz).

The first section describes the criteria used to determine if data were of sufficient quality to be considered for analysis. Next, data processing methods used to extract spectral and temporal click characteristics are discussed. Finally, results are presented for every click train, and the largest amplitude click within each train, that met click-selection criteria.

## 4.1 Click-Selection Criteria

This section details the criteria used to include or discard echolocation click data based on its quality. A consequence of studying marine mammals in the wild versus in a controlled environment is that data must be gathered opportunistically. In controlled experiments, such as that of the harbour porpoise studied in [17], marine mammals can be trained to direct acoustic energy at a hydrophone from a known distance. This allows for a much more straightforward determination of PL as the source-to-receiver distance is known. Furthermore, there is no question of the directionality of the signal; that is, the animal can be trained to position itself such that its signal is directed on-axis. Recording whales in the wild means that the whale location and click direction are uncontrolled and unknown.

As an example, consider Figure 4.1, which shows approximately 18 clicks across 5 s of recording. Between approximately 2-4 s, the clicks appear to increase and then decrease in amplitude. In this example, it is difficult to discern whether the RKW is altering the loudness of the clicks it is producing, or if it is moving its head to scan across directions at a constant sound level. Estimating the actual source levels of the clicks (in the direction they were projected) depends strongly on this difference in behaviour. To address this concern, source level characteristics are only considered for the click with the greatest amplitude in each selected click train, since this click is most likely to have been directed towards the array and not represent an off-axis capture. Furthermore, following [18] and [19], a click train was only selected if it included at least 5 clicks, to maximize the likelihood that the RKW was clicking at the array.

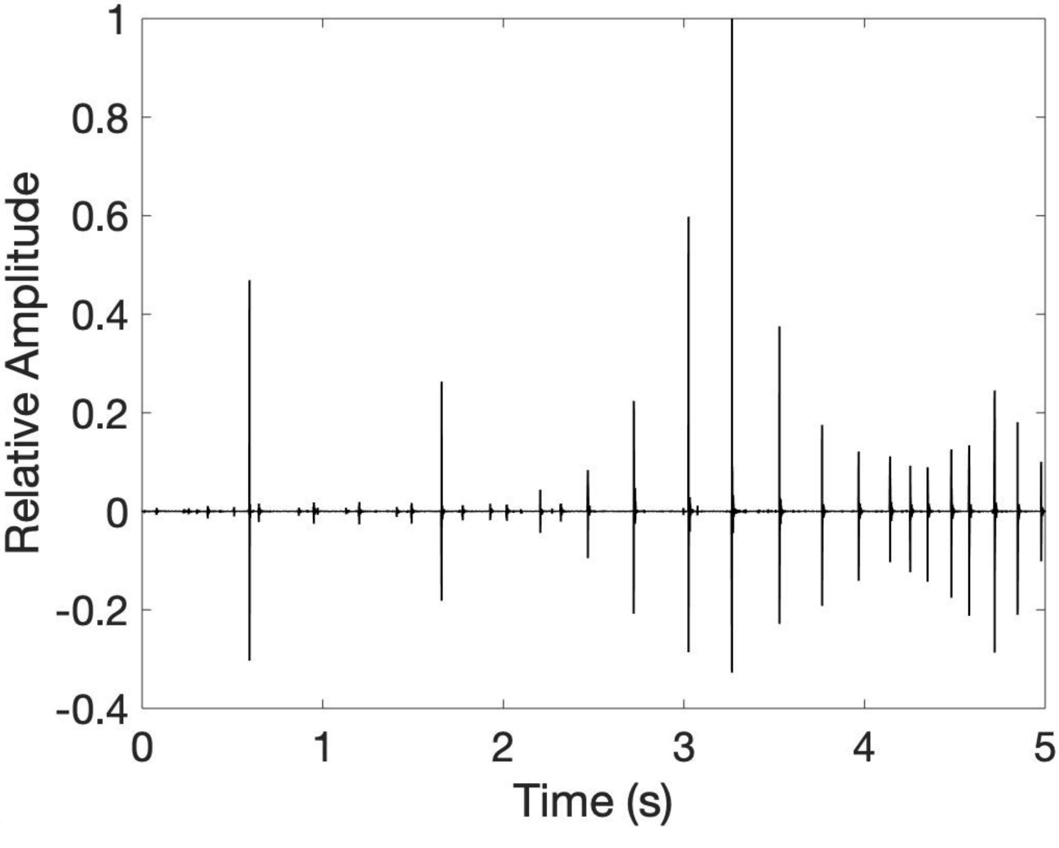

Figure 4.1: A slow-click train produced by a SRKW. The lower amplitude clicks between 0-3.5 s were produced by a different SRKW, supported by localization evidence, and therefore are not considered here. Time and location of recording: 25 August 2020, 13:11:57 UTC, Swiftsure Bank.

A concern in determining click duration is interference between the signal's direct path and reflections, both off of the air-water interface and the array itself. As an example, Figure 4.2 shows two clicks. While the signal duration can be easily identified in Figure 4.2(a) (approximately 120 $\mu$s), it is more difficult to assess where the direct arrival in Figure 4.2(b) ends, and where signal reflections may begin. While signal energy is apparent between 100-380 $\mu$s, it is highly likely, based on previous studies [9], that the click in Figure 4.2(b) is approximately the same length as in Figure 4.2(a), but is influenced by reflections. Including potential reflections in click duration estimates leads to erroneous results. Fortunately, the duration of most signals could be clearly discerned as reflections usually tended to be well separated in time (an example seen at 270 $\mu$s in Figure 4.2(b)).

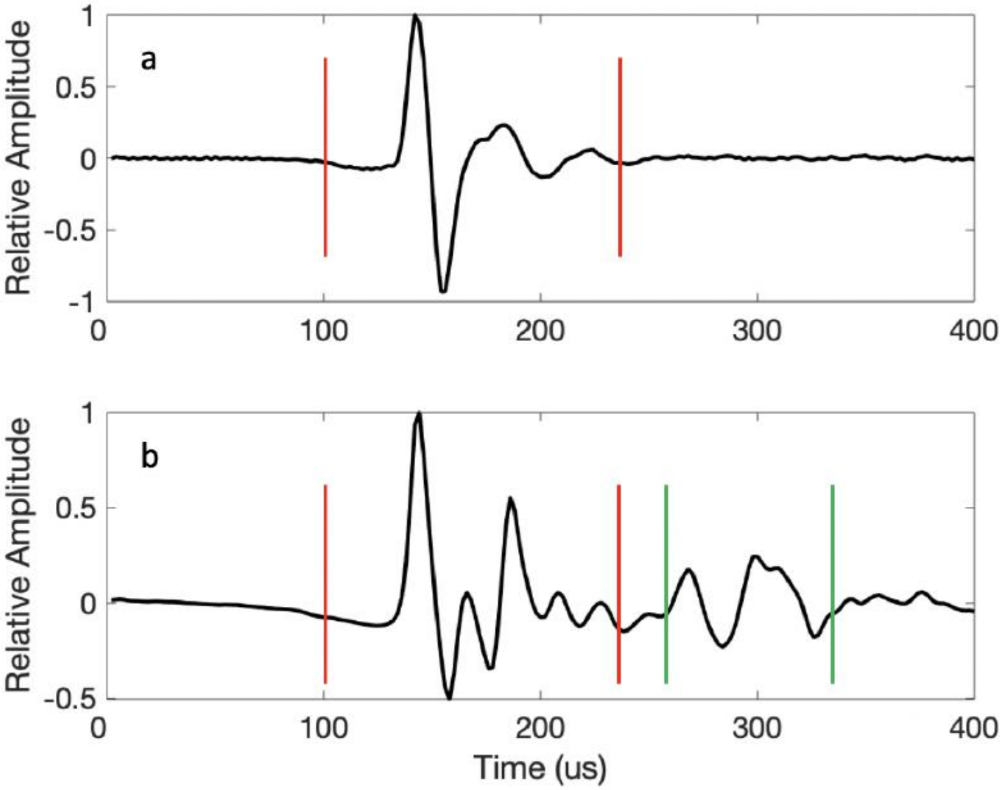

Figure 4.2: Two representative click waveforms. The signal's duration in (a) can be more easily discerned than in (b), due to the apparent presence of reflected energy in (b). The red lines in (a) and (b) show the estimated duration of the signal. The green lines in (b) show an area of potentially reflected energy.

Another issue for data quality involves the distance (range) the whale was from the array. Whale range estimates became increasingly uncertain the further the animal was from the array. Furthermore, the errors associated with signal cross-correlation were occasionally quite large, perhaps affected by signal reflections. To ensure acceptable levels of uncertainty, clicks were not considered if the RKW position was deemed too far, or too inaccurate.

The following echolocation click-selection criteria summarize whether a click train was selected for source level analysis:

- A click train must include at least 5 clicks;
- Click duration must be clearly discernible and separable from reflected energy;
- Source level is only reported for the greatest amplitude click within a click train; and
- The estimated source range from acoustic localization must be no further than 80 m — the approximate maximum range that was found to allow for an acceptable level of uncertainty in this study.

## 4.2 Echolocation Click Analysis

This section describes the analysis carried out on RKW click trains, and individual clicks therein, to estimate echolocation click acoustic characteristics of interest. In the time domain, these characteristics are click-train ICI, click duration, and peak-to-peak (PP) source level. In the frequency domain, these characteristic are peak frequency, centroid frequency, root-mean-square (RMS) bandwidth, and the location and power of a high-frequency secondary peak (HFSP), which is often present in the click spectrum [4] [9] [10]. Analysis was carried out using scripts written by the author of this thesis in MATLAB version 2019b.

Figure 4.3 shows a SRKW slow-click train of approximately 11 clicks, and its associated spectrogram. Results are presented as the voltage response of the recording system over a 3 s period. Note that the broadband lines at 60 kHz, 120 kHz, and 180 kHz appear to be due to electronic noise (and harmonics). Noise removal was carried out by subtracting the energy recorded on the same hydrophone, over an equal time period, in the absence of echolocation clicks, although some noise persisted. The electronic-noise appears in all spectrograms in this study but does not significantly affect any results. Figure 4.4 shows the same SRKW slow-click train after noise removal. It is interesting to note in Figure 4.4 that each large click has a much smaller secondary click directly after it. This is a phenomenon occasionally seen in echolocation click recordings, and is believed to be produced by the clicking whale through a secondary pair of phonic lips [7]. It was noticed in approximately 31% of all analyzed click trains recorded in this study — 6 SRKW click trains, and 5 NRKW click trains. Figure 4.5 shows a magnification of the time series of the two clicks, and Figure 4.6 shows the spectra of primary and secondary clicks. The majority of the energy lies in similar frequency bands for both clicks. However, little is known about the secondary click and they are not considered further in this study.

The click train spectrogram in Figure 4.4 shows the majority of energy in this click train falls within 10-60 kHz, with decreasing energy up to 130 kHz. This frequency range was commonly observed in much of the data analyzed here, and is consistent with other studies [9]. The position of the SRKW that produced this click train, relative to the array, was determined to be $(x, y, z) = (-57.3, 9.5, 18)$ m with standard deviations of $(x, y, z) = (11.1, 2.2, 3.4)$ leading to a range of 61±10.5 m.

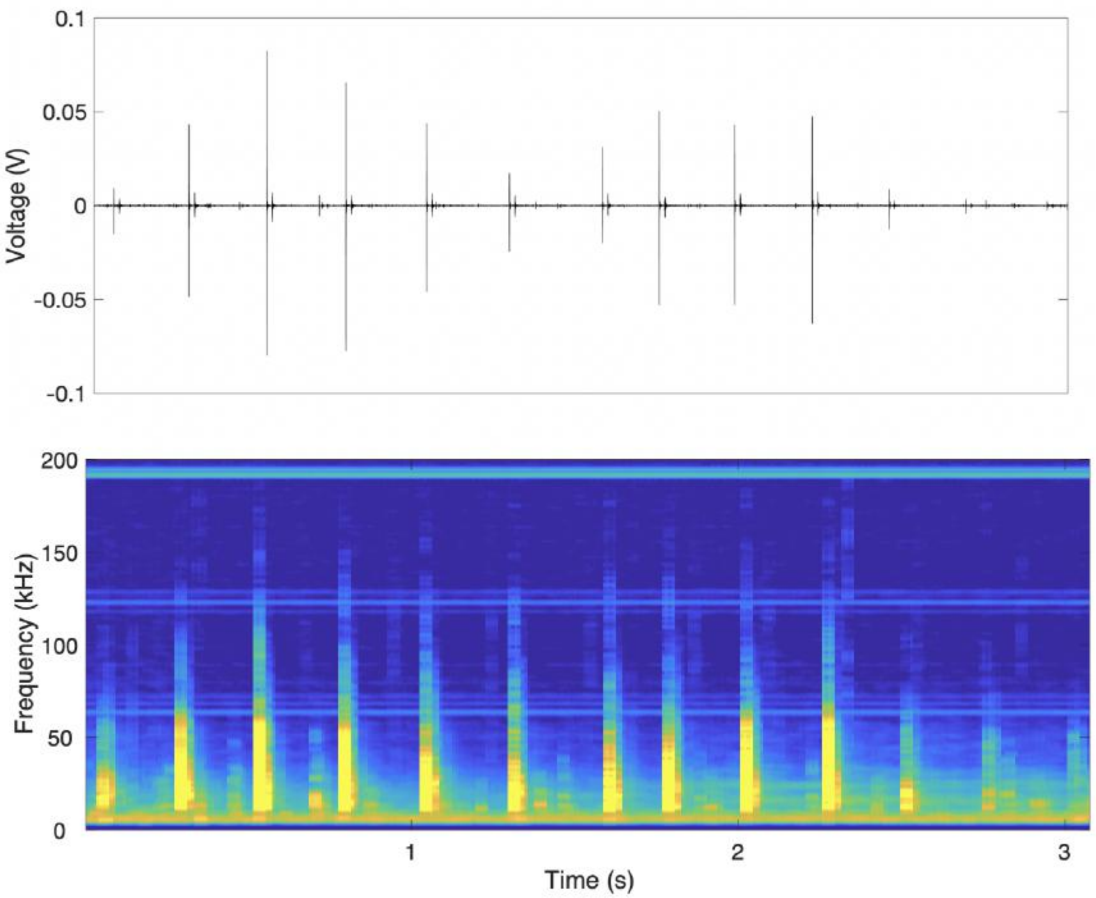

Figure 4.3: Example SRKW slow-click train in the time domain (top) and as a spectrogram (bottom) before noise removal. Time and location of recording: 27 August 2020, 12:43:01 UTC, Swiftsure Bank.

### 4.2.1 Echolocation Click Temporal Characteristics

The ICI of a click train was calculated by measuring the time between the peak amplitude of each click. The ICI values for the click train in Figure 4.4 are shown in Figure 4.7, and range from 179-287 ms, categorizing this train as a slow-click train based on the definition given in Chapter 1 (ICI $>$ 100 ms). The first 7 clicks were produced at a gradually increasing ICI, followed by a series of clicks at more variable ICIs.

The largest click within the click train was analyzed further for click duration. This click, shown in Figure 4.8, was visually analyzed and determined to have a duration of 90 $\mu$s, soon after which reflected energy appears to influence the waveform. Discussions with a whale biologist supported the conclusion that the oscillations near

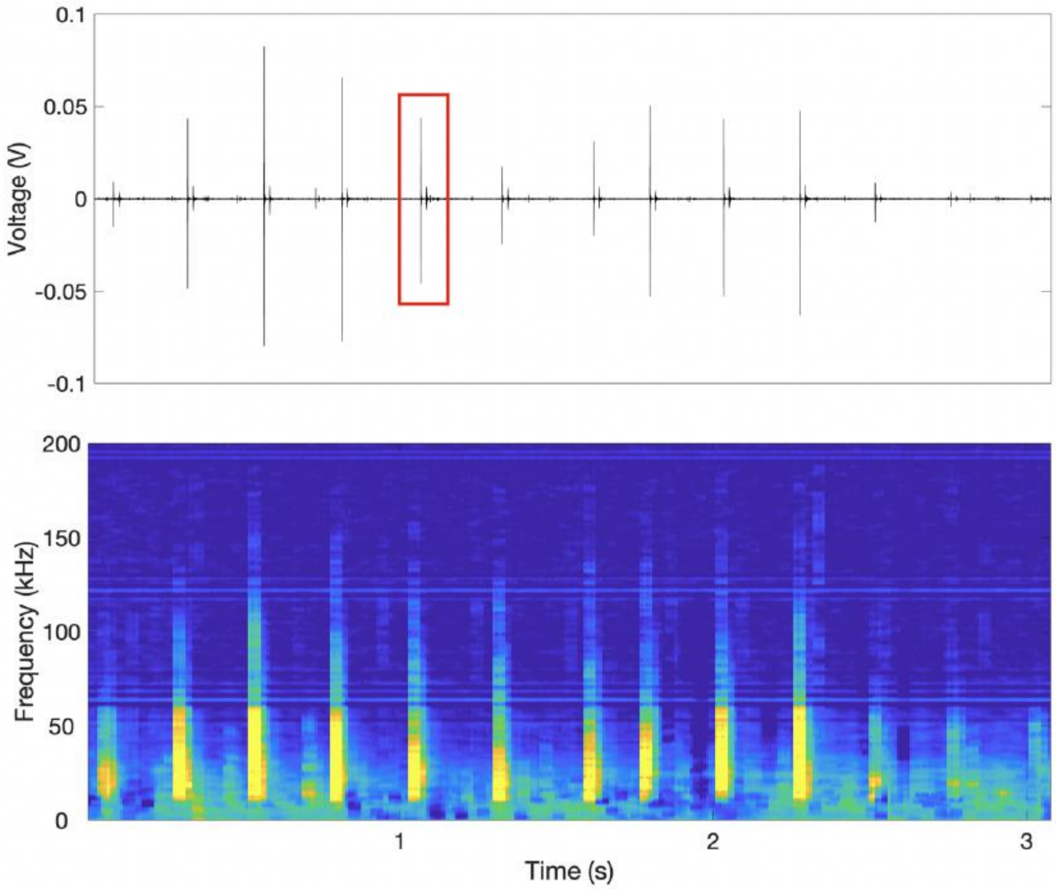

Figure 4.4: Example SRKW slow-click train in the time domain (top) and as a spectrogram (bottom) after noise removal. The red box indicates the two clicks (primary and secondary) magnified in Figure 4.5. Time and location of recording: 27 August 2020, 12:43:01 UTC, Swiftsure Bank.

the end of signal are likely reflected energy (Pers. Com. H. Yurk). All duration values reported in this study have been extracted visually.

The PP pressure value of the signal was extracted and used to derive RL. As an example, consider Figure 4.9, which shows a click that has been adjusted by the instrument sensitivity in the frequency domain, and returned to the time domain. The positive peak value is $1.86 \times 10^6$ $\mu$Pa and the negative peak value is $-1.44 \times 10^6$ $\mu$Pa leading to a PP value of $3.3 \times 10^6$ $\mu$Pa. An addition of 38 dB is required to adjust the amplification settings of the measurement system as the calibration data were amplified by a different value than the recorded RKW data were. Converting to a logarithmic scale leads to PP SL as follows: RL $= 20\log(3.3 \times 10^6\ \mu\text{Pa}/1\ \mu\text{Pa})$ dB $+$ 38 dB $=$ 168 dB re 1 $\mu$Pa. Note that the application of the calibration converted

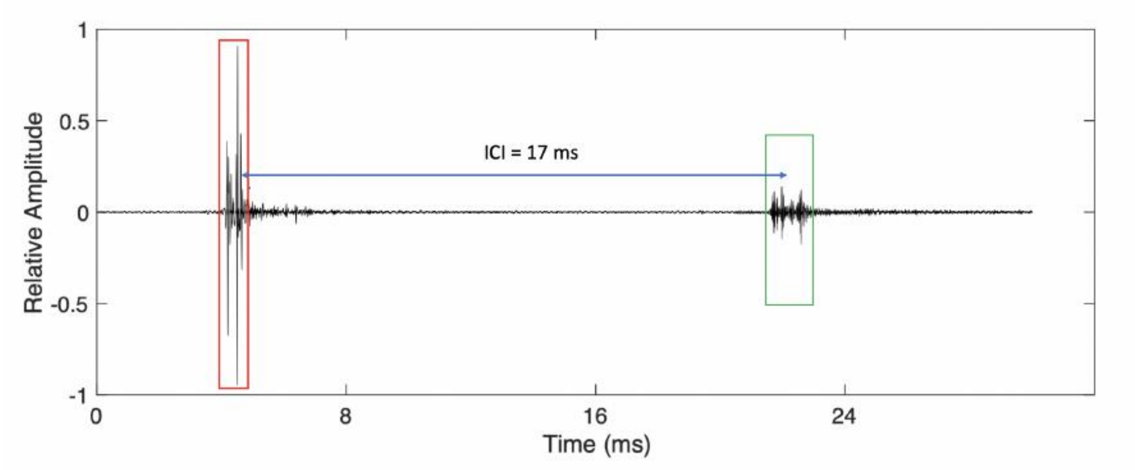

Figure 4.5: Magnification of the primary and secondary clicks illustrated in Figure 4.4. The red box shows the primary click that produces the spectra in Figure 4.6(a) and the green box shows the secondary click that produces the spectra in Figure 4.6(b). The time between the clicks is 17 ms.

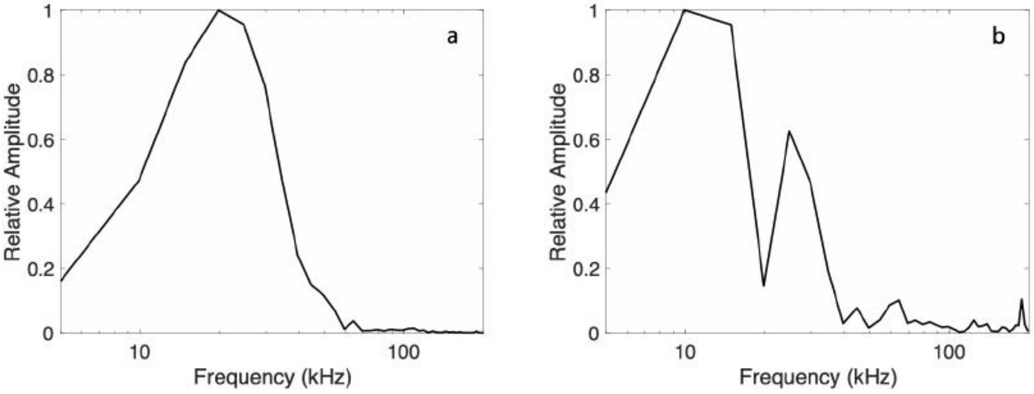

Figure 4.6: Spectra for the primary click (a) and the secondary click (b), indicated in Figure 4.5 by red and green boxes, respectively. The frequency bands are similar between clicks.

the resulting units from sensitivity (dB re V/$\mu$Pa) to true sound level (dB re 1 $\mu$Pa).

ASL was derived from the RL value by determining energy losses due to PL. As discussed in Chapter 2, PL is calculated by summing the geometric spreading and chemical absorption losses. While chemical absorption is frequency dependant, at relatively short ranges it can be approximated by a single value corresponding to the frequency at which click energy is centered. For RKWs, this value is taken

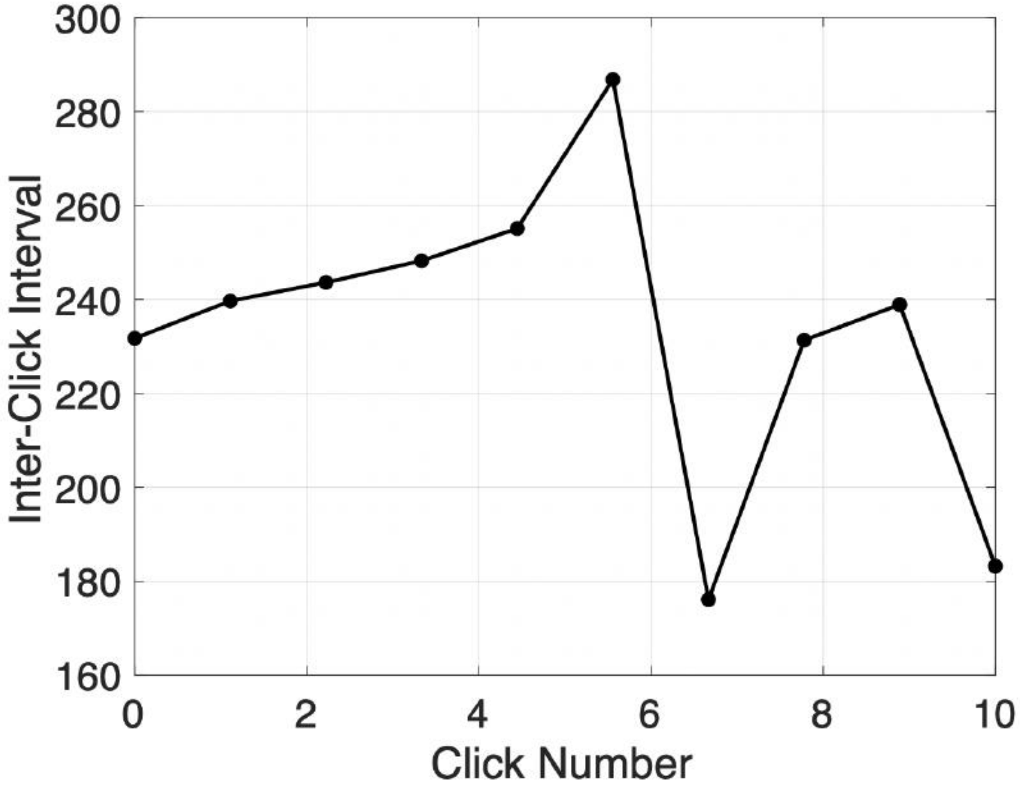

Figure 4.7: SRKW click train ICI as a function of click number, for the slow-click train shown in Figure 4.4

.

to be 30 kHz (a common mean centroid frequency value of an echolocation click) corresponding to PL = 0.01 $R$ dB (Eq. (2.2)). This approximation is particularly valid for short source to receiver distances, like the RKW to hydrophone distances in this study, as spherical spreading dominates PL significantly, while frequency dependant absorption contributes only slightly. For example, for the maximum distance used in this study (80 m), a signal at 30 kHz experiences a 0.8 dB loss, while a signal at 50 kHz experiences a 1.2 dB loss – a difference of just 0.4 dB. For the click in this example, with a range of 46±7 m, the total PL was determined to be 33±2 dB. Thus, the corresponding ASL, which represents the sound level at 1 m from the source, was determined to be ASL = 168 dB re 1 $\mu$Pa + 33±2 dB = 201±2 dB (pp) re 1 $\mu$Pa at 1 m.

Figure 4.10 presents a block diagram of the steps required to extract a source level value from an echolocation click.

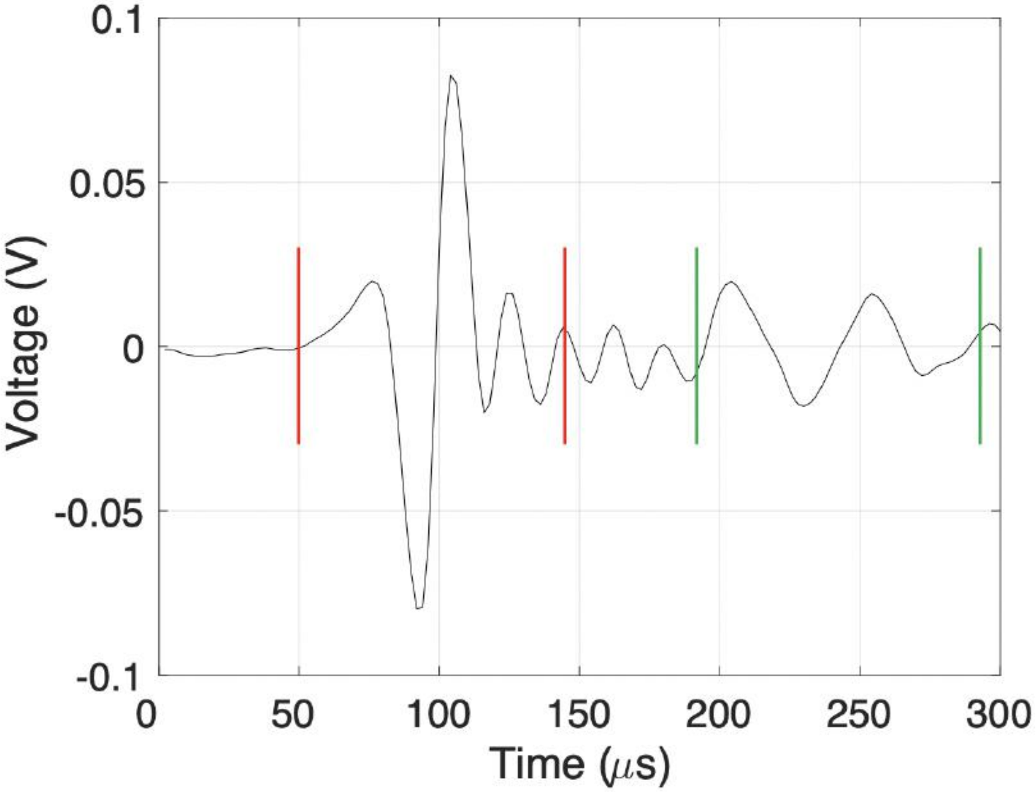

Figure 4.8: The largest click extracted from the click train in Figure 4.4. Red lines show the estimated beginning and end of the signal. Green lines show reflected energy not considered part of the direct arrival. Click duration for this example is 90 $\mu$s.

### 4.2.2 Echolocation Click Spectral Characteristics

To evaluate the frequency-domain spectral characteristics, each click within the click train was fast Fourier transformed (FFT). This was carried out by automating a search for clicks within a click train, setting the duration of the rectangular window to 100 $\mu$s before and 200 $\mu$s after the click's greatest amplitude (ensuring the click energy was captured), and extracting them for individual transformations. A spectrum was generated for each click with a frequency resolution of 3.3 kHz, based on 150 sample points at a 500 kHz sampling rate. Application of the calibration curve, applied through interpolation over the frequency range of the spectrum (2-200 kHz), led to an RL power spectrum, which was subsequently converted to an ASL power spectrum by accounting for PL.

Considering spectral characteristics, peak frequency is simply the frequency with

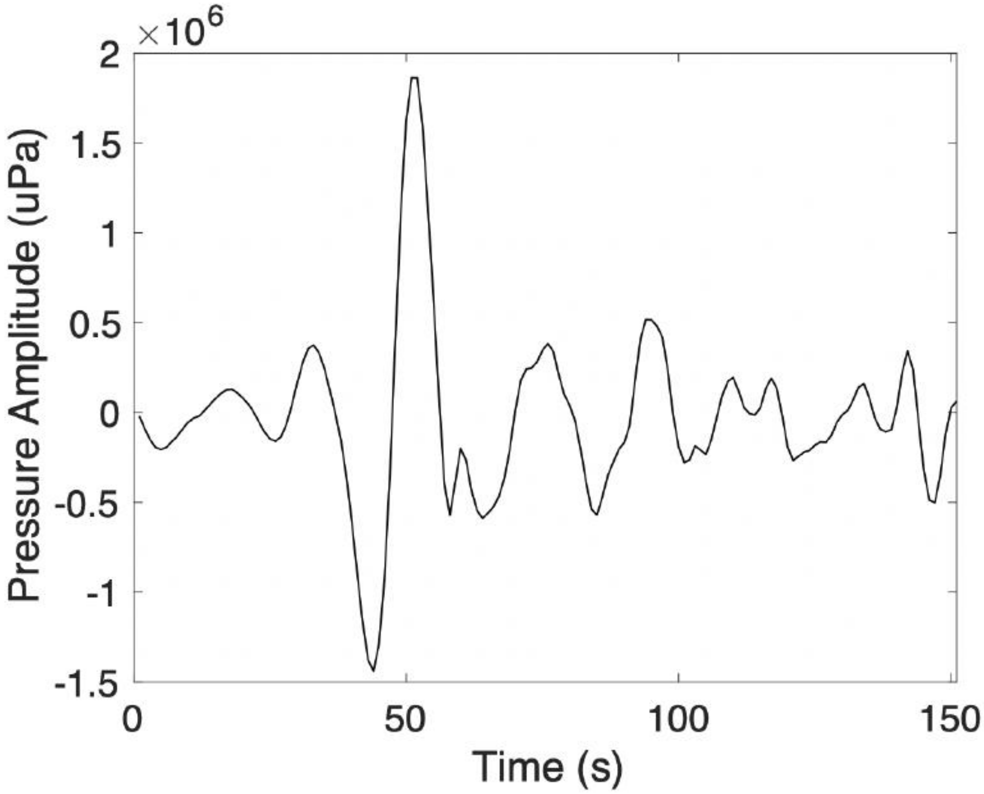

Figure 4.9: A click recorded on a Reson hydrophone showing its amplitude in pressure as a function of time.

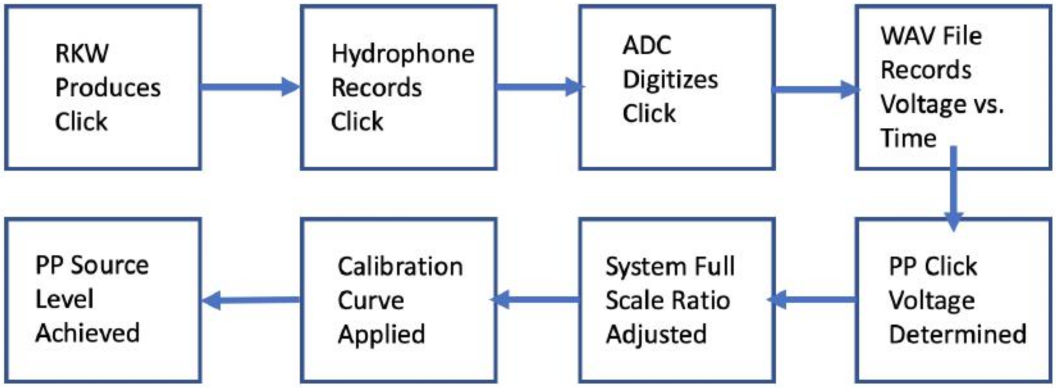

Figure 4.10: A block diagram showing the steps involved in extracting source level from an echolocation click.

the maximum power. However, for asymmetric or multi-modal spectra, the centroid frequency can be a more stable estimate of a representative central frequency [10]. Centroid frequency is defined as the frequency separating the spectrum into equal halves (on a linear frequency scale) and is calculated by summing the cumulative amplitude of the spectrum across the frequency range, and determining the frequency value that divides the cumulative amplitude in halves. RMS bandwidth is defined as the standard deviation of a linear spectrum around centroid frequency. RMS bandwidth is a better representation than −3 dB or −10 dB bandwidths as it can account for more than one prominent peak frequency [9]. Finally, the peak frequency value for a HFSP, when present in the spectrum, was visually extracted and a power level determined by comparison to the primary-peak amplitude.

Figure 4.11 shows the power spectrum of the click in Figure 4.8, corrected for hydrophone calibration and PL and plotted both linearly and logarithmically (both formats are commonly used). The peak frequency and centroid frequency (red line) are determined to be 20 and 30 kHz, respectively, and the RMS bandwidth (blue line) was 29 kHz. The HFSP (green line) was peaked at 87 kHz and had a power of −17 dB relative to the primary peak.

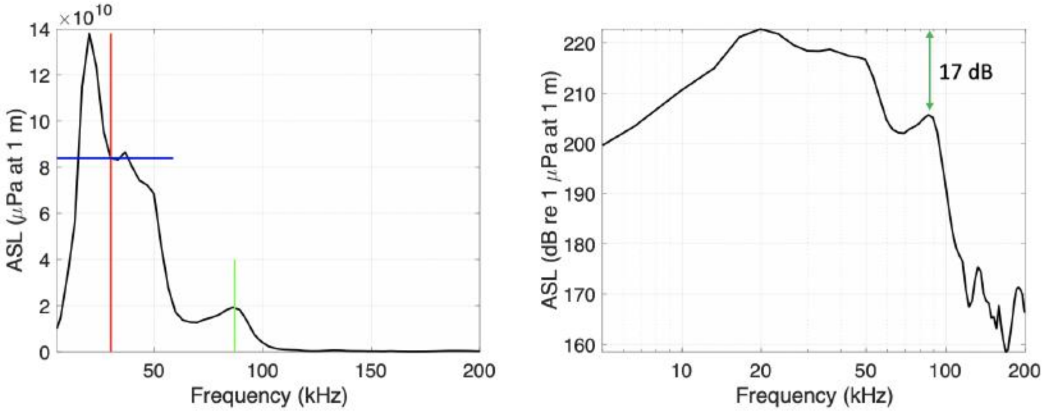

Figure 4.11: The linear amplitude (pressure) and logarithmic power (dB) spectra of the click in Figure 4.8 corrected for instrument response and PL. The red, blue, and green lines indicate the centroid frequency, RMS bandwidth, and HFSP, respectively.

Table 4.1 summarizes the acoustic characteristics extracted from the slow-click train and its largest click, shown in Figure 4.4. These characteristics were extracted from a Geospectrum hydrophone, which is valid for this example as saturation did not occur. The following sections present the results of the same analysis carried out on every echolocation click train that met the click-selection criteria from the data collected over both field seasons.

Table 4.1: Acoustic characteristics of the SRKW slow-click train shown in Figure 4.4.

| Click Train Characteristics | | Largest Click Characteristics | |
|---|---|---|---|
| Number of Clicks | 11 | Duration ($\mu$s) | 90 |
| Click Type | Slow | RL$_{pp}$ (dB re 1 $\mu$Pa) | 165±2 |
| Mean Peak Frequency (kHz) | 18±3 | ASL$_{pp}$ (dB re 1 $\mu$Pa at 1 m) | 201±2 |
| Mean Centroid Frequency (kHz) | 25±4 | HFSP (kHz) | 79 |
| Mean RMS Bandwidth (kHz) | 41±13 | HFSP Power Rel. Peak (dB) | −17 |

## 4.3 SRKW Echolocation Click Acoustic Characteristics

SRKW echolocation click data were recorded on a total of 13 days over both field seasons; however, only 5 days of recordings contained data that met click-selection criteria given in Section 4.1. A total of 708 echolocation clicks within 19 click trains met these criteria and were used in further analysis. Fifteen of the click trains were classified as slow-click trains, containing 340 clicks. Four of the click trains were classified as fast-click trains, containing 368 clicks. Unfortunately, no buzz-click trains were recorded for SRKWs during any of the encounters.

### 4.3.1 Slow-Click Trains

Following [4], an echolocation click train was categorized as a slow-click train if all ICIs of the train were greater than 100 ms; however, in this study, some cases included ICIs which fell within fast-click train criteria. Visual inspection of a click train was undertaken and an assessment made to whether the train should be considered slow or fast. Click trains for which the majority of ICIs were greater than 100 ms but which had a small number of ICIs less than 100 ms were deemed to be slow-click trains since they did not have a constant high click rate commonly used to define fast-click trains [11]. Figure 4.12 shows three representative clicks, from three different slow-click trains, and their spectra. The click spectra display similar characteristics: a prominent primary peak between 10-30 kHz, a secondary peak between

50-90 kHz, and little energy above 100 kHz. Almost all SRKW slow-clicks displayed characteristics similar to these.

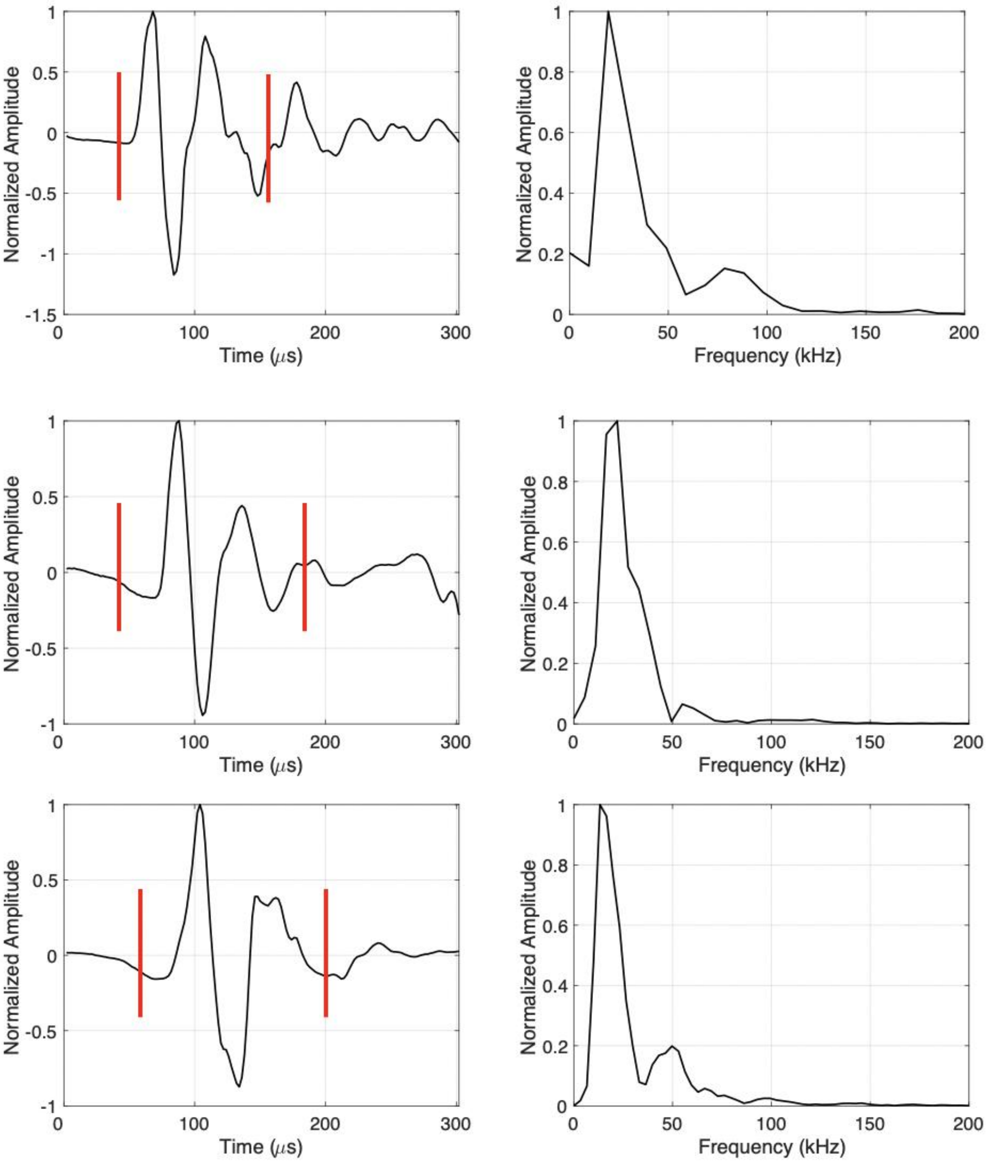

Figure 4.12: Three representative examples of SRKW echolocation slow-click waveforms and their spectra. The red lines show the beginning and end of the signal, identified manually to exclude reflections. The spectra corresponds to the full 300 $\mu$s waveform. Time and location of recordings, from top to bottom: 27 August 2020, 12:36:36 UTC, Swiftsure Bank; 26 August 2020, 14:34:40 UTC, Swiftsure Bank; 27 August 2020, 12:40:36 UTC, Swiftsure Bank.

Figure 4.13 shows histograms of acoustic characteristics for all 340 SRKW slow-clicks. The results are further discussed in Section 4.3.3 where they are compared to other click types. Figure 4.14 shows the PP ASLs of the largest click from each analyzed click train as a function of source to receiver range. Error bars were calculated by determining the PL at the estimated range plus the standard deviation, and the estimated range minus the standard deviation. As PL is logarithmic, error bars are not symmetric about the ASL estimate. The red line is a best fit regression curve based on spherical spreading, calculated as $A+20\log(2R)$ where $R$ is range and $A$ is an unknown constant (ASL at $R = 0$), calculated to minimize misfit. This plot suggests that SRKWs may increase the source level of their clicks based roughly on the spherical-spreading loss over the distance to an object in order to receive echoes of similar intensity. Similar plots were presented for NRKWs in [9], although that work did not discuss the interpretation in terms of source level adjustments, and considered $A+20\log(R)$ which does not account for the two-way propagation from the source to reflector and back (the difference can be taken up in the calculation of $A$). This hypothesis is only valid under the assumption that the echolocating RKW is directing the click specifically at the array, and not another target in its vicinity. While click selection criteria laid out in Section 4.1 increases the probability that the clicks are directed at the array, it is not certain, and thus, the hypothesis is difficult to validate.

### 4.3.2 SRKW Fast-Clicks

An echolocation click train was categorized as a fast-click train if the ICI values were between 10-100 ms [11]. Four fast-click trains were identified and met click-selection criteria for SRKWs in 2019 and 2020. Figure 4.15 shows a fast-click train of 44 clicks and its spectrogram. The majority of the energy is distributed between 10-60 kHz with little energy extending past 70 kHz for most clicks. Figure 4.16 shows three fast-click waveforms and their spectra from three separate click trains. The click waveforms differed greatly in structure between click trains, but tended to have similar spectra. Figure 4.17 shows histograms of SRKW fast-click acoustic characteristics. Figure 4.18 shows the PP ASLs of the largest clicks from each of the four analyzed click trains. The largest fast-click ASLs followed the same trend as the slow-click ASLs (increase in strength as range increases), although there are too few data to draw conclusions. These observations will be discussed in Section 4.3.3.

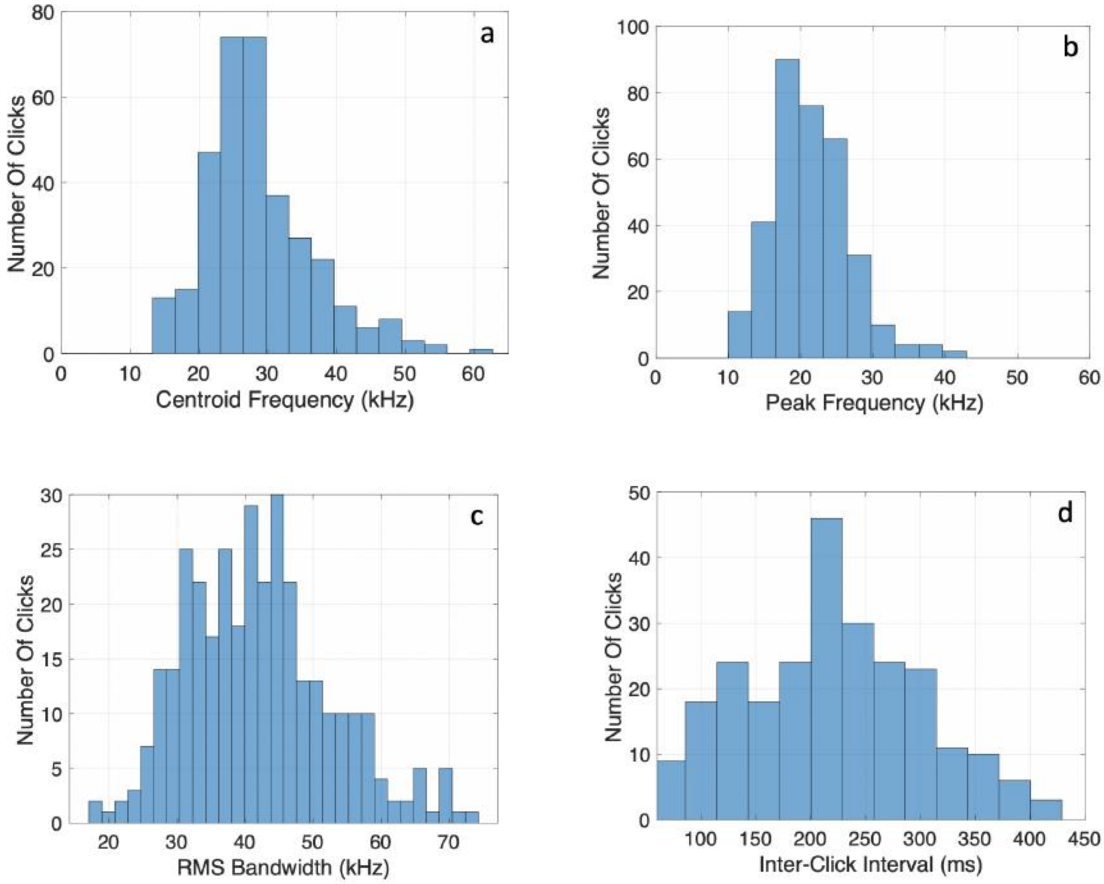

Figure 4.13: Histograms of SRKW slow-click acoustic characteristics. Data are from 340 clicks in 15 recorded slow-click trains.

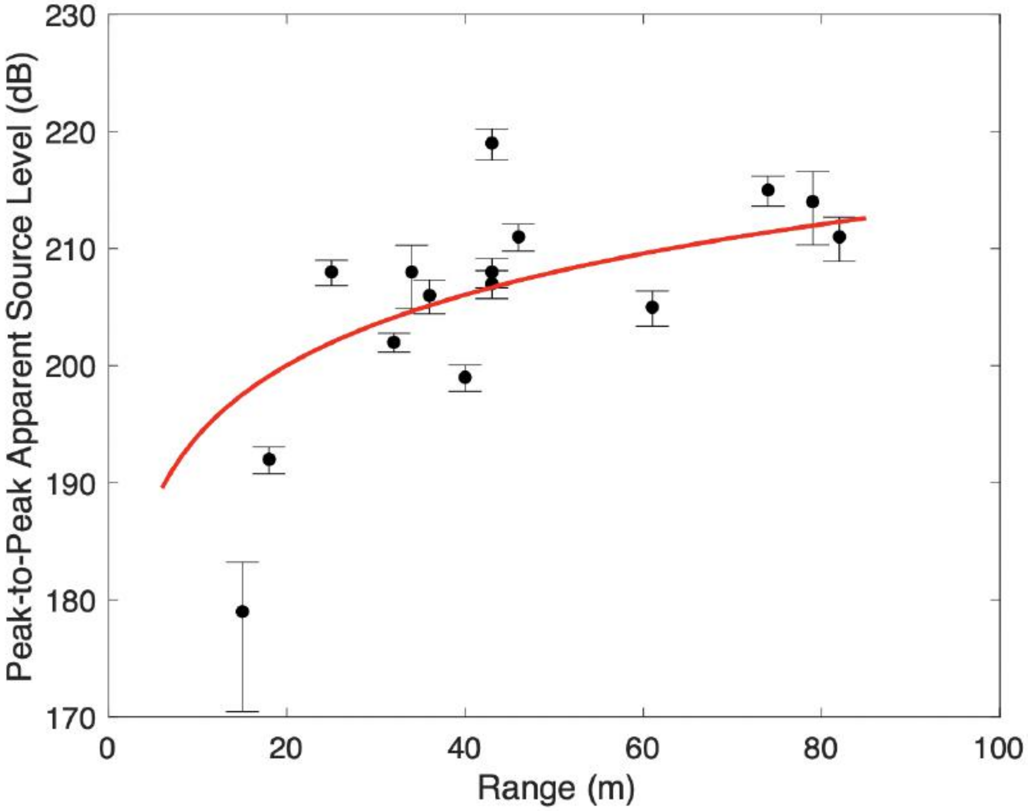

Figure 4.14: PP ASL for the largest click from each SRKW slow-click train as a function of range from the whale to the array. Error bars were determined from the PL calculated at the estimated range plus and minus the range standard deviation. The red line is a best-fit regression curve based on spherical spreading for a two-way path, as described in the text.

### 4.3.3 SRKW Click Type Comparison

Table 4.2 compares the results of the analysis on SRKW slow- and fast- echolocation clicks. ICI values for slow-clicks varied greatly, with an average value 207 ms and a standard deviation of 236 ms, resulting in a CoV of 1.14. Fast-clicks had an average ICI value of 72 ms with a standard deviation of 42 ms, resulting in a CoV of 0.58. This greater variability for slow-click trains could suggest SRKWs prefer a constant rate of echo return when using fast-clicks as opposed to a changing rate when using slow-click. The centroid frequency and peak frequency do not change significantly (relative to standard deviations) between click type. The mean RMS bandwidth increases by 10 kHz between slow-clicks and fast-clicks, but it is not clear if this

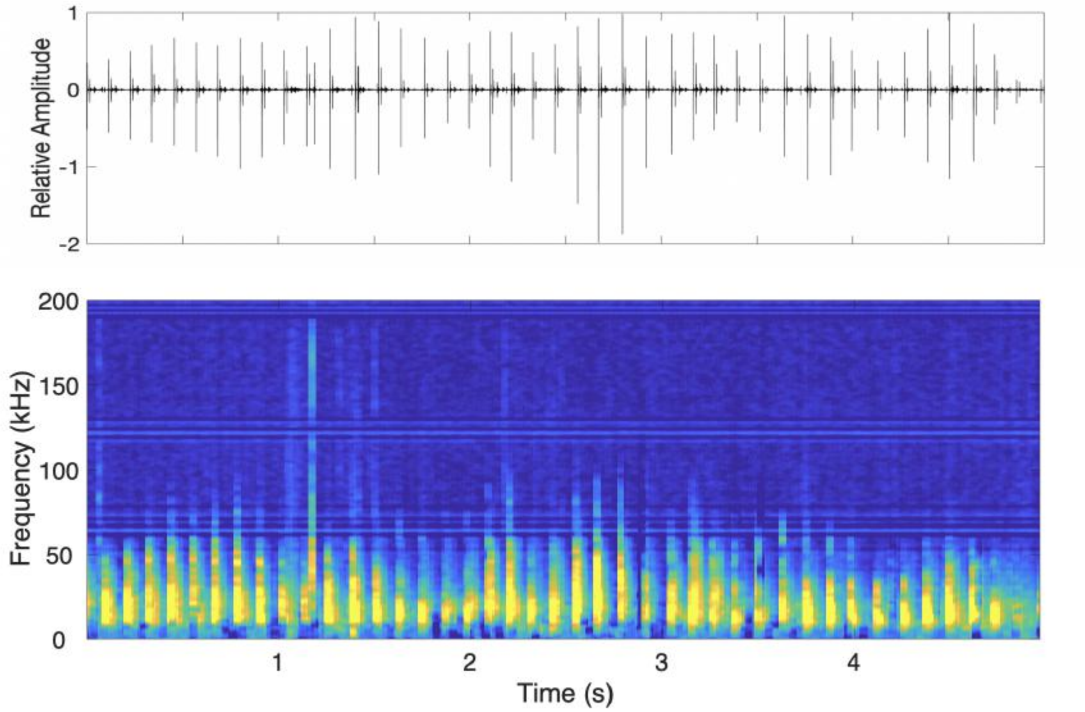

Figure 4.15: A SRKW fast-click train and its spectrogram. Time and location of recording: 26 August 2020, 14:08:07 UTC, Swiftsure Bank.

difference is significant given the associated uncertainties.

Table 4.2: SRKW echolocation click ICI and spectral characteristics. The values are means ± standard deviations with the 5th and 95th percentiles in parentheses, and $n$ = sample size.

| | Slow-Click ($n = 340$) | Fast-Click ($n = 368$) |
|---|---|---|
| ICI (ms) | 224±101 (67, 375) | 71±42 (10, 220) |
| Centroid Frequency (kHz) | 27±8 (17, 43) | 28±10 (17, 50) |
| Peak Frequency (kHz) | 20±7 (13, 30) | 21±7 (13, 33) |
| RMS Bandwidth (kHz) | 42±11 (27, 61) | 52±16 (29, 78) |

Table 4.3 compares the acoustic characteristics of the largest click from each of the slow-click ($n = 15$) and fast-click ($n = 4$) trains. The duration and power are presented as mean values with the lowest and highest observed values given in parentheses. Note that the duration was drawn from 100 clicks of each type in order to increase the sample size. The HFSP frequency is presented as a mean with lowest and highest observed values in brackets. The HFSP power level is presented in decibels below the

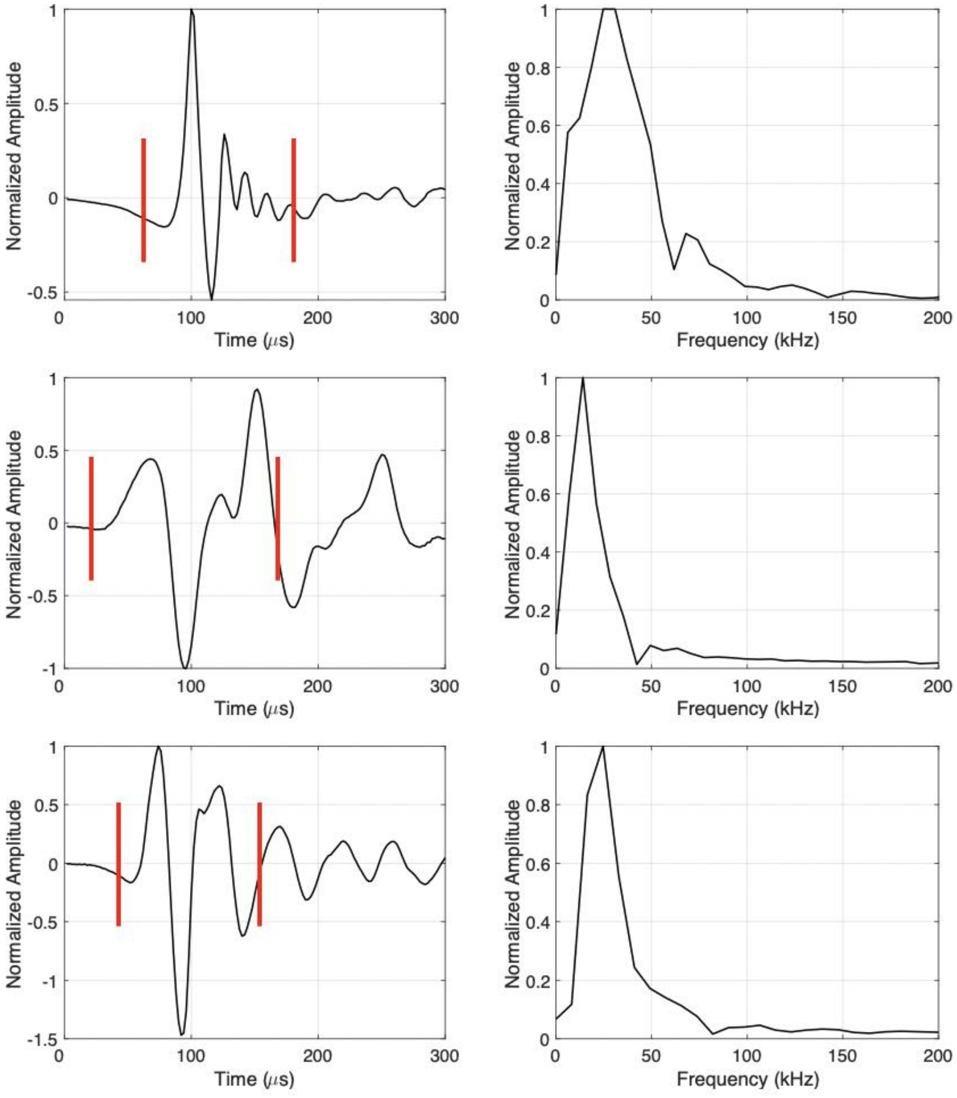

Figure 4.16: Three representative examples of SRKW echolocation fast-click waveforms and their spectra. The red lines show the beginning and end of the signal, extracted manually to exclude reflections. The spectra corresponds to the full 300 $\mu$s waveform. Time and location of recordings, from top to bottom: 25 August 2020, 13:11:32 UTC, Swiftsure Bank; 26 August 2020, 14:08:02 UTC, Swiftsure Bank; 27 August 2020, 12:01:58 UTC, Swiftsure Bank.

power of the peak frequency.

Duration, RL, and ASL values are similar between click types. While the frequency of the HFSP is similar for both click types, there is a noticeable difference in

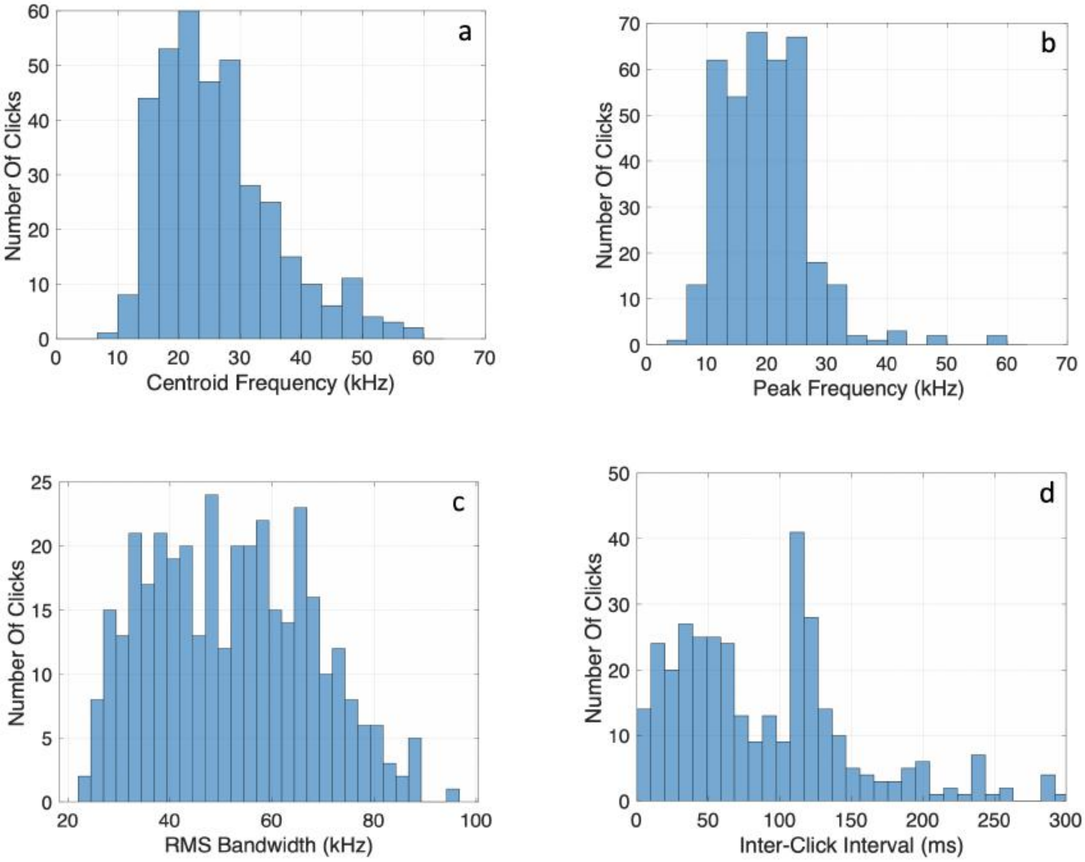

Figure 4.17: Histograms of SRKW fast-click acoustic characteristics. Data are from 368 clicks in 4 recorded fast-click trains.

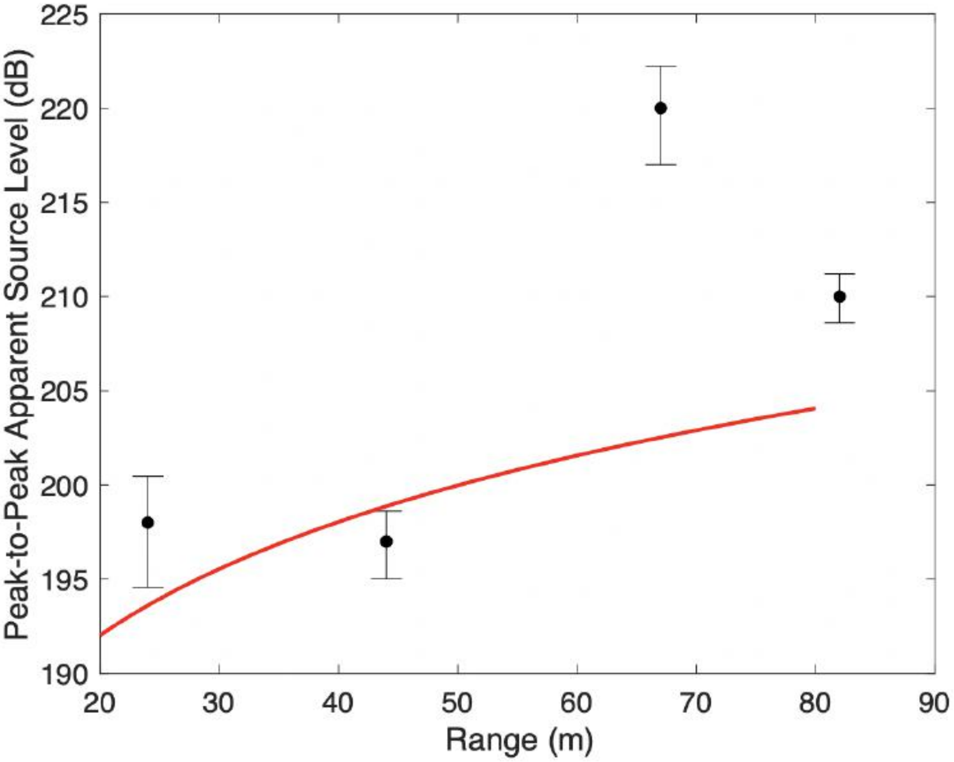

Figure 4.18: PP ASL for the largest click from each SRKW fast-click train as a function of range from the whale to the array. Error bars were determined from the PL calculated at the estimated range plus and minus the range standard deviation. The red line is a best-fit regression curve based on spherical spreading for a two-way path.

HFSP power levels. Most slow-clicks have a HFSP 12 dB below the primary peak frequency (approximately 75% less energy). Fast-click HFSPs tended to have even less power, at an average of 21 dB less than the primary peak (approximately 91% less power). This could suggest SRKWs utilize high frequency components less when fast-clicking than when slow-clicking.

Figures 4.19 and 4.20 present graphical representations of two click trains (slow and fast, respectively) and their characteristics (RL, ICI, centroid frequency, peak frequency). The centroid and peak frequencies in SRKW slow-click trains tended to remain constant, exhibiting only small changes from the mean. Fast-click train centroid frequency did the same; however, peak frequency was highly variable and often exhibited large, abrupt increases or decreases from one to click to the next. Both figures show examples of click trains with constant ICIs, but ICIs for several

Table 4.3: SRKW largest click characteristics. Values are means ± standard deviations with lowest and highest values in parentheses. The sample size for duration is 100 for each click type. HFSP power is presented as dB below the power at the peak frequency.

| | Slow-Click ($n = 15$) | Fast-Click ($n = 4$) |
|---|---|---|
| Duration ($\mu$s) ($n = 100$) | 110±24 (90, 150) | 110±16 (90, 140) |
| RL$_{pp}$ (dB re 1 $\mu$Pa) | 172±7 (158, 184) | 171±8 (163, 182) |
| ASL$_{pp}$ (dB re 1 $\mu$Pa at 1 m) | 206±10 (182, 218) | 206±11 (197, 220) |
| HFSP Frequency (kHz) | 86±12 (53, 89) | 89±3 (83, 89) |
| HFSP Power Rel. Peak (dB) | $-12 \pm 6$ | $-22 \pm 9$ |

other click trains (particularly slow-click trains) contained highly-variable values.

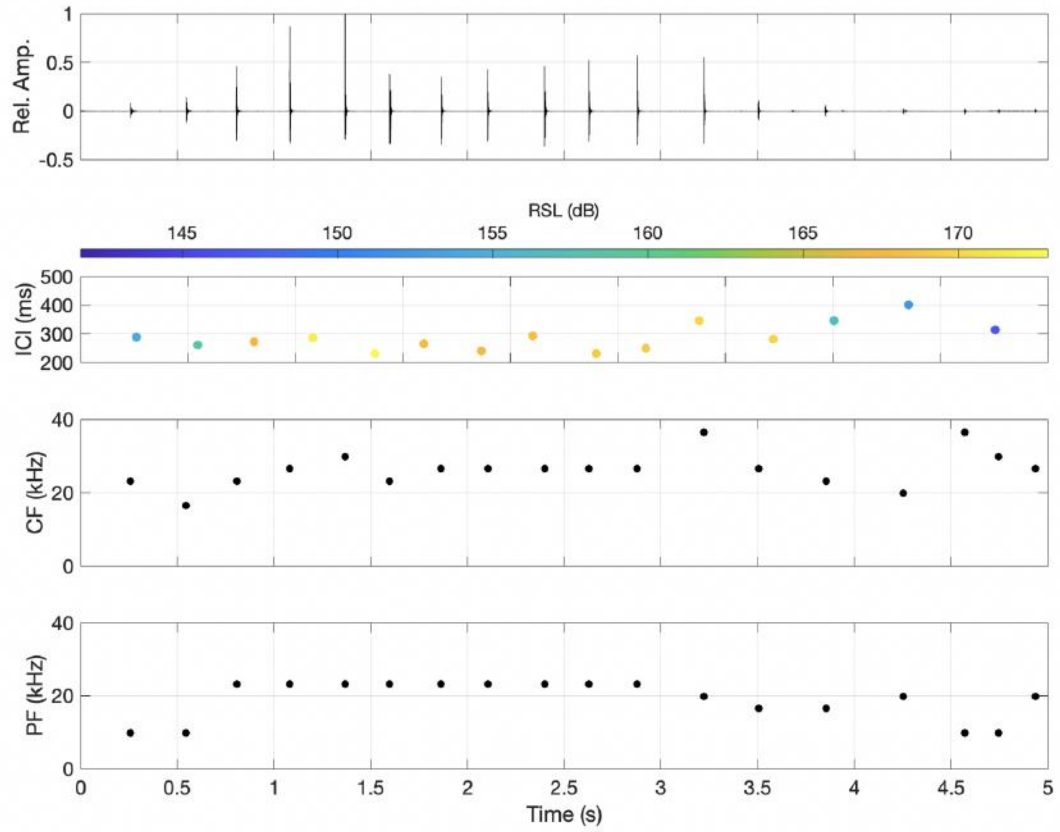

Figure 4.19: A graphical representation of a SRKW slow-click train and its characteristics.

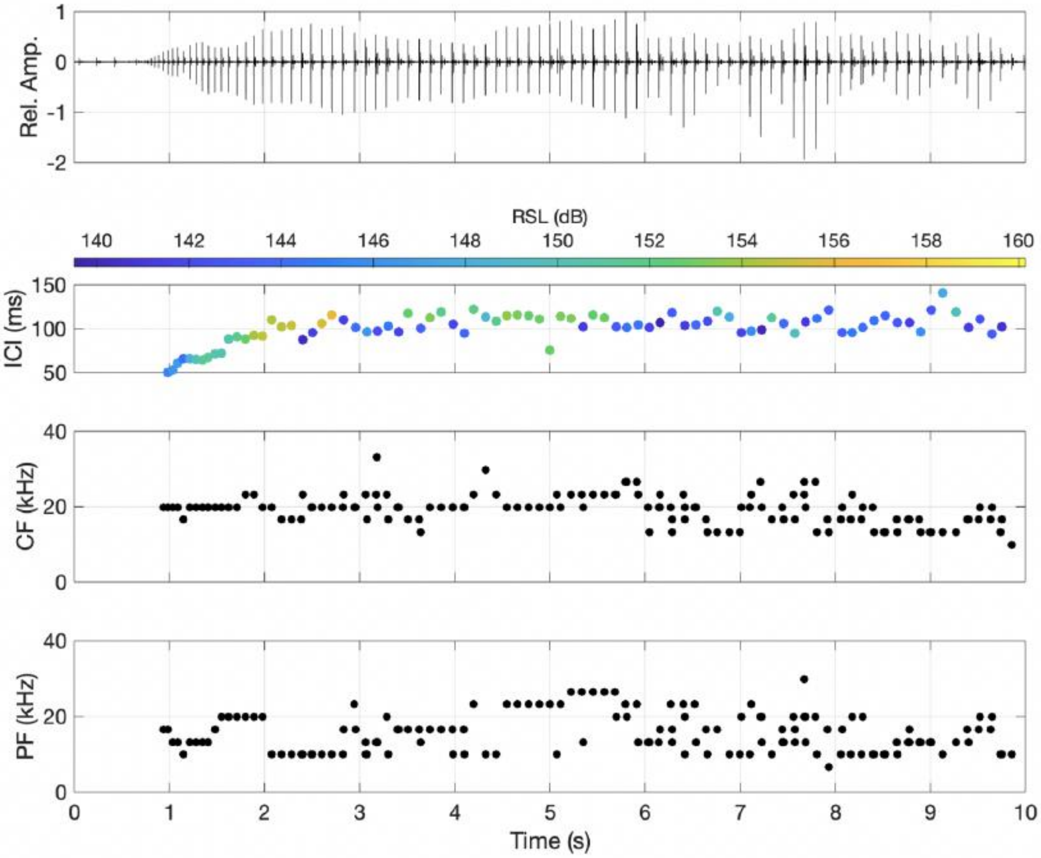

Figure 4.20: A graphical representation of a SRKW fast-click train and its characteristics.

## 4.4 NRKW Echolocation Click Acoustic Characteristics

NRKWs were encountered on six of the field days in 2019; however, only during two days were echolocation click data recorded that met click-selection criteria. A total of 1277 echolocation clicks within 16 click trains were selected for further analysis. Ten of the click trains were classified as slow-click trains, containing 564 clicks. Five of the click trains were classified as fast-click trains, containing 559 clicks. Fortunately, one buzz-click train was recorded, containing 154 clicks.

### 4.4.1 NRKW Slow-Clicks

Figure 4.21 shows a NRKW slow-click train and its spectrogram. Energy is concentrated between about 10-60 kHz for most clicks. The majority of clicks have little energy above 100 kHz.

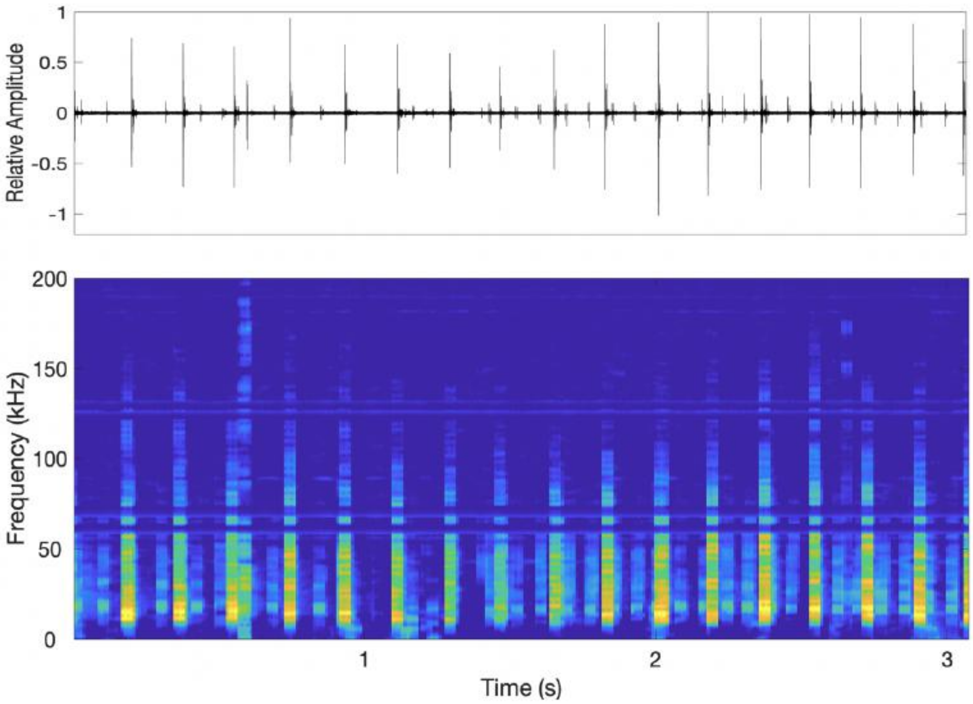

Figure 4.21: A NRKW slow-click train and its spectrogram. Time and location of recording: 13 August 2019, 17:23:27 UTC, Johnstone Strait.

Figure 4.22 shows three representative slow-click waveforms and spectra, from three separate click trains. The waveforms tend to vary in structure, but displayed broad frequency spectra between 10-60 kHz, and HFSPs centred between 70-95 kHz. Figure 4.23 shows histograms of click characteristics for the 564 NRKW slow-clicks that met click-selection criteria. The results are further discussed in Section 4.4.4. Figure 4.24 shows the PP ASLs of the largest slow-clicks from each click train as a function of range from the whale to the array. Like the SRKWs, these results suggest NRKWs might produce louder clicks the further they are from a target, roughly according to spherical-spreading loss.

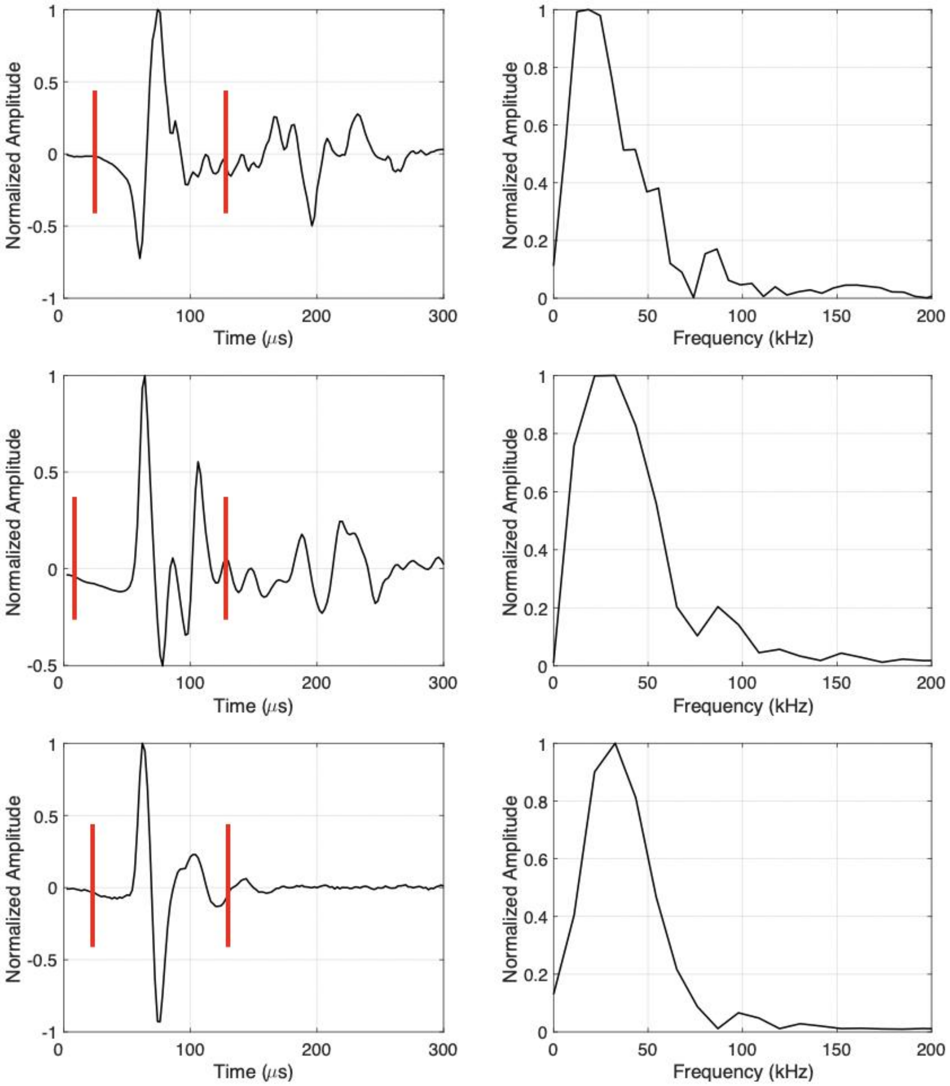

Figure 4.22: Three representative examples of NRKW echolocation slow-click waveforms and their spectra. The red lines show the beginning and end of the signal, extracted manually to exclude reflections. The spectra corresponds to the full 300 $\mu$s waveform. Time and location of recordings, from top to bottom: 13 August 2019, 17:25:27 UTC, Johnstone Strait; 13 August 2019, 17:24:22 UTC, Johnstone Strait; 18 August 2019, 18:33:31 UTC, Johnstone Strait.

### 4.4.2 NRKW Fast-Clicks

Four NRKW fast-click trains were identified and met click-selection criteria. Figure 4.25 shows a NRKW fast-click train and its spectrogram. Like the slow-click train,

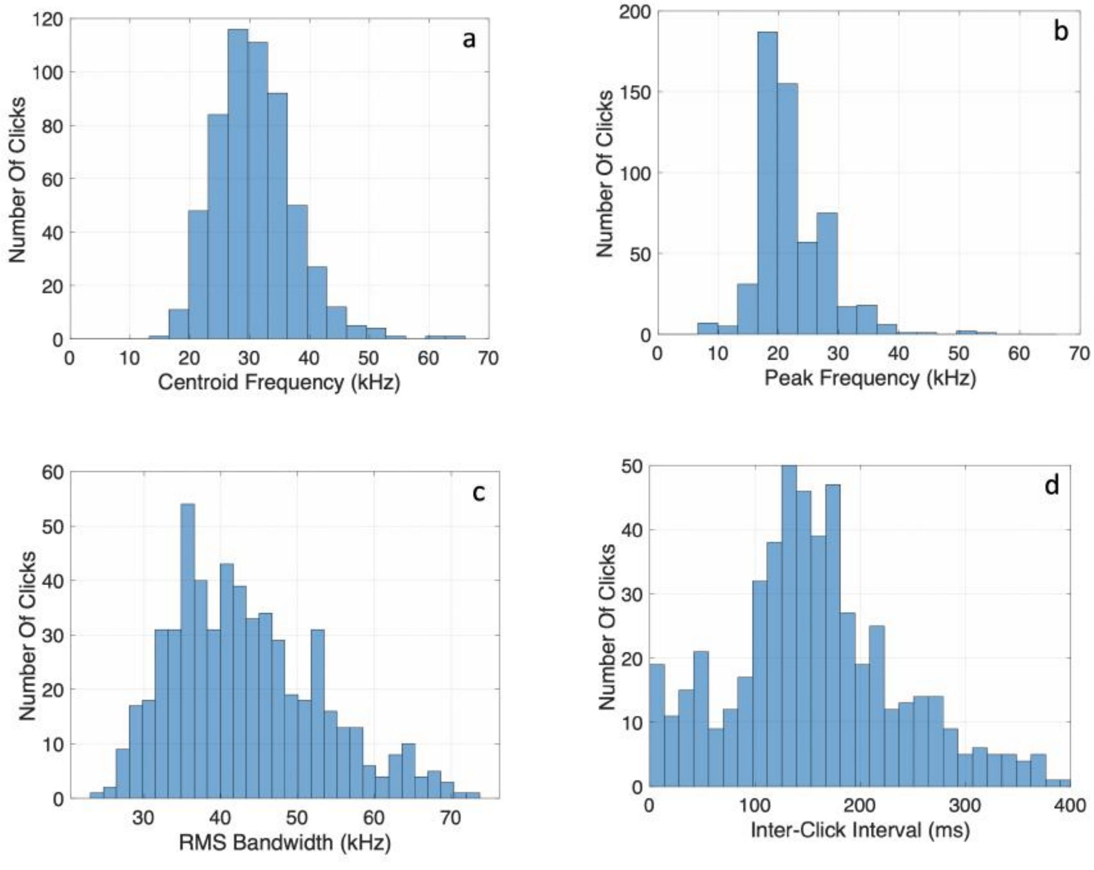

Figure 4.23: Histograms of NRKW slow-click acoustic characteristics. Data are from 564 clicks in 10 recorded slow-click trains.

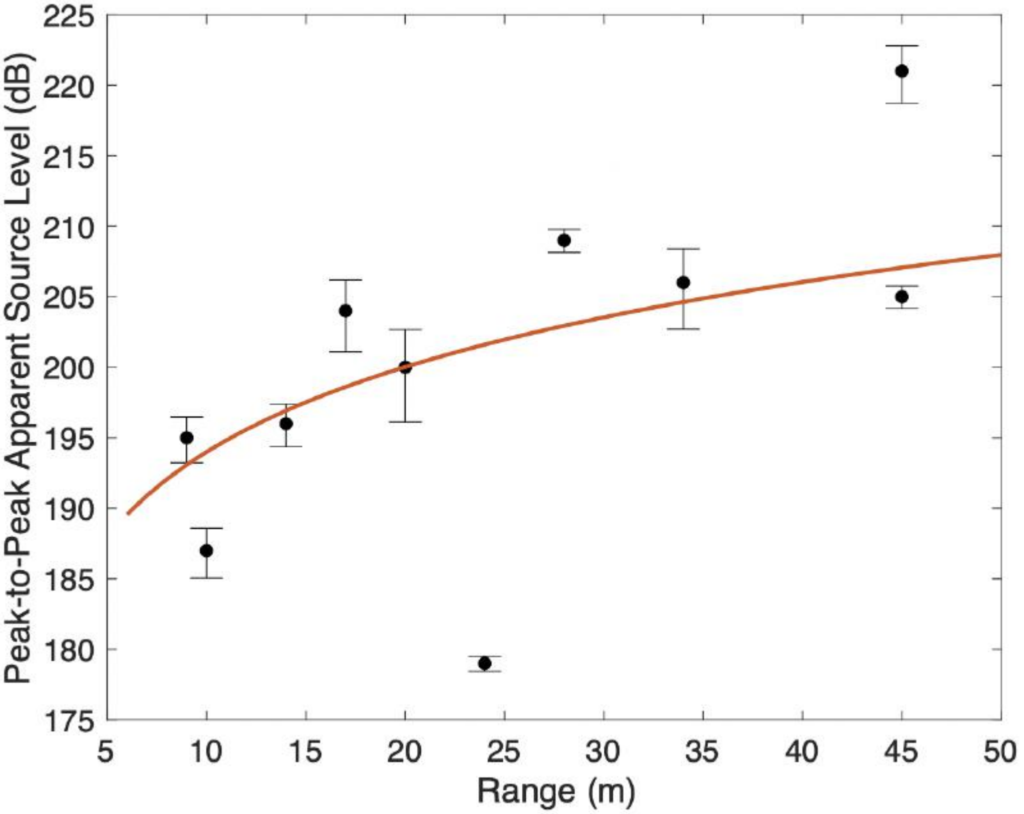

Figure 4.24: PP ASL for the largest click from each NRKW slow-click train as a function of range from the whale to the array. Error bars were determined from the PL calculated at the estimated range plus and minus the range standard deviation. The red line is a best-fit regression curve based on spherical spreading for a two-way path.

the energy is mostly localized between 10-60 kHz; however, some of the stronger clicks have energy in frequencies extending above 100 kHz.

Figure 4.26 shows three fast-click waveforms and their spectra from three different click trains. Duration values are similar to slow-clicks and also displayed broad frequency spectra between 10-60 kHz. HFSPs are clearly evident in the top and bottom spectral panels at 95 and 65 kHz, respectively, but not clear in the middle panel. Figure 4.27 shows histograms of NRKW fast-click acoustic characteristics. Figure 4.28 shows the five largest click ASLs as a function of range from the whale to the array. Although too few to be conclusive, the data follow the same trend as the slow-clicks: the source level increases as range increases, roughly consistent with counteracting spherical-spreading loss.

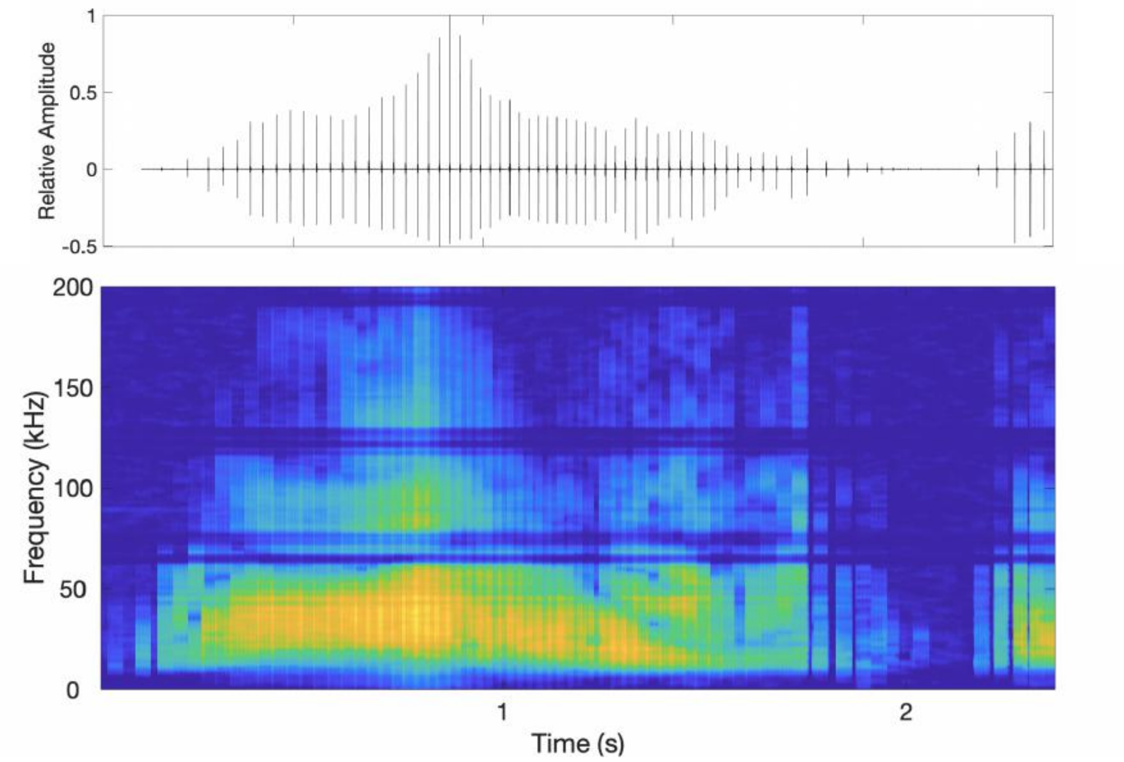

Figure 4.25: A NRKW fast-click train and its spectrogram. Time and location of recording: 18 August 2019, 13:19:10 UTC, Johnstone Strait.

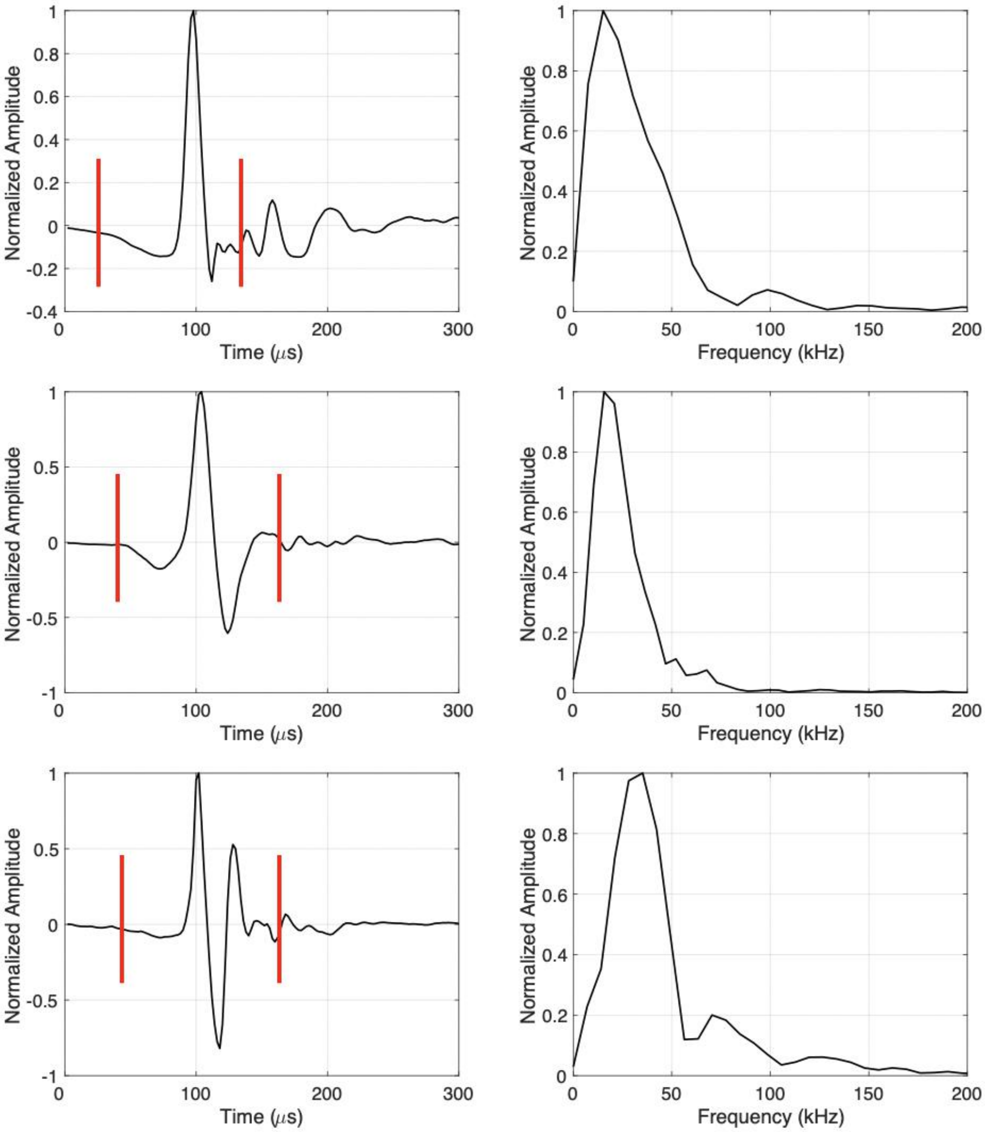

Figure 4.26: Three representative examples of NRKW echolocation fast-click waveforms and their spectra. The red lines show the beginning and end of the signal, extracted manually to exclude reflections. The spectra corresponds to the full 300 $\mu$s waveform. Time and location of recordings, from top to bottom: 13 August 2019, 17:23:37 UTC, Johnstone Strait; 13 August 2019, 17:27:22 UTC, Johnstone Strait; 18 August 2019, 13:19:10 UTC, Johnstone Strait.

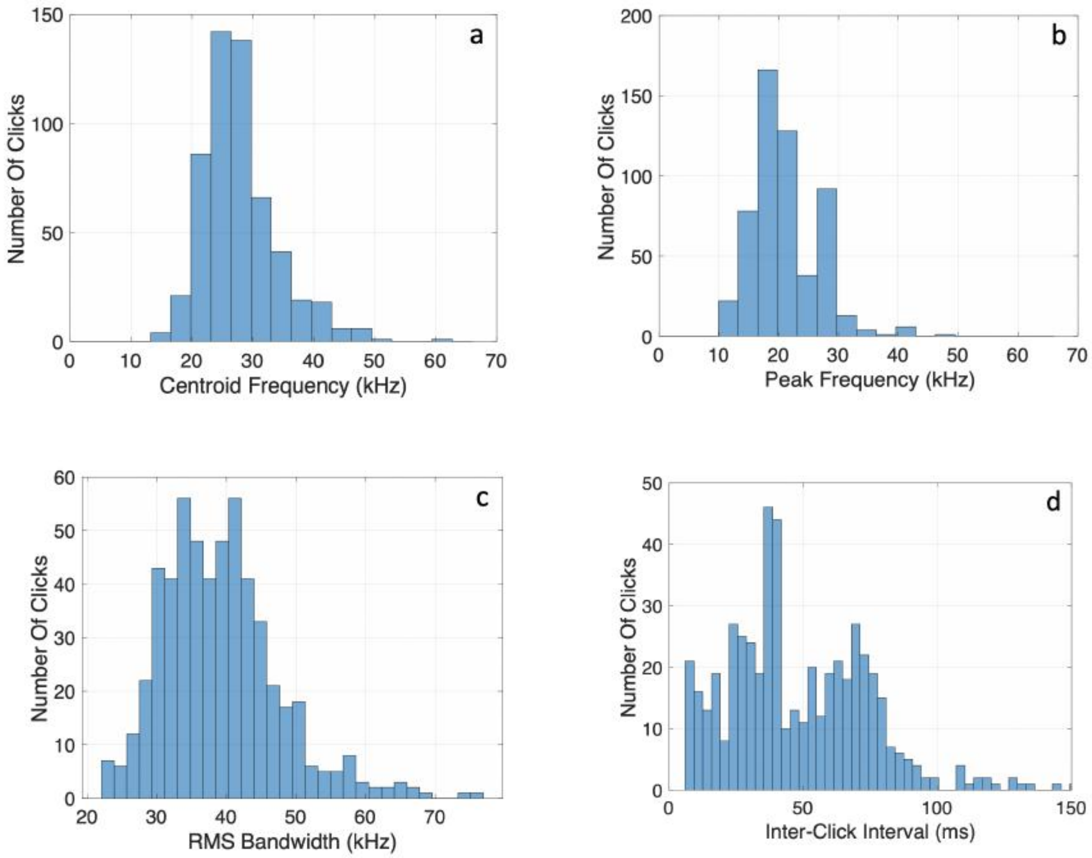

Figure 4.27: Histograms of NRKW fast-click acoustic characteristics. Data are from 559 clicks in 5 recorded fast-click trains.

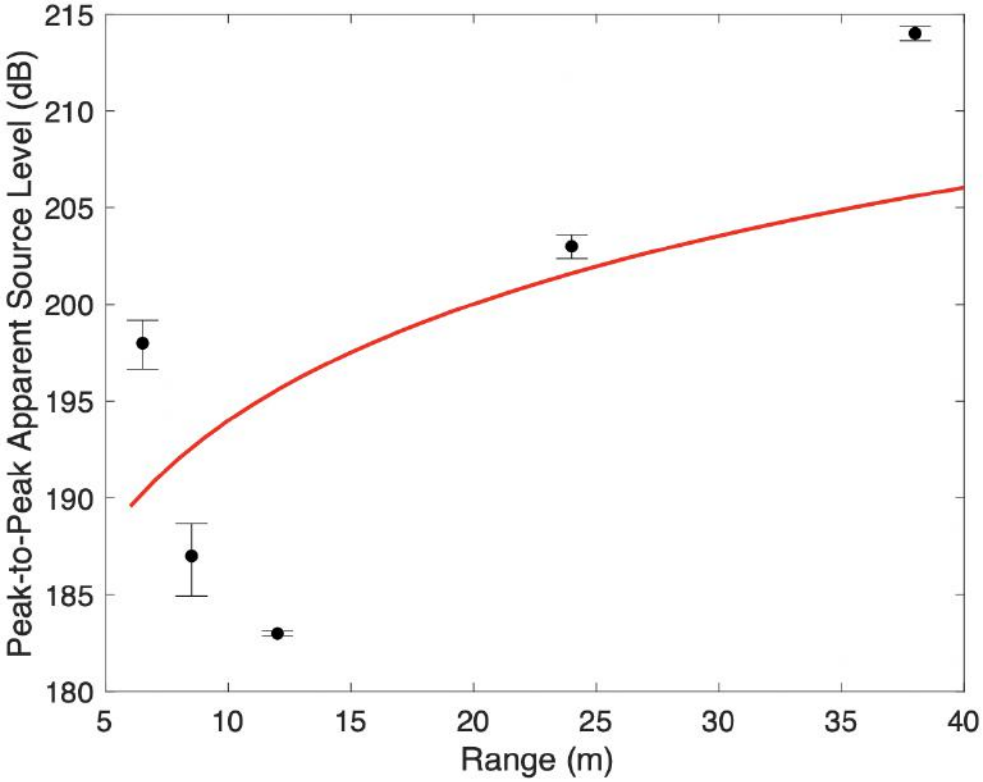

Figure 4.28: PP ASL for the largest click from each NRKW fast-click train as a function of range from the whale to the array. Error bars were determined from the PL calculated at the estimated range plus and minus the range standard deviation. The red line is a best-fit regression curve based on spherical spreading PL for a two-way path.

### 4.4.3 NRKW Buzz-Clicks

Figure 4.29 shows the one recorded NRKW buzz-click train and its associated spectrogram. The click train has the most energy between 10-60 kHz, with decreasing energy up to approximately 100 kHz for the stronger clicks. The three clicks with high-frequency components up to 200 kHz were likely produced by Pacific white-sided dolphins, which produce much higher-frequency clicks, and were observed visually to be in the immediate vicinity, and therefore were not considered during click analysis. Figure 4.30 shows three buzz-click waveforms from the same click train, and their spectra. Click duration was noticeably longer for buzz-clicks than for slow- or fast-clicks. A HFSP was present in all of the buzz-clicks but had a variable frequency between 40-90 kHz. Figure 4.31 shows histograms of NRKW buzz-click acoustic characteristics extracted from the one recorded buzz-click train.

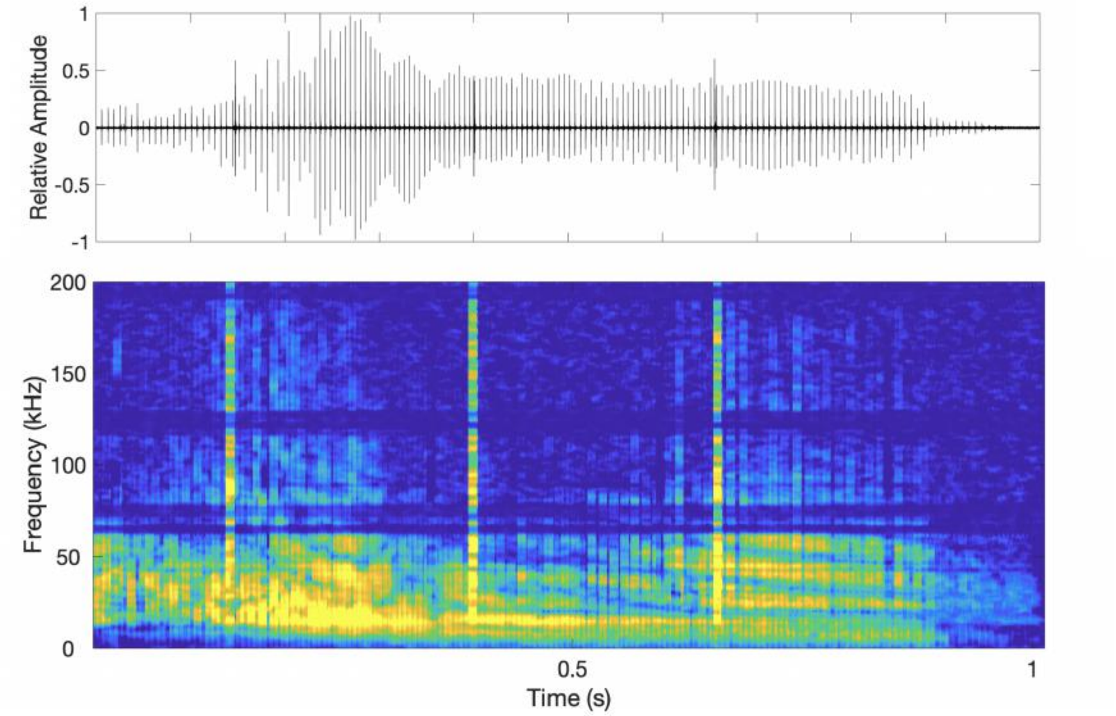

Figure 4.29: A NRKW buzz-click train and its spectrogram. The three clicks with very high frequency components were produced by Pacific white-sided dolphins. Time and location of recording: 18 August 2019, 13:18:50 UTC, Johnstone Strait.

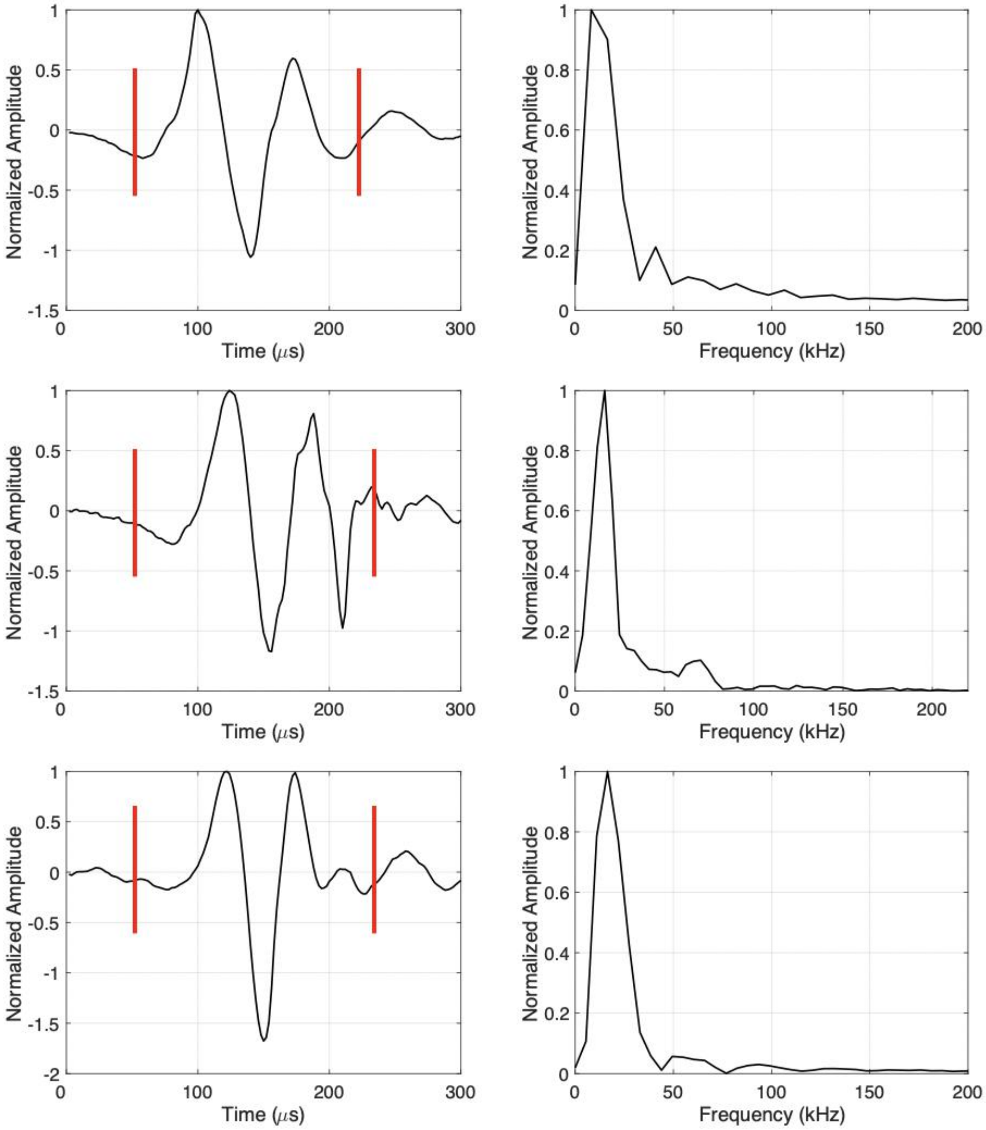

Figure 4.30: Three representative examples of NRKW echolocation buzz-click waveforms and their spectra. The red lines show the beginning and end of the signal, extracted manually to exclude reflections. The spectra corresponds to the full 300 $\mu$s waveform. The three clicks were extracted from the same buzz-click train. Time and location of recording: 18 August 2019, 13:18:50 UTC, Johnstone Strait.

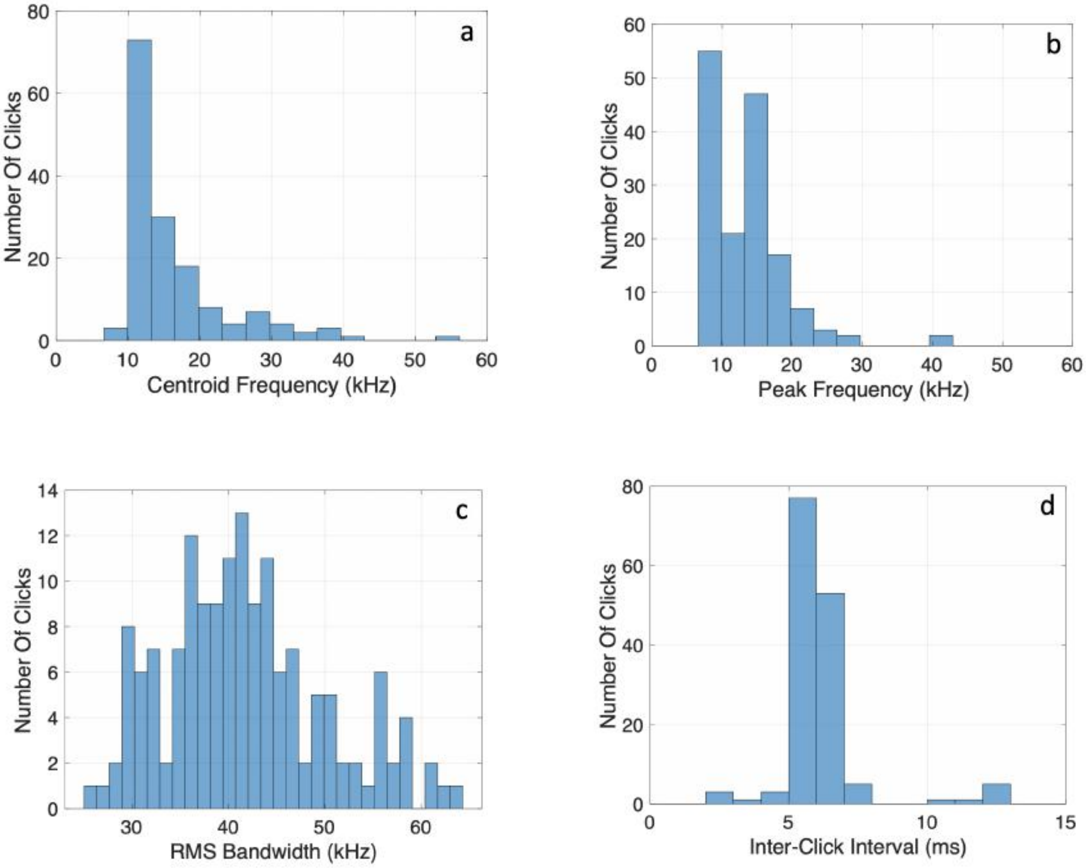

Figure 4.31: Histograms of NRKW buzz-click acoustic characteristics. Data are from 154 clicks in 1 recorded buzz-click train.

### 4.4.4 NRKW Click Type Comparison

Table 4.4 presents the acoustic characteristics of NRKW echolocation clicks that met click-selection criteria. The slow- and fast-clicks do not show significant differences in peak or centroid frequency, suggesting that NRKWs do not alter their click characteristics significantly when switching from one click type to the other. The one buzz-click train, however, had significantly reduced values for both centroid and peak frequency, by approximately 12 and 8 kHz, respectively. The RMS bandwidths did not change significantly between any click type.

Table 4.4: NRKW echolocation click ICI and spectral characteristics. The values are means ± standard deviations with the 5th and 95th percentiles in parentheses, and $n$ = sample size.

| | Slow-Click ($n$ = 564) | Fast-Click ($n$ = 549) | Buzz-Click ($n$ = 99) |
|---|---|---|---|
| ICI (ms) | 160±86 (23, 327) | 56±48 (11, 143) | 6±2 (5, 7) |
| Centroid Frequency (kHz) | 29±7 (20, 40) | 26±6 (20, 40) | 15±7 (10, 30) |
| Peak Frequency (kHz) | 21±7 (13, 33) | 19±6 (13, 26) | 12±7 (7, 20) |
| RMS Bandwidth (kHz) | 43±10 (30, 63) | 39±8 (28, 56) | 42±8 (29, 58) |

Table 4.5 compares the acoustic characteristics of the largest click from each NRKW click train. Slow- and fast-click durations did not differ significantly; however, buzz-click duration was approximately 30 ms longer, on average. These results are in agreement with [10] which showed that buzz-clicks produced by white-beaked dolphins were also longer in duration than their slow-clicks. ASL values of the largest click from each click train did not differ greatly between click type. HFSP frequency and power were similar for slow- and fast-clicks. The buzz-click HFSP frequency was significantly lower than the lowest HFSP values for slow- or fast-clicks; however, the sample size (of one) is too small for meaningful comparison.

Figures 4.32, 4.33, and 4.34 present graphical representations of three click trains (slow, fast, and buzz, respectively) and their characteristics (RL, ICI, centroid frequency, peak frequency). The slow-click train displayed only small variability in ICI, and centroid and peak frequencies, with the exception of one outlier. The fast-click train contained particularly constant ICI and frequency values. The buzz-click train displayed low variability in ICI and frequency values.

Table 4.5: NRKW largest click characteristics. Values are means ± standard deviations with lowest and highest values in parentheses. The sample size for duration is 100 for each click type. HFSP power is presented as dB less than the power at the peak frequency.

| | Slow-Click ($n = 10$) | Fast-Click ($n = 5$) | Buzz-Click ($n = 1$) |
|---|---|---|---|
| Duration ($\mu$s) ($n = 100$) | 112±15 (90, 160) | 116±19 (90, 160) | 146±17 (100, 160) |
| $\text{RL}_{pp}$ (dB re 1 $\mu$Pa) | 173±9 (151, 187) | 169±9 (161, 181) | 158 |
| $\text{ASL}_{pp}$ (dB re 1 $\mu$Pa at 1 m) | 200±12 (179, 221) | 197±12 (183, 214) | 192 |
| HFSP Frequency (kHz) | 86±6 (76, 92) | 87±5 (79, 89) | 59 |
| HFSP Power Rel. Peak (dB) | $-11 \pm 4$ | $-14 \pm 10$ | $-15$ |

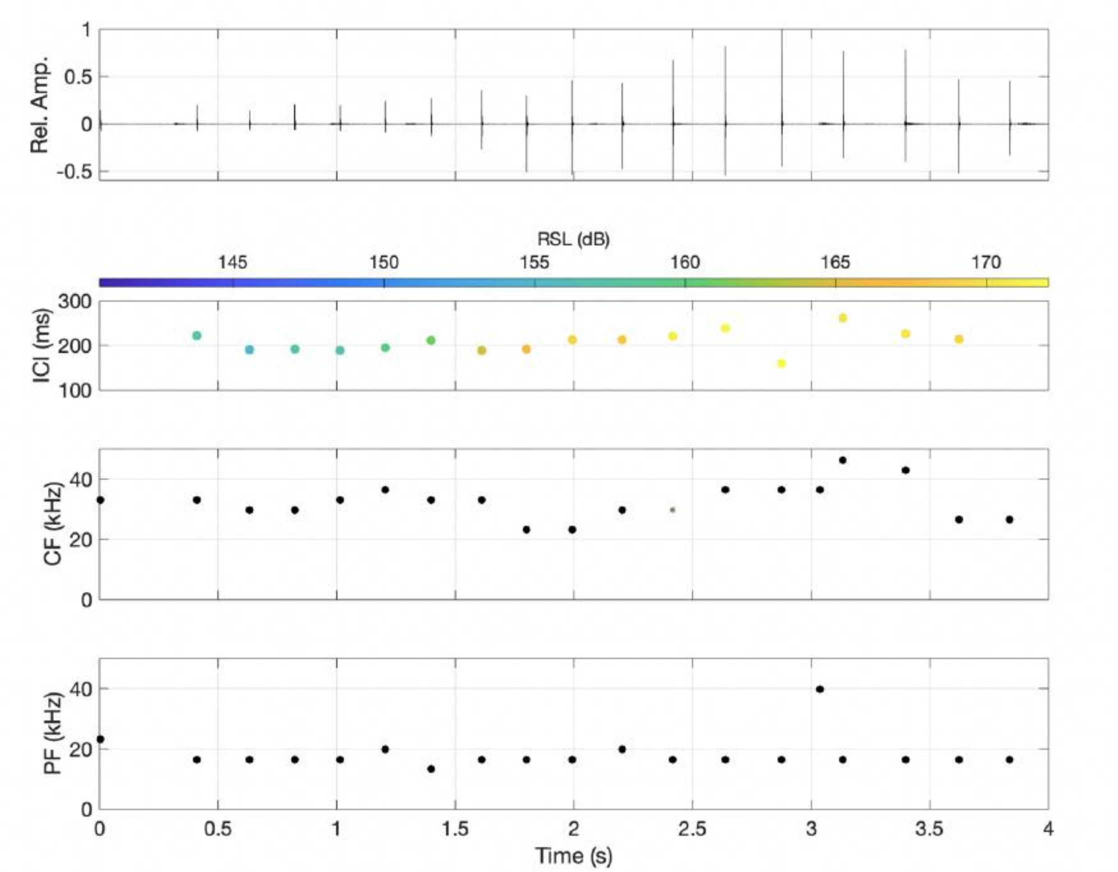

Figure 4.32: A graphical representation of a NRKW slow-click train and its characteristics. Time and location of recording: 13 August 2019, 18:24:36 UTC, Johnstone Strait.

## 4.5 NRKW and SRKW Click Comparison

The question of whether there are differences in echolocation click characteristics between SRKWs and NRKWs can be addressed here since this thesis provides the first

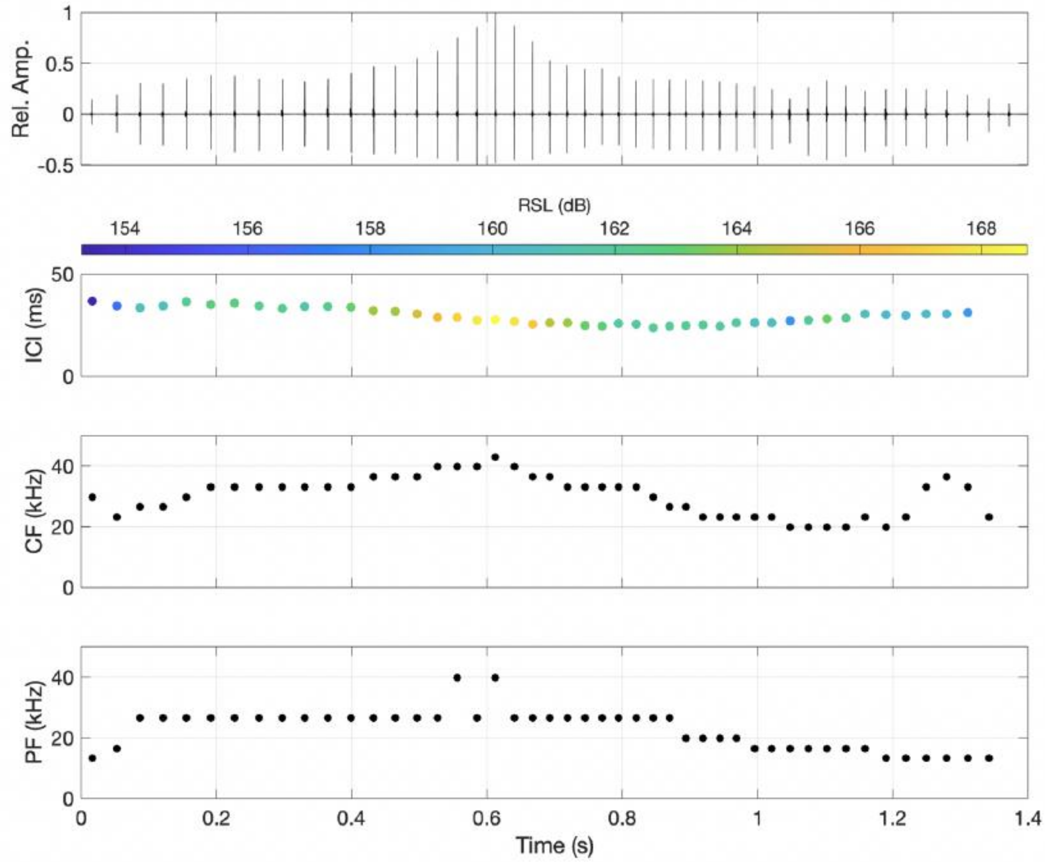

Figure 4.33: A graphical representation of a NRKW fast-click train and its characteristics. Time and location of recording: 18 August 2019, 13:19:10 UTC, Johnstone Strait.

documented recordings of SRKW click characteristics. Comparing Tables 4.2 and 4.4, which present the acoustic characteristics of all clicks for SRKWs and NRKWs, respectively, shows that there are no significant differences between ecotype slow- and fast-clicks. Similarly, the characteristics of the largest clicks in each click train, presented for SRKWs and NRKWs in Tables 4.3 and 4.5, respectively, show no significant differences given standard deviations. This suggests that there is virtually no difference in how RKW ecotypes use slow- and fast-clicks. Unfortunately, buzz-clicks could not be compared as none were recorded for SRKWs.

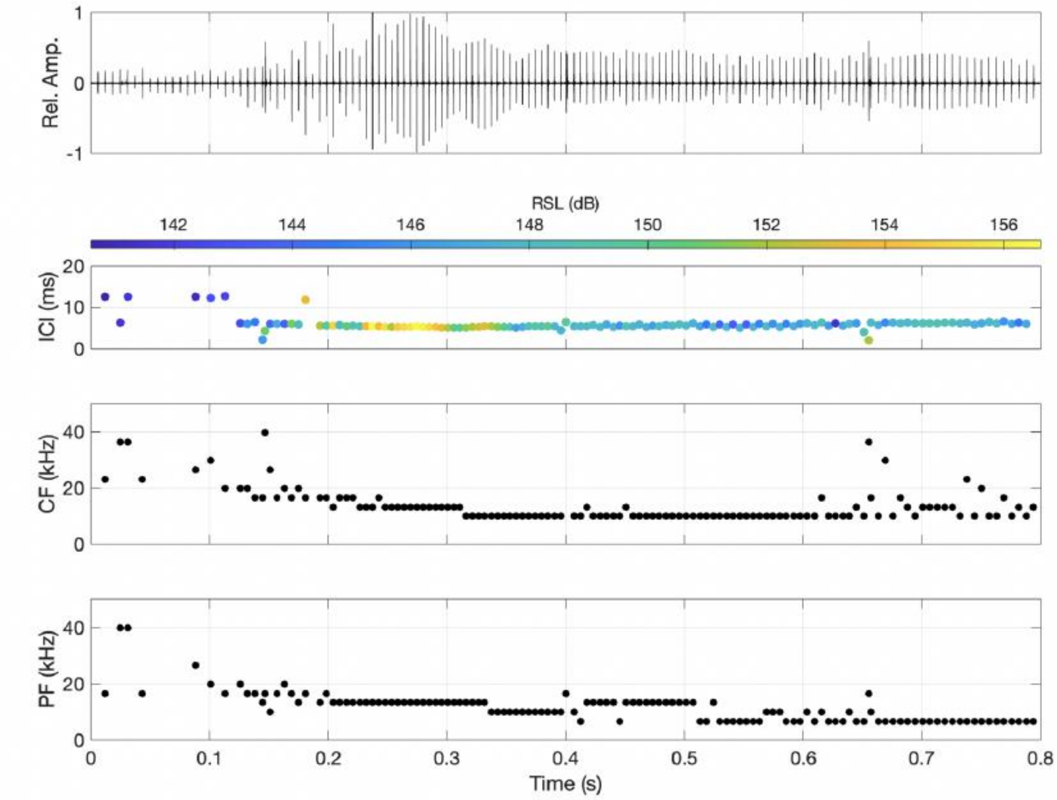

Figure 4.34: A graphical representation of a NRKW buzz-click train and its characteristics. The higher frequency data points are thought to be Pacific white-sided dolphins. Time and location of recording: 18 August 2019, 13:18:50 UTC, Johnstone Strait.

## 4.6 Comparison to Other Studies

Due to the inherent difficulty in measuring echolocation clicks, described in Section 3.1.5, only one study has been found that publishes results on RKW echolocation clicks, and only for NRKWs. Furthermore, no study could be found by this researcher that has attempted to differentiate acoustic characteristics between SRKW and NRKW clicks, or click type. As such, the click characteristics reported here can only be compared to other published values in a generalized sense. The values reported in this study for peak frequency and RMS bandwidth are in agreement with those published in [9], for NRKWs. That study reported slightly shorter click durations than this work; however, it is possible that signal reflections did not influence those results to the same extent due to array geometry and proximity to the ocean surface. The ASL range in this study for NRKWs (179-221 dB re 1 $\mu$Pa at 1 m) was somewhat lower than that published in [9], 194-224 dB re 1 $\mu$Pa; however, that study had a much larger sample size ($n = 1185$). The highest value in this study (221 dB re 1 $\mu$Pa) is only 3 dB lower than that in [9]. The majority (75%) of ASLs reported in [9] fell within 195-210 dB re 1 $\mu$Pa. The biggest discrepancy between the two studies is in centroid frequency values. The centroid frequencies determined here were nearly 20 kHz lower than in [9]. They reported that 76% of recorded signals had a centroid frequency greater than 50 kHz, a significantly higher number than in this study — approximately 5%.

The odontocete study (on white-beaked dolphins) carried out in [10] showed that both slow- and fast-click trains (referred to in that study as regular clicks) tended to have shorter durations and higher frequencies than buzz-click trains. There is some evidence in this study to suggest RKW click trains follow a similar pattern, based on the single NRKW buzz-click train recorded.

# Chapter 5

# Summary

Odontocetes produce short-duration, impulsive broadband echolocation clicks for the purposes of foraging and navigation. Acoustic characteristics of these clicks are well known for several species; however, there exists a data gap for resident killer whales, an endangered species residing in coastal waters of the Pacific Northwest. Underwater anthropogenic noise has been identified as a threat to RKW foraging abilities in the form of auditory masking. It is difficult to quantify the extent of the masking through noise modelling, however, due to the data gap.

A research team from the University of Victoria attempted to fill this gap by designing and constructing a 2 m × 2 m rectangular array of approximately 24 hydrophones, and deploying the array in RKW critical habitats to record echolocation clicks. Data were gathered over two field seasons on two subspecies — northern and southern RKWs. Data analysis was carried out and click acoustic characteristics were extracted. These are presented for both SRKWs and NRKWs, and further separated into click type based on inter-click interval, which studies suggest is an indicator of the phase of foraging behaviour. RKWs may alter echolocation ICI depending on which phase of foraging they are in: slow-clicks are often used during prey search, fast-clicks during prey pursuit, and buzz-clicks immediately prior to prey capture [11]. The temporal characteristics used to characterize the clicks are peak-to-peak source level, inter-click interval, and duration. The spectral characteristics are peak frequency, centroid frequency, root-mean-square bandwidth, and the peak frequency and relative power of a high-frequency secondary peak which is often present in the spectrum.

Calculation of source levels requires knowledge of the source-to-receiver distance (range) such that propagation loss effects (spherical spreading and absorption) can be quantified. This study considered two approaches to source localization — linearized inversion and a 3D grid search. The grid search was deemed superior due to the nonlinear nature of the localization problem, which led to erroneous uncertainty and sometimes to divergence for the linearized approach. Additionally, due to the high directionality of RKW echolocation clicks, data-quality criteria were implemented to attempt to identify which clicks were roughly on-axis — an important distinction when reporting source levels. In total, 708 clicks from 19 click trains, and 1277 clicks from 16 click trains were used to extract acoustic characteristics, for SRKWs and NRKWs, respectively.

Results in this study suggest SRKWs and NRKWs utilize the acoustic spectrum for echolocation clicks similarly. No data suggest significant differences, spectrally or temporally, between subspecies' clicks.

This study reports the acoustic characteristics of each click type in order to assess the potential changes made by RKWs. Temporal and spectral characteristics do not appear to change significantly between RKW fast- and slow-clicks. The one buzz-click train, however, shows significant differences from the other types. Buzz-click mean centroid and peak frequencies are approximately 10 kHz lower, and mean click duration approximately 20% longer, compared to slow- and fast-click. The results from [10], which conducted a similar click-type comparison on white-beaked dolphins, reports similar differences between click types.

The values obtained for NRKW apparent source levels were found to vary between 179-221 dB re 1 $\mu$Pa at 1 m. The range overlaps but is somewhat lower than that reported in [9] of 194-224 dB re 1 $\mu$Pa at 1 m. The values for SRKW ASLs were similar to NRKWs in this study, varying between 192-220 dB re 1 $\mu$Pa at 1 m. This is the first study to report source levels for SRKWs. Although the data are somewhat sparse, the results here support a relationship between click source levels and the range to the echolocation target, suggesting RKWs may seek to achieve a roughly constant level of echo return and adjust source levels depending on target range, according to two-way spherical spreading loss. While most characteristics reported here are in approximate agreement with [9], it is worth noting that the mean centroid frequency differs significantly, with a mean value here for NRKWs of 26 kHz while [9] reports a mean of 50 kHz.

RKW populations are thought to have thrived in centuries past. It is only in recent decades that the species is facing the threat of extinction due to anthropogenic activities. It is the responsibility of human populations to act as environmental stewards, which includes encouraging RKW population growth. Protection of the RKW critical habitat is paramount in ensuring the survival of these iconic animals in the Pacific-Northwest. Recent studies have shown there are drastic anthropogenic noise increases occurring within the same habitat the Canadian government has vowed to protect [20]. The results presented in this study will be used in future work to quantify the effects of this anthropogenic noise on RKW foraging abilities.

# Bibliography

[1] Killer Whale Recovery Team. National recovery strategy for northern and southern resident killer whales (Orcinus orca). March, 2005.

[2] S. Veirs, V. Veirs, and J.D. Wood. Ship noise extends to frequencies used for echolocation by endangered killer whales. *PeerJ*, 2016(2):1–35, 2016.

[3] F.I.P. Samarra, V.B. Deecke, K. Vinding, M.H. Rasmussen, R.J. Swift, and P.J. O. Miller. Killer whales (Orcinus orca) produce ultrasonic whistles. *The Journal of the Acoustical Society of America*, 128(5):EL205–EL210, 2010.

[4] M.M. Holt, D.P. Noren, V. Veirs, C.K. Emmons, and S. Veirs. Speaking up: Killer whales (Orcinus orca) increase their call amplitude in response to vessel noise. *The Journal of the Acoustical Society of America*, 125(1):EL27–EL32, 2009.

[5] M.A. Bigg and A.A. Wolman. Live-Capture Killer Whale (Orcinus orca) Fishery, British Columbia and Washington, 1962–73. *Journal of the Fisheries Research Board of Canada*, 32(7):1213–1221, 1975.

[6] Marine Mammal Commission - Southern Resident Killer Whale. https://www.mmc.gov/priority-topics/species-of-concern/southern-resident-killer-whale/. Date accessed: 2021-06-29, 2021.

[7] O.A. Filatova, F.I.P. Samarra, L.G. Barrett-Lennard, P.J. O. Miller, J.K.B. Ford, H. Yurk, C.O. Matkin, and E. Hoyt. Physical constraints of cultural evolution of dialects in killer whales. *The Journal of the Acoustical Society of America*, 140(5):3755–3764, 2016.

[8] R. Williams, A.J. Wright, E. Ashe, L.K. Blight, R. Bruintjes, R. Canessa, C.W. Clark, S. Cullis-Suzuki, D.T. Dakin, C. Erbe, P.S. Hammond, N.D. Merchant,

P.D. O'Hara, J. Purser, A.N. Radford, S.D. Simpson, L. Thomas, and M.A. Wale. Impacts of anthropogenic noise on marine life: Publication patterns, new discoveries, and future directions in research and management. *Ocean and Coastal Management*, 115:17–24, 2015.

[9] W.W. L. Au, J.K.B. Ford, J. K. Horne, and K. A.N. Allman. Echolocation signals of free-ranging killer whales (Orcinus orca) and modeling of foraging for chinook salmon (Oncorhynchus tshawytscha). *The Journal of the Acoustical Society of America*, 115(2):901–909, 2004.

[10] L. Yang, M. Sharpe, A.J. Temple, and P. Berggren. Characterization and comparison of echolocation clicks of white-beaked dolphins (Lagenorhynchus albirostris) off the Northumberland coast , UK Characterization and comparison of echolocation clicks of white-beaked dolphins (Lagenorhynchus albirostris). (March), 2021.

[11] M.M. Holt, M.B. Hanson, C.K. Emmons, D.K. Haas, D. A. Giles, and J.T. Hogan. Sounds associated with foraging and prey capture in individual fish-eating killer whales, Orcinus orca. *The Journal of the Acoustical Society of America*, 146(5):3475–3486, 2019.

[12] P. T. Madsen and M. Wahlberg. Recording and quantification of ultrasonic echolocation clicks from free-ranging toothed whales. *Deep-Sea Research Part I: Oceanographic Research Papers*, 54(8):1421–1444, 2007.

[13] X. Lurton. *An Introduction to Underwater Acoustics.* Springer in association with Praxis Publishing, Berlin, second edition, 2002.

[14] S.E. Dosso, G.H. Brooke, S.J. Kilistoff, B.J. Sotirin, V.K. McDonald, M.R. Fallat, and N.E. Collison. High-precision array element localization for vertical line arrays in the arctic ocean. *IEEE Journal of Oceanic Engineering*, 23(4):365–378, 1998.

[15] M.M. Holt, D. P. Noren, and C.K. Emmons. An investigation of sound use and behavior in a killer whale (Orcinus orca) population to inform passive acoustic monitoring studies. *Marine Mammal Science*, 29(2):193–202, 2013.

[16] J.K.B. Ford. Acoustic behaviour of resident killer whales (Orcinus orca) off Vancouver Island, British. *Canadian Mining Journal*, 134(1):30–31, 1989.

[17] J.C. Koblitz, M. Wahlberg, P. Stilz, P.T. Madsen, K. Beedholm, and H. Schnitzler. Asymmetry and dynamics of a narrow sonar beam in an echolocating harbor porpoise. *The Journal of the Acoustical Society of America*, 131(3):2315–2324, 2012.

[18] J.C. Koblitz, P. Stilz, M.H. Rasmussen, and K.L. Laidre. Highly directional sonar beam of narwhals (Monodon monoceros) measured with a vertical 16 hydrophone array. *PLoS ONE*, 11(11):1–17, 2016.

[19] A. Villadsgaard, M. Wahlberg, and J. Tougaard. Echolocation signals of wild harbour porpoises, Phocoena phocoena. *Journal of Experimental Biology*, 210(1):56–64, 2007.

[20] C. Erbe, R. Williams, D. Sandilands, and E. Ashe. Identifying modeled ship noise hotspots for marine mammals of Canada's Pacific region. *PLoS ONE*, 9(3):1–10, 2014.